Universidad Jaume I

Escuela Superior de Tecnología y Ciencias Experimentales

Departamento de Física

UNIVERSITAT
JAUME·I

Programmable optics for ultrashort pulse management: devices and applications.

PhD Thesis by

Jorge Pérez Vizcaíno

Supervisors:

Dr. Gladys Mínguez Vega

Dr. Omel Mendoza Yero

Castellón, Junio 2015

UNIVERSITAT
JAUME·I

Dña. Gladys Mínguez Vega, Profesora Titular de Óptica de la Universidad Jaume I de Castellón, y D. Omel Mendoza Yero, Doctor en Óptica de la Universidad Jaume I,

CERTIFICAN:

> Que la presente memoria “PROGRAMMABLE OPTICS FOR ULTRASHORT BEAM MANAGEMENT: DEVICES AND APPLICATIONS”, resume el trabajo realizado, bajo su dirección, por D. Jorge Pérez Vizcaíno y constituye su Tesis para optar al Grado de Doctor.

Para que así conste, en cumplimiento de la legislación vigente, firman el presente certificado en Castellón, a dieciocho de junio de dos mil quince.

Fdo.: Gladys Mínguez Vega

Fdo.: Omel Mendoza Yero

A mis padres y a mi hermano.

“The next Monday, when the fathers were all back at work, we kids were playing in a field. One kid says to me, “See that bird? What kind of bird is that?” I said, “I haven’t the slightest idea what kind of a bird it is.” He says, “It’s a brown-throated thrush. Your father doesn’t teach you anything!” But it was the opposite. He had already taught me: “See that bird?” he says. “It’s a Spencer’s warbler.” (I knew he didn’t know the real name.) “Well, in Italian, it’s a Chutto Lapittida. In Portuguese, it’s a Bom da Peida. In Chinese, it’s a Chung-long-tah, and in Japanese, it’s a Katano Tekeda. You can know the name of that bird in all the languages of the world, but when you’re finished, you’ll know absolutely nothing whatever about the bird. You’ll only know about humans in different places, and what they call the bird. So let’s look at the bird and see what it’s doing—that’s what counts.” (I learned very early the difference between knowing the name of something and knowing something.)”

Richard Feynman

Agradecimientos

Desocupado lector, bien está documentado que hasta el más loco hidalgo de la Mancha, por mucho o poco que tenga de ingenioso, se acompaña de cuerdos escuderos antes de emprender cualquier viaje. Esta tesis no es una excepción, y más que una colección de artículos, es una colección de personas que la han hecho posible.

En primer lugar me gustaría agradecer enormemente a mis directores de tesis todo el apoyo y tiempo que me han brindado estos años. Muchas gracias Gladys por tu dedicación, por lo que me has enseñado y lo mucho que he disfrutado a tu lado. Muchas gracias Omel por todas esas fructíferas horas de laboratorio y por ayudarme siempre que te lo he pedido. Ha sido un verdadero placer trabajar con vosotros, y más aún conoceros. Sé que dirigiréis muchas más tesis, ¡pero yo seré siempre vuestro primogénito!

Me siento también muy afortunado de haber podido compartir esta experiencia con todos los miembros del GROC. Quiero empezar agradeciendo a Jesús Lancis la confianza depositada en mí para llevar a cabo este proyecto, así como sus siempre buenos consejos. También a Merche, Lluis, Enrique y Raúl, que tanto me han ayudado con esta tesis, con la docencia, o simplemente con las buenas conversaciones acompañadas de los manjares de la cantina. Gracias a Pere, por responder siempre a mis llamadas de auxilio cuando el láser no funcionaba. Y por supuesto a Vicente, cada día más vikingo. A ti te debo tu *conspicua* compañía y demás vocablos *preconstitucionales*. Finalmente, dar las gracias a Pedro Andrés, al que siempre estaré agradecido por iniciarme en esta aventura.

Quiero reconocer aquí la paciencia que Rocío tuvo conmigo en tantos buenos meses juntos en el laboratorio, y lo mucho y bien que aprendí con ella. Todo lo no-lineal que soy se lo debo a Rocío, así como a los flaones de Jenny. Jamás sabremos quién se comió el último. Agradecer también a todos los nuevos jóvenes que han ido llegando, Alex, Ángel, Carlos, Esther, Eva, Fernando, Miguel, Omar y Salva, los buenos ratos que hemos pasado y su enorme espíritu emprendedor. Ahora ya sé un poquito más sobre series de televisión, la expropiación de tazas de equipos ajenos, la intoxicación de departamentos enteros con pollo, o cómo desalinear un interferómetro y que parezca un accidente. Gracias a todos, nos vemos en Balsicas.

De las idas y venidas propias de las estancias, quiero empezar agradeciendo a Vincent Loriot lo mucho que aprendí con él durante su estancia en Castellón. Fue una época muy fructífera para mi investigación.

De la estancia en Salamanca, agradecer profundamente a Íñigo su dedicación conmigo enseñándome tanto en el laboratorio. También a Benja, Javi, Isa y demás miembros del CLPU por su hospitalidad y paciencia. Y un recuerdo para Luca, por enseñarme los rincones más animados de la gran ciudad de Salamanca, a la que volveré seguro.

I would like to thank Willem Vos for giving me the opportunity to work at COPS. I learnt a lot from your group, and my experience in The Netherlands was wonderful. Thanks to all the members of COPS who made me feel like at home, and specially to Diana for the bad and good days at the laboratory. I also appreciate a lot the hospitality of Marijke Reehuis.

Quiero acordarme de los amigos que han estado apoyándome este tiempo. Sé que prácticamente ninguno de vosotros sabe muy bien a qué me dedico, pero siempre dais buenos momentos. A todo el círculo del Peset, con especial mención a Carlos, a Pedro y sus fieles visitas, a Raimon y César, a Manu y Guille, a mi *compi* Fran, y a Patri por enseñarme la Holanda interior. No me hace falta decir nombres para acordarme en esta tesis de cada uno de los *gafas*, todo el que realmente lo es se siente aludido. Y también a Sergio, un castellano del norte que invade a los del sur cada feria de Septiembre.

Finalmente, no voy a ahorrar palabras de agradecimiento a mi familia. Quiero dedicar esta Tesis a mis padres. Aprecio y valoro mucho todo el esfuerzo que habéis hecho por mi educación. Esta tesis es la culminación de todos esos años de dedicación que me habéis dado. Y como no, a mi hermano, al que le debo horas y horas de fútbol en el pasillo. También a mis abuelos, siempre un ejemplo de por qué el sacrificio de hoy da sus frutos mañana. A mis tíos y primos por su apoyo constante. Y gracias

a Elena, por ser tan comprensiva, por haber soportado todas mis ausencias,
y por los buenos momentos que hemos pasado y los que nos quedan.

CONTENTS

Acronyms List

AOPDF	Acousto-Optic Programmable Dispersive Filter
BBO	Beta Barium Borate
CEP	Carrier to Envelope Phase
CGH	Computer Generated Hologram
CPA	Chirped Pulse Amplification
DCM	Dispersion Compensation Module
DL	Diffractive Lens
DMD	Digital Micromirror Device
DML	Diffractive Microlens
DOE	Diffractive Optical Element
DOF	Depth Of Focus
DST	Direct Space-to-Time
FROG	Frequency-Resolved Optical Gating Measurement
FTB	Flat-Top Beam
FWHM	Full Width Half Maximum
GL	Grey Level
IFTA	Iterative Fourier Transform Algorithm
LCD	Liquid Crystal Display
LCOS	Liquid Crystal On Silicon
LUT	Look-Up Table
NA	Numerical Aperture
OCT	Optical Coherence Tomography
OPA	Optical Parametric Amplification
PAN	Parallel Aligned Nematic
PTD	Propagation Time Difference
QDST	Quasi-Direct Space-to-Time
RB	Rhodamine B
SC	Supercontinuum
SH	Second Harmonic
SHS	Shack-Hartmann Sensor
SLM	Spatial Light Modulator
STARFISH	SpatioTemporal Amplitude-and phase Reconstruction by Fourier-transform of Interference Spectra of High-complex-beams
TN	Twisted Nematic
TPA	Two-Photon Absorption
VAN	Vertical Aligned Nematic

Chapter 1. Introduction

The laser was discovered at the beginning of the sixties of the 20th century. Nowadays, it is included in most of the rankings as a discovery that revolutionized science and the world. There are already more than ten Nobel Prize winners whose work was made possible by lasers. The last Nobel Prize in Chemistry 2014, granted during the writing of this Thesis, was awarded jointly to Eric Betzig, Stefan W. Hell and William E. Moerner "for the development of super-resolved fluorescence microscopy". Old times when laser was “a solution looking for a problem” seem to be quite far away.

1.1 ULTRASHORT PULSES

Lasers have evolved very fast since its invention. Big advances have been made pursuing improvements of different laser properties: new wavelength ranges, different repetitions rates, high energies [1-3], etc. Additionally, one of the biggest efforts has been made in order to develop pulsed laser sources. During the sixties, the Q-switching technology [4] allowed for the generation of microsecond (µs) and nanosecond (ns) pulses. The mode-locking technique developed in the sixties [5], and the discovery of new materials as the case of Ti:Sapphire (Ti:Al_2O_3) [6], enabled the generation of shorter pulses. In this way, picoseconds (ps) in the seventies and femtoseconds (fs) pulses in the eighties were also available. However, the pulse energy reached by these techniques was of the order of the nanojoules (nJ), insufficient for some applications. This problem was overcome by Strickland and Mourou in the mid-eighties with the development of the chirped pulse amplification (CPA) technology [7]. CPA allows for femtosecond pulse energies up to several joules.

By ultrashort (or ultrafast) we mean femtosecond (or less) pulse duration, which means a unit of the order of 10^{-15} s [8]. Nowadays, subcycle attosecond pulses (10^{-18} s) have been achieved [9]. Hence, a simple question arises: why are we so interested in the generation of shorter pulses? In a very first approach, shorter pulses mean being able to measure shorter live events. Many essential processes and interactions on atomic and molecular scales occur at ultrashort timescales. However, ultrafast phenomena involve more than just the study of ultrashort live events. The characteristics of this kind of illumination, listed below, make it an indispensable tool to develop many applications in different fields of science and technology.

The main properties of ultrashort laser pulses are:

Short duration. The most obvious property of ultrashort pulses is their extremely short duration. Ultrashort laser pulses are far shorter and their ability to time-resolve fast processes such as molecular dynamics is far greater than anything that can be accomplished by means of state-of-the-art electronics (time resolution of a few picoseconds). This also means that pulse characterization cannot be determined directly by electronic devices. For this reason, pulses are characterized using optical methods, in which it is typically the short pulse itself that acts as the probe [10-13].

Broad spectral bandwidth. The generation of short pulses is the result of the coherent sum of several waves of different frequencies. Short pulses imply large spectral bandwidths. Continuous wave lasers (CW) are defined by its quasi-monochromatic spectrum. However, a typical pulse with 30 fs intensity at full width half maximum (FWHM) has a spectral bandwidth of around 50 nm. In this way, when dealing with short pulses, the dependent wavelength response of an optical system must be carefully considered to avoid undesirable effects.

Pulse repetition rate. Depending on the technique of pulse generation, typical pulse repetition rates can be between 1 Hz to several GHz. Control of the pulse repetition frequency of femtosecond lasers remains a challenge [14]. The repetition rate is in most cases fixed, although tunability only within a small range is also available.

High peak power with low energy average. The extremely short duration of femtosecond laser pulses implies that very high peak powers can be generated even for moderate pulse energies. Pulse energies at the microjoule and milijoule level (typically achieved in amplified laser systems) mean peak powers exceed 10MW and 10GW, respectively for pulse widths of 100 fs. When focused down to small spot sizes on the order of 30 µm^2, these pulses give on-target intensities of 1–1000 TW/cm^2. At such high intensities, it is even possible to accelerate protons [15] when focused beams interact with plasmas.

Short coherence length. As with narrow spectral bandwidth, long coherence length is one of those properties of laser light that is traditionally thought of as being beneficial. This is especially true for such applications as holography, were the depth of field of the image demands a rather long coherence length. However, ultrashort pulses exhibit short coherence length. To give a physical insight of the relation between pulse width and coherence length, a 100 fs laser pulse has a coherence length of about 30 µm. This is beneficial in applications such as optical coherence tomography (OCT), where the longitudinal resolution of OCT depends directly on the coherence length of the source [16, 17].

1.2 ULTRASHORT LASERS: APPLICATIONS AND FUTURE DEVELOPMENT

The term ultrashort technology encompasses the study of the generation, manipulation and measurement of ultrashort pulses. Big efforts are being made to promote the development of all of these areas. Advances in laser development (pulse generation) are keys for new advances in laser physics experiments. In this way, ultrashort technology offers the possibility to observe and study new phenomena that arise from the combination of short pulses at high energies and their interaction with matter. This is the reason why new types of laser infrastructures conceived to produce high peak powers and focused intensity are being built. As examples, the Spanish Pulsed Lasers Centre (CLPU) achieves petawatt pulse powers by generating pulses of 30 fs with 30 J of energy per pulse. On the other hand, the Extreme Light Infrastructure (ELI) [18], is designed to be the first exawatt-class (10^{18} W) laser. This power will be obtained by achieving a kilojoule of energy into a pulse of only 10 fs in duration.

The range of applications of ultrashort lasers is very broad. Femtochemistry [19], material processing [20], cells and tissue nanosurgery [21] are some examples. Apart from these, a selection of some applications specially active and promising are described below:

Brain activity map: neural circuits operate at emergent levels, where the interactions among hundreds or thousands of neurons generate functional states [22]. Ultrashort pulses together with spatial light modulators (SLMs) are used for structured non-linear illumination to activate dendritic spines and cortical neurons in brain slices [23, 24]. In this way, two-photon excitation of deep tissue, faster scanning strategies or scanless approaches using SLMs are aimed to reconstruct the full record of neural activity across complete neural circuits [25].

Focusing through scattering media: light scattering in inhomogeneous media induces wavefront distortions that limits the resolution and penetration depth of microscopy techniques. Wavefront shaping of the incident beam by means of a SLM allows for the correction of spatial distortions [26]. The technique has been also extended to ultrashort pulses, allowing new possibilities for optical manipulation and nonlinear imaging in scattering media [27, 28].

Filamentation for tumor suppression: gaining control over the spatial filaments distribution is an important task in applications such as filamentation-based tumor treatment [29], a novel technique which has been recently proposed for cancer therapy. In such case, an intense ultrashort infrared laser is used for filamentation generation. A careful management of both the position and the energy of the filaments is decisive to control the radiological dose and avoid damage of the adjacent healthy tissue.

High-harmonic and attosecond pulses generation. Short pulses need to acquire a broad spectrum before they can be recompressed. To go to shorter pulses than one light period, higher frequencies must be generated. This is done by high harmonic generation in a gas jet [30]. A fraction of the harmonic spectrum is selected to produce pulses down to 0.08 fs [31]. Among other benefits, the generation of pulses at the attosecond scale offers the possibility to study the electron dynamics on real time [9].

Proton laser acceleration. When a laser beam is focused onto thin foils, protons can be accelerated when intensities larger than 10^{20} W/cm^2 are reached in the focal region [15]. Proton laser acceleration can lead to cheaper sources of proton beams for medical applications [32] like cancer treatment, improving deposition accuracy of conventional photon therapies.

Hydrophobic materials. Metals and semiconductors are irradiated by femtosecond illumination, creating a surface morphology that exhibits structure on the micro- and nanoscale [33]. By varying the laser fluence, the surface morphology and the wetting properties are tuned [34]. It results in functional surfaces with special hydrophobic and self-cleaning properties with strong impact in daily life, industry and agriculture [35].

1.3 PULSED BEAM SHAPING AND MOTIVATION

Ultrashort lasers are nowadays an essential tool in many fields of scientific research. The fabrication and commercialization of pulsed laser sources is progressing very fast, resulting in more compact, reliable and economical devices. As a result, ultrashort lasers have increasingly greater demand, even by users who are not experts in laser physics. Moreover, the ultrashort laser technology is gradually penetrating in the industry sphere. All this requires control tools more and more oriented to the final user, which essentially demands robust and trustable devices, user-friendly interfaces, and versatile operation modes that fit user requirements.

In most of the cases, simply having an ultrashort pulse does not guarantee that it is suitable for real-world applications. Usually the output of the laser source needs to be manipulated. In other words, some characteristics of the beam, such as the temporal or spatial profile, must be modified in order to satisfy the user requirements for a final application. The main reason is that the interaction of ultrashort pulses with matter generally lead to nonlinear phenomena which greatly depend on the spatiotemporal structure of the input beam. Of course, beam shaping is not exclusive to ultrashort lasers. Since the invention of the CW laser, numerous techniques have been proposed to control the propagation of a laser beam in the spatial profile, ranging from open loop control [36-43] to feedback (adaptive) control [26, 44, 45]. With the development of pulsed light sources, beam shaping techniques were also extended to the time domain [46, 47].

Unfortunately, beam shaping of femtosecond pulses is far from trivial and it requires different methods or considerations with respect to those developed for monochromatic or quasi-monochromatic radiation. Replacing a CW laser by a pulsed laser without further considerations may lead to undesirable distortions. This is especially true for few fs pulses, which have a huge spectral bandwidth. When the pulse propagation through an optical system is wavelength dependent, each wavelength component of the pulse may experience a different spatial propagation. It leads not only to distorted spatial patterns, but also to a spatial dependence of the pulse duration. In this way, both the spatial and the temporal profiles are simultaneously modified, causing a strong spatiotemporal coupling of the pulse. Therefore, the spatial and temporal pulse control is an issue that has many technological challenges, but absolutely necessary for any further application. In this sense, beam delivery from the laser source to the final target is as important as the generation of the pulse itself.

This Thesis focuses in femtosecond pulse shaping, a complementary topic to femtosecond pulse generation. We aim to exploit diffractive optical elements (DOEs) to build up new devices for programmable and real time femtosecond shaping. DOEs offer many advantages over other devices based on refractive or reflective optics. Diffractive surfaces can be computed and traced to cancel or minimize the impact of wave aberrations and, in general, to sculpt user-defined pulsed beams with control over the spatial and temporal profile. But what is most important: they can be encoded in SLMs. SLMs are opto-electronic devices able to modulate the phase, amplitude and polarization of a laser beam at a micro scale. They are controlled by computer. To fabricate an arbitrary structure, a computer generated hologram (CGH) is encoded onto the SLM. This feature allows for the generation of programmable and versatile DOEs able to modulate light in almost real time. All these features make them extremely attractive for the final user.

The objective of this thesis is double.

I. The first one is the development of new all-optical devices to manipulate femtosecond pulses in a controlled fashion by means of DOEs encoded in SLMs.
II. The second one is the study of the above devices for novel applications in the field of nonlinear optics.

I. Innovative femtosecond devices

Spatial shaping of ultrashort pulsed beams with temporal control.

We have developed devices for transferring amplitude and/or phase maps onto the spatial profile of an ultrashort pulse by using reconfigurable SLMs based on liquid crystal on silicon (LCOS) technology. Both coherent and random phase realizations (by means of learning algorithms) have been proposed. In this way, arbitrary waveforms have been generated both in the transverse and on-axis dimensions. Moreover, we have used a hybrid refractive-diffractive module to compensate for the dispersive effects in the fine generation of temporally resolved femtosecond light patterns with micrometer resolution. This set of techniques constitute the basis for the laser-matter experiments carried out in the second part of this Thesis.

Active femtosecond optics.

Wavefront shaping can be dramatically influenced by aberrations, to the point of introducing distortions that invalidate pulse shaping techniques in terms of efficiency and spatiotemporal pattern generation. For example, much effort is being made to fabricate more powerful pulsed lasers to reach ultrahigh intensities when they are focused into a target. However, the presence of aberrations can eventually reduce the intensity at the focus to a marginal quantity, making aberrations the real bottleneck to get ultrahigh focusing intensities. In this way, we have developed a new method to measure and correct wavefront aberrations specifically designed for femtosecond pulsed laser beams. The method only requires a programmable SLM and a camera. It provides accurate results even when implemented with low dynamic range cameras and polychromatic beams. The aberrations are not only measured at the SLM plane, but thanks to programmable nature of the SLMs they are also cancelled out by the SLM itself. It allows us to measure and correct aberrations with the SLM placed at exactly the position where it will be used in future experiments, discarding the introduction of external wavefront sensors.

Temporal pulse shaping.

We have designed the first device for temporal shaping that consists only of a single diffractive element controlled on real-time. This quasi-direct space-to-time (QDST) pulse shaper is reduced to a simple phase mask encoded onto a SLM. In this proposal the entire size of the pulse shaper is very small, there is almost no need for optical alignment, and obviously no extra refractive focusing elements are required. The proposed pulse shaper exhibits not only real-time temporal modulation, but also high efficiency output pulses thanks to an active suppression of wavefront aberrations by means of the SLM. Moreover, the SLMs peak power damage threshold is of about 0.25 TW/cm^2, so they constitute an appropriate and low-cost tool for femtosecond pulse shaping with amplified beams. The proposed technique constitutes a user-friendly pulse shaper for non-expert’s users.

II. Femtosecond applications

Nonlinear Optics.

Extreme light technologies lead laser-matter interactions to a new and unpredictable dimension. These interactions are extremely sensitive to changes in the input beam parameters, thus being mandatory to have as much control as possible over them. In this sense, the versatility offered by SLMs for controlling the amplitude and phase of an input beam makes them a very valuable tool for triggering nonlinear effects. We have generated controlled multifilaments in the bulk of a fused silica sample, both in the transversal and on-axis positions. Individual control of the filaments is achieved by individually changing the focusing conditions and energy coupled to each filament. The use of programmable SLMs allows for the generation of multifilaments even under adverse experimental conditions where the beam is not homogeneous or it is affected by aberrations. All this allows us to gain spectral control over the generated multifilaments, as well as over their axial and transversal positions.

Multiphoton microscopy.

Multiphoton absorption processes [48] allow for a selective excitation of fluorescence signals, providing a convenient way for high resolution microscopy. The laser focus is traditionally scanned across the samples, which makes this technique to suffer from time limitations on signal acquisition. Reducing the scanning time and extending the depth of the imaged tissue are regarded as priority objectives to improve multiphoton microscopy. In this sense, scanless approaches using SLMs to ‘‘bathe’’ the sample under femtosecond illumination are promising alternatives. The use of very short pulses can benefit nonlinear microscopy as, among others advantages, the excitation efficiency and the penetration depth both increase with decreasing pulse duration [49].

We have demonstrated scanless two-photon microscopy by using a SLM to shape the incoming laser beam into any user-defined light pattern.

This proposal highly mitigate the severe temporal limitations inherent to sequential scanning of the sample [23]. However, the induced spatiotemporal distortions spread both in space and time the irradiance patterns, thus limiting not only the spatial resolution but also the signal-to-noise ratio in two-photon microscopy. The use of a hybrid refractive-diffractive module significantly reduce spatiotemporal distortions, thus converting scanless two-photon microscopy for broadband illumination in a valid imaging tool.

1.4 THESIS OUTLINE

This thesis is organized as follows.

In **chapter 2,** we introduce the basic concepts required for the description of ultrashort laser pulses, as well as the main mathematical tools to deal with these light sources. We also discuss the propagation of the pulses through different media, both linear and nonlinear media. In **chapter 3**, we describe the use of SLMs for optical beam control. Some considerations about focusing with SLMs are discussed. Then, we exploit the SLM-CCD configuration where just a CCD camera and a SLM are used for two different purposes: characterization and suppression of the aberrations carried out by the beam and determination of the M^2 beam propagation factor of a laser beam. In **chapter 4**, we introduce state-of-the-art for temporal pulse shaping. Then, we propose a compact and reprogrammable method for QDST pulse shaping. Our pulse shaper consist on a single phase mask encoded onto a SLM.

In **chapter 5**, we introduce an all diffractive dispersion compensation module (DCM) to minimize spatiotemporal distortion effects over ultrashort pulses. The DCM, together with CGHs encoded onto the SLM, are used for scanless two photon microscopy. The use of the DCM enhances fluorescence signal and resolution. Finally, we experimentally analyse the spatiotemporal dynamics of a beam after passing trought a flat-top converter device. The SpatioTemporal Amplitude-and phase Reconstruction by Fourier-transform of Interference Spectra of High-complex-beams (STARFISH) technique for pulse characterization is demonstrated to be valuable for these cases. In **chapter 6**, we propose the application of DOEs encoded onto SLMs for triggering nonlinear effects in three different experiments. First, dynamical spatial shaping of a 30 fs laser beam by encoding Dammann lenses on a SLM is shown for the generation of stable and stationary filaments in a fused silica sample. Second, controlled multifilamentation patterns and tunable spectra are achieved for an input inhomogeneous irradiance distribution. In a third set of experiments, we show that local control over the optical phase enables us to gain fine control over filament interference effects.

1.5 PUBLICATIONS

The following publications part of this thesis. They will be cited using roman numerals. The published works are included at the end of this thesis.

Articles

[I] Pérez-Vizcaíno, J., Mendoza-Yero, O., Martínez-Cuenca, R., Martínez-León, L., Tajahuerce, E., & Lancis, J. (2012).
Free-motion beam propagation factor measurement by means of a liquid crystal spatial light modulator.
Journal of Display Technology, 8(9), 539-545.

[II] Mendoza-Yero, O., Loriot, V., Pérez-Vizcaíno, J., Mínguez-Vega, G., Lancis, J., De Nalda, R., & Bañares, L. (2012).
Programmable quasi-direct space-to-time pulse shaper with active wavefront correction.
Optics Letters, 37(24), 5067-5069.

[III] Pérez-Vizcaíno, J., Mendoza-Yero, O., Mínguez-Vega, G., Martínez-Cuenca, R., Andrés, P., & Lancis, J. (2013).
Dispersion management in two-photon microscopy by using diffractive optical elements.
Optics Letters, 38(4), 440-442.

[IV] Perez-Vizcaíno, J., Mendoza-Yero, O., Borrego-Varillas, R., Mínguez-Vega, G., Vázquez de Aldana, J. R., & Láncis, J. (2013).
On-axis non-linear effects with programmable Dammann lenses under femtosecond illumination.
Optics Letters, 38(10), 1621-1623.

[V] Borrego-Varillas, R., Perez-Vizcaino, J., Mendoza-Yero, O., Minguez-Vega, G., Vazquez de Aldana, J., & Lancis, J. (2014).
Controlled multi-beam supercontinuum generation with a spatial light modulator.

Photonics Technology Letters, IEEE, 26(16), 1661-1664.

[VI] Loriot, V., Mendoza-Yero, O., Pérez-Vizcaíno, J., Mínguez-Vega, G., de Nalda, R., Bañares, L., & Lancis, J. (2014).
Fresnel phase retrieval method using an annular lens array on an SLM.
Applied Physics B, 117(1), 67-73.

[VII] Borrego-Varillas, R., Perez-Vizcaino, J., Mendoza-Yero, O., Vazquez de Aldana, J., Minguez-Vega, G., & Lancis, J. (2015).
Dynamic Control of Interference Effects between Optical Filaments through Programmable Optical Phase Modulation.
Submitted for publication.

[VIII] Borrego-Varillas, R., Perez-Vizcaino, J., Gallardo-Gonzalez I., Alonso, B., Minguez-Vega, G., Forbes, A., & J. Sola, I. (2015).
Flat-top beam shaping of femtosecond beams.
In preparation.

Book chapters

[IX] Mendoza-Yero, O., Pérez-Vizcaíno, J., Martínez-León, L., Mínguez-Vega, G., Climent, V., Lancis, J., & Andrés, P. (2014).
Dispersion Compensation in Holograms Reconstructed by Femtosecond Light Pulses
Multi-Dimensional Imaging. 2014, John Wiley & Sons, Ltd. p. 101-125.

Chapter 2. Propagation of ultrashort pulses

Femtosecond light pulses are electromagnetic wave packets fully described by its time and space dependent electric field [8]. The electric field **E** is a vector magnitude with amplitude and phase that depends on the three spatial coordinates (x,y,z) and the time (t). Therefore, the electric field can be written as $\boldsymbol{E}(x, y, z, t)$. In this thesis the vector nature of **E** is not taken into account, so from now on we will consider the electric field as a scalar magnitude, neglecting its polarization dependence, i.e., $\boldsymbol{E}(x, y, z, t) = E(x, y, z, t)$.

The electric field E is an electromagnetic wave and thus must satisfy Maxwell equations. We can write, in Cartesian coordinates [8]:

$$\left(\frac{\partial^2}{\partial x^2} + \frac{\partial^2}{\partial y^2} + \frac{\partial^2}{\partial z^2} - \frac{1}{c^2}\frac{\partial^2}{\partial t^2}\right) E(x, y, z, t) = \mu_0 \frac{\partial^2}{\partial t^2} P(x, y, z, t), \qquad (2.1)$$

where μ_0 is the magnetic permeability of free space and c the speed of light. The polarization of the media P, which is here also presented as a scalar magnitude, describes the response of the medium to the field. The term P can be expanded depending on the contribution of the electric field to the polarization of the media [50]:

$$P(t) = \mathcal{E}_0 \big[\underbrace{\chi^{(1)} E(t)}_{P^L} + \underbrace{\chi^{(2)} E^2(t) + \chi^{(3)} E^3(t) + \cdots}_{P^{NL}} \big]. \qquad (2.2)$$

For simplicity the spatial dependence of the fields P and E is neglected in Eq. (2.2), where $\mathcal{E}_0$ is the permittivity of free space and $\chi^{(1)}$ is the linear optical susceptibility. The quantities $\chi^{(2)}$ and $\chi^{(3)}$ are the second- and third-orders nonlinear optical susceptibilities, respectively. These orders (and higher ones) contribute to the nonlinear polarization of the media P^{NL}. When P^{NL} is neglected we are in the regime of linear (classical) optics governed by the linear polarization P^{L}. This term is responsible for effects such as diffraction, dispersion, refraction and linear gains and losses [8]. The term P^{NL} is responsible for nonlinear phenomena where, unlike linear processes, the frequency of light can change when propagating through the media or the material's properties are dependent on the intensity of the input field. Harmonic generation, two-photon absorption (TPA), or supercontinuum (SC) generation are some examples of nonlinear processes [50].

2.1 TEMPORAL DOMAIN

In this section we only consider the temporal dependence of the electric field, neglecting the spatial contribution. In this sense, we can write $E(x, y, z, t) = E(t)$.

A complex representation is more convenient for the study of pulse propagation problems using Fourier analysis. The real-valued electric field $E(t)$ can be represented as $E(t) = 2Re\{E^{+}(t)\}$. The complex field $E^{+}(t)$ is denoted as [8, 51]:

$$E^{+}(t) = \frac{1}{2}A(t) * exp\{i(w_0 t + \Phi(t) + \Phi_0)\}, \tag{2.3}$$

where $A(t)$ is the real field envelope and w_0 the carrier frequency of the pulse. Eq. (2.3) is valid under the assumption of slowly varying envelope approximation (SVEA). The most common function to represent the real field envelope is the Gaussian function. The phase terms $\Omega(t) = w_0 t + \Phi(t) + \Phi_0$ inside the exponential correspond to the oscillatory phase $w_0 t$, the temporal phase $\Phi(t)$ and the carrier to envelope phase (CEP) Φ_0. The CEP can be neglected for pulses longer than 100 fs. The instantaneous light frequency, defined as the time derivative of the instantaneous phase of the pulse, is then:

$$w(t) = \frac{d\Omega(t)}{dt} = w_0 + \frac{d\Phi(t)}{dt}. \qquad (2.4)$$

The importance of the temporal phase $\Phi(t)$ is stated in the above expression: the frequency of the temporal oscillation varies within the pulse. As an example to understand the implications of this phenomenon, three different Gaussian pulses with $A(t)$ temporal width $\Delta\mathrm{t} = 5$ fs at FWHM are represented in Fig 2.1. Each pulse has a different temporal phase $\Phi(t) = at^2$. The parameter a is zero for Fig. 2.1a, while $a = +0.16/fs^2$ and $a = -0.16/fs^2$ for Fig. 2.1b and 2.1c, respectively. The effect of the temporal phase is translated into a linear increase of the frequency in time when a is positive, and a decrease when a is negative. The term $\Phi(t)$ is usually called (temporal) chirp and cannot be directly modified by electronic devices. Therefore, accessing to changes in the frequency domain is a usual way to modify the temporal profile of a pulse. Fourier transform pulse shapers [52] or the Acousto-optic programmable dispersive filter (AOPDF) [53, 54] are based on this idea.

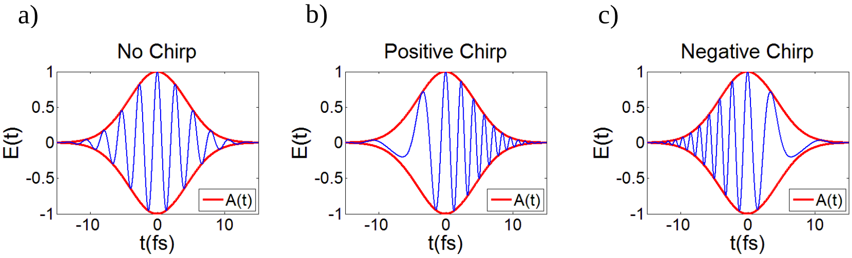

Figure 2.1 Electric field E(t) and temporal amplitude function A(t) for a) non-chirped pulse, b) chirped pulse with $a = +0.16/fs^2$ *and c) chirped pulse with* $a = -0.16/fs^2$. *The pulse amplitude A(t) in all cases is Δt=5 at FWHM.*

The temporal and frequency domain are related via the Fourier transform. In this way, we can state the relationship between the spectral field $E_f(w)$ and $E(t)$ as [51]:

$$E_f(w) = \mathfrak{F}\{E(t)\} = \int_{-\infty}^{\infty} E(t)e^{-i\omega t}\,dt \tag{2.5}$$

$$E(t) = \mathfrak{F}^{-1}\{E_f(w)\} = \frac{1}{2\pi}\int_{-\infty}^{\infty} E_f(w)e^{i\omega t}\,dw\,, \tag{2.6}$$

From Eq. (2.5) it is clear that $E_f(w)$ is a complex spectral field with negatives frequencies. However, as $E(t)$ is real-valued, $E_f(w)$ is Hermitian. It means that knowledge of the positives frequencies is sufficient for the full characterization of the field and, in practice, only positive frequencies (E_f^+) are considered. Thus, we can rewrite $E_f(w) \equiv E_f^+ = A_f(w)e^{-i\varphi(w)}$, where $A_f(w)$ denotes the spectral amplitude and $\varphi(w)$ is the spectral phase. The power spectral density $S(w)$, defined as $S(w) = [A_f(w)]^2$, is what we call spectrum and it is measured by a spectrometer. The pulse is completely characterized if the amplitude and phase is known for the spectral or time domain. From the mathematical properties of Fourier transform, it arises that short pulses in time means broadband spectrum in frequency. If the spectral amplitude and phase is known, the pulse in the time domain is obtained by applying the inverse Fourier transform. For well-behaved pulses it is often helpful to expand the spectral phase $\Phi(w)$ into a Taylor series [51]:

$$\varphi(w) = \sum_{j=0}^{\infty} \frac{1}{j!}\frac{\partial^j \varphi(w)}{\partial w^j}\bigg|_{w_0} (w - w_0)^j. \tag{2.7}$$

The zeroth order spectral phase coefficient is related to the absolute phase Φ_0 of the time domain. By the Fourier transform shift properties, the linear term introduces a shift in the temporal domain, but with no influence over the carrier frequency. The coefficients for the second and third orders are known as GDD and TOD, acronyms of “group delay dispersion” and “third order dispersion”. The introduction of GDD, TOD or higher orders distorts the temporal profile of the pulse and consequently we call it a "chirped pulse". For not chirped pulses the temporal duration of the pulses is minimum.

2.2 LINEAR BEAM PROPAGATION

So far we have only considered the temporal profile $E(t)$ of the pulses. In this section we will discuss how to calculate the spatial dependence of the electric field $E(x, y, z)$ in linear media. Many practical situations allow us to discuss the change of beam profile $E(x, y, z)$ and pulse envelope $E(t)$ as if they occur independently from each other. This is the case of uniform waves, where the transverse beam profile does not change from one plane to another. For long pulses the change of the pulse characteristics, such as duration, chirp or bandwidth can be separated from the change of beam profile. The term "long pulses" may be ambiguous. By long pulses we mean pulses that have a narrow spectrum, and in practice the effects of the spatial propagation of the pulse do not affect its temporal profile. Mathematically it implies that the electric field can be decomposed as $E(x, y, z, t) = E(t)E(x, y, z)$. For very short pulse durations, the significant bandwidth of the pulses results in a coupling of the spatiotemporal effects. In general, this may cause degradation of the beam spatial profile and stretching of the pulse duration as it is observed when high spatial frequencies are involved [55, 56]. How to take into account the spatiotemporal coupling of ultrashort pulses is briefly explained in section 2.2.1.

From Eq. (2.1) and (2.2), we can derive the wave equation of the electric field propagating in a linear medium. Again, we will use a complex representation of the electric field and the scalar diffraction theory, i.e., we will not consider polarization. However, Eq. (2.1) has a complicated structure and in general can only be solved by numerical methods [8]. Instead, we will use an integral approach: the Huygens' principle, expressed in the Fresnel approximation. In short, the Huygens' principle establishes that for an input field distribution over some closed surface S_0, we must regard each point on that surface as a source of uniform spherical waves.

The total field at any point inside or beyond the surface S_0 can be calculated by summing the spherical waves coming from each individual source point on the surface S_0 (Huygens' integral) [57].

The Fresnel approximation to the Huygens' integral consists in the approach of the "spherical waves" coming from the input field distribution, to a "paraxial-spherical wave" formalism. In physical terms, this paraxial approximation assumes that the source point x_1, y_1, z_1 is located not too far off the propagation z axis; and then it supposes that we only wish to calculate the resulting field distribution in a point of the space x_2, y_2, z_2 that sustains a small angle with respect to the source point. That is, x_2, y_2 are not far from the propagation axis (paraxial approximation). This allows us to write the Huygens' integral in the Fresnel approximation as [57]:

$$E(x_2, y_2, z_2) = \frac{i}{\lambda(z_2 - z_1)} \exp\left(-ik(z_2 - z_1)\right) * \iint_{-\infty}^{\infty} E(x_1, y_1, z_1) \exp\left[-ik \frac{(x_2 - x_1)^2 + (y_2 - y_1)^2}{2(z_2 - z_1)}\right] dx_1 dy_2, \tag{2.8}$$

where $k = \frac{2\pi}{\lambda}$.

The Huygens-Fresnel integral for wave propagation through a cascade of conventional optical elements (refractive and reflective surfaces, lenses, diffractive elements and mirrors) can be performed in one step by expressing the integral through the ABCD matrix formalism [58]. Therefore, paraxial propagation can be described entirely in terms of complex ABCD matrices.

In short, the ABCD matrix approach states that the paraxial ray vectors $\boldsymbol{r_1}$ and $\boldsymbol{r_2}$ travelling from an input plane to an output plane, respectively, are related by a linear transformation given by [57, 58]:

$$\boldsymbol{r_2} = \begin{pmatrix} A & B \\ C & D \end{pmatrix} \boldsymbol{r_1} = M \boldsymbol{r_1}. \tag{2.9}$$

The matrix M is called the ABCD matrix and varies depending on the optical elements that are between the input and output planes. For the typical cases of free space propagation over a distance d through a medium of refraction index n, or propagation through a lens of focal length f, the ABCD matrix is explicitly written as:

$$\begin{pmatrix} A & B \\ C & D \end{pmatrix} = Free\ space: \begin{pmatrix} 1 & d/n \\ 0 & 1 \end{pmatrix} Lens: \begin{pmatrix} 1 & 0 \\ -1/f & 1 \end{pmatrix}.$$

In the case of several optical elements placed in cascade (M_1, M_2, M_3,…), the resulting matrix is calculated by multiplying each individual matrix in inverse order of actuation appearance: $M = \ldots M_3 M_2 M_1$.

Expressing the Huygens-Fresnel integral for beam propagation in terms of the ABCD matrix formalism has several advantages, as the fast computing speed and the simplicity of the procedure. Moreover, as stated above, it is valid for a broad range of cases, at least, as a first order (paraxial) approximation. For an input complex field $E(x_1, y_1)$, the output field $E(x_2, y_2)$ after the ABCD system (see Fig. 2.2) is then given by [58]:

$$E(x_2, y_2) = i\frac{\exp(-ikL)}{\lambda B} \iint_{-\infty}^{\infty} E(x_1, y_1) exp\left[\frac{-ik}{2B}(A({x_1}^2 + {y_1}^2) - 2(x_1x_2 + y_1x_2) + D({x_2}^2 + {y_2}^2)\right] dx_1 dy_1. \tag{2.10}$$

Each individual element of the system is defined by a physical thickness L_i and refractive index n_i, so that the on-axis optical path length L is equal to

$$L = \sum_i n_i L_i.$$

For the case where the system has rotational symmetry we can rewrite Eq. (2.10) in terms of the radial coordinate r as [58]

$$E(r_2) = i\frac{\mathrm{k}}{B}\exp\left[-ik\left(L + \frac{D}{2B}\right){r_2}^2\right] \int_0^{\infty} r_1 E(r_1) J_0\left(\frac{k}{B} r_1 r_2\right) \exp\left[\frac{-ikA}{2B}{r_1}^2\right] dr_1, \tag{2.11}$$

where J_0 is the zero-order Bessel function.

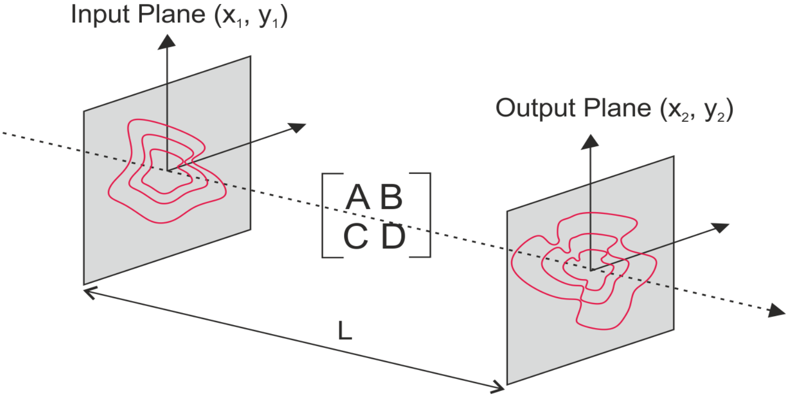

Figure 2.2 Beam propagation example for an input beam $E(x_1, y_1)$. The resulting field $E(x_2, y_2)$ is calculated at an output plane after propagating a distance L throught the ABCD optical system.

2.2.1 Spatiotemporal pulse propagation

In the case of very short pulses, there is a coupling between the spatial and temporal effects. Short pulses have a broad bandwidth and beam propagation is wavelength dependent (see Eq. (2.10)) even for propagation in a non-dispersive medium. It means that temporal and spatial effects cannot be separated as we have done so far. The complex field at the input plane is defined by $E(x_1, y_1, z = 0, w)$. To take into account this spatiotemporal coupling we first calculate the spatial propagation for each individual wavelength with Eq. (2.10). Then we propagate the field to the output plane z=L. In order to know the spatiotemporal profile of our pulse after propagation, the spatio-spectral domain is related to the temporal domain as done in Eq. (2.6). In this way, the output field is $E(x_2, y_2, L, w)$. The spatiotemporal profile of the pulse is then given by:

$$E(x_2, y_2, L, t) = \frac{1}{2\pi} \int_{-\infty}^{\infty} E(x_2, y_2, L, w) e^{iwt} \, dw \qquad (2.12)$$

2.3 NONLINEAR PROPAGATION

Nonlinear optics studies the interaction of laser light with matter when the nonlinear polarization term of the media P^{NL} becomes relevant [50]. All kind of materials have a nonlinear behavior under sufficiently intense incident fields. However, there are some materials that are more likely to show a nonlinear response. We usually refer to them as *nonlinear materials* or *nonlinear media*. The induced modifications can be roughly divided depending on the difference between the initial and final quantum-mechanical states of the system. If there is no difference we refer to them as *parametric processes.* Second harmonic (SH) generation, self-phase modulation, self-focusing or the optical Kerr effect are examples of parametric processes. On the other hand, TPA or stimulated Raman scattering are examples of nonparametric *processes*, as the final quantum state is different compared to the initial one.

From Eq. (2.2) we can see that in the nonlinear regime the media introduces a contribution (P^{NL}) to the polarization term $P(t)$. The physical explanation is that a microscopic displacement of the bound charges is induced when a laser pulse propagates through a material. Therefore, new oscillating electric dipoles are formed and added up to the macroscopic polarization of the media [59]. The second order nonlinear interactions, those that involved the nonlinear susceptibility $\chi^{(2)}$, only occur for non-centrosymmetric media (media without inversion symmetry). As a result, $\chi^{(2)} = 0$ for liquids, gases and amorphous solids [60]. Only certain crystals, such as Beta Barium Borate (BBO), have a large second order nonlinear susceptibility and efficiently generate these processes.

In this chapter we go through the three nonlinear effects that have played a role during this thesis: SC generation, TPA and SH generation, in this order. Due to the prevalence of centrosymmetric media, we will first focus on the influence of third order susceptibility on beam propagation. A complete description of all nonlinear processes derived from non-negligible $\chi^{(3)}$ susceptibility can be found in references [50, 60]. Here we will discuss those which are more intuitive and play an active role for supercontinuum light generation.

When considering the linear and third order susceptibilities $\chi^{(1)}$ and $\chi^{(3)}$, the refractive index n of the media follows a general expression [61]:

$$n = \sqrt{1 + \chi^{(1)} + \frac{3}{4}\chi^{(3)}|E(t)^2|}. \tag{2.13}$$

The above equation can be expressed in a more convenient form to explicitly separate the linear and nonlinear contributions. Assuming that $\chi^{(1)} \gg \chi^{(3)}$ we can use the binomial expansion for Eq. (2.13):

$$n(t) = n_0 + n_2 I(t), \tag{2.14}$$

where n_0 is the usual linear refractive index ($n_0 = \sqrt{1 + \chi^{(1)}}$) , and $n_2 = \frac{3\chi^{(3)}}{4\mathcal{E}_0 c {n_0}^2}$. The term I is the intensity of the electric field $I(t) = \frac{1}{2}\mathcal{E}_0 c n_0 |E(t)^2|$. The change in the refractive index of a material in response to an applied electric field is known as the Kerr effect. The dependence of the refractive index on the intensity of the beam has a great influence on the beam dynamics through the material, resulting in effects such as the followings.

Self-focusing

Self-focusing of light is a process in which an intense light beam modifies the optical properties of the medium in such a way that the beam is focalized into the medium due to its own action over it. For this statement we assume n_2 to be positive. If a Gaussian beam is propagating through such a material, the central part of the beam, which is more energetic than the outer regions, will induce a larger refractive index at the center of the beam than at its periphery (Eq. (2.14)). Thus the material acts as a positive lens, causing the beam to come to a focus within the material [50].

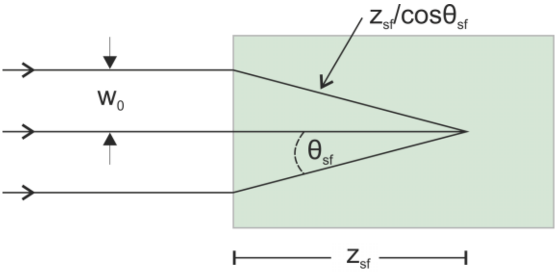

Figure 2.3. Self-focusing sketch of a beam entering a transparent medium.

This can be easily shown by means of the Fermat's principle, that establishes that a light ray, in going from point A to point B, must traverse an optical path length that is stationary with respect to variations of that path. Following this principle, the optical path length $\int n(\boldsymbol{r})dl$ of all rays travelling from a wavefront at the input face to the self-focus must be equal. As a first approximation, we now take the refractive index along the marginal ray to be the linear refractive index n_0 of the medium and the refractive index along the central ray to be $n_0 + n_2 I$. If we apply it to the case of Fig. 2.3, we get the equation $(n_0 + n_2 I z_{sf}) = n_0 z_{sf}/cos\theta_{sf}$. From this equation and taking into account the approximation of the cosine for small angles, we can derive the self-focusing angles as

$$\theta_{sf} = \sqrt{\frac{2n_2 I}{n_0}}. \tag{2.15}$$

This convergence angle θ_{sf} only considers self-focusing effect. However, the diffraction of the beam must be also taken into account in order to elaborate a more detailed model of the beam dynamics. The diffraction angle of a beam of diameter d is [50]

$$\theta_{dif} = \sqrt{\frac{0.61\lambda_0}{dn_0}}. \tag{2.16}$$

When $\theta_{sf} > \theta_{dif}$ the self-focusing effect overcomes diffraction and the beam is focused into the medium. By equalling Eq. (2.15) and (2.16) we can derive the minimum power P_{cr} needed to observe self-focusing. To do that we take into account that the power contained in the beam is given by $P = (\pi/4)d^2I$. In this way, we obtain that

$$P_{cr} = \frac{\pi(0.61)^2\lambda_0}{8n_0n_2}. \tag{2.17}$$

A direct consequence of Eq. (2.17) is the phenomenon of light *self-trapping*. Self-trapping takes place when there is an exact balance between self-focusing and diffraction of the beam. This condition is matched when the power carried by the beam reaches the critical power P_{cr} [50, 62].

Filamentation

For pulses with powers P above the critical power P_{cr} for self-focusing, the collapse of the beam to a singularity is predicted. However, the higher and higher intensities achieved by self-focusing break the electron-core bound force and a plasma is generated. This plasma entails a reduction of the local refractive index and so the beam starts to diverge again. This effect is known as *plasma defocusing*. The balanced combination of diffraction of the beam, self-focusing, and plasma defocusing can generate a "light channel" with negligible divergence characterized by a near constant beam waist over many Rayleigh lengths [63]. This effect is called filamentation of light (see Fig. 2.4). Although there are many physical effects that come into play during the propagation of the pulse in the filament [50, 60], the process of its formation can be qualitatively described by the three mentioned effects. As we will see in section 2.4.1, filamentation is accompanied by a strong spectral broadening known as SC light generation.

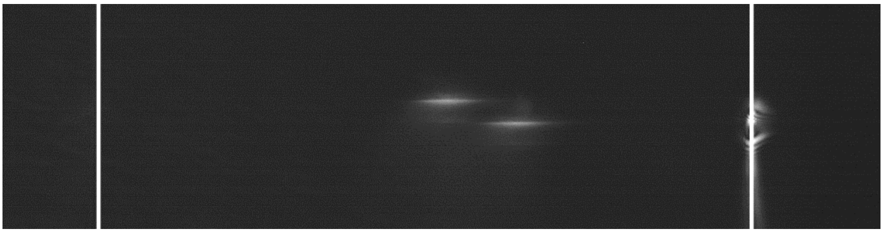

Figure 2.4. Image of two filaments at different on-axis positions generated in the bulk of a 5-mm thick fused silica sample (white bars denote the limits of the fused silica sample).

When the laser power is much higher than the critical power for self-focusing, the beam undergoes a break-up into multiple filaments. The number N of generated filaments depends on the input power P of the pulses, and can be estimated as $N \approx P/P_{cr}$ [63]. It has been demonstrated that multiple filamentation originates from transverse modulation instabilities [64, 65], thus producing a random distribution of fila ments.

Self-phase modulation

Self-phase modulation is the temporal analogue of self-focusing. The optical Kerr effect from Eq. (2.14) establishes a time dependent refractive index. In this way, the phase velocity of the propagating pulse depends on the intensity of the pulse and so the phase can be modulated by the time-domain envelope of the pulse itself (self-phase modulation) [59]. The phase of the beam after propagation of a distance L through the material is:

$$\Omega(t) = (wt - kL) = wt - \frac{wL}{c}\left(n_0 + n_2 I(t)\right), \tag{2.18}$$

and thus, the time derivative of this expression leads to the instantaneous frequency

$$w(t) = w - \frac{n_2 wL}{c}\frac{\partial I(t)}{\partial t}. \tag{2.19}$$

This can be easily understood in Fig. 2.5. The central part of the pulse sees a higher refraction index than the leading and trailing parts. By Eq. (2.19), it is translated into a red shift of the pulse in the leading part and a blue shift in the trailing part.

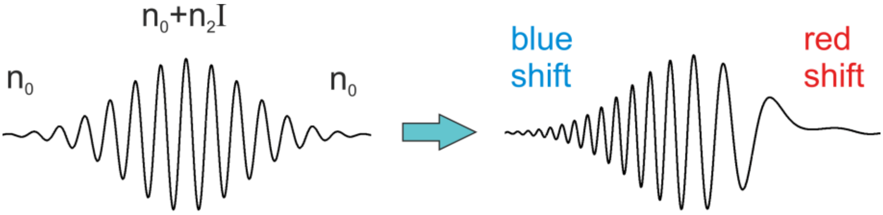

Figure 2.5. Frequency shift due to self-phase modulation.

Self-steepening

So far, we have briefly studied two main self-action effects. However there are many others with also great importance in the nonlinear interaction between a medium and the laser pulse. As an example, the group velocity of the pulse is also intensity dependent. This causes a change in the pulse envelope, known as *self-steepening*. The group velocity v_g is given by:

$$v_g = \left(\frac{\partial k}{\partial w}\right)^{-1} = \frac{c}{w\frac{\partial n}{\partial w} + n}. \tag{2.20}$$

Since the refractive index depends on the intensity distribution (Kerr effect), Eq. (2.20) means that the group velocity is slower for higher laser intensity. This causes a change in the envelope, displacing the peak towards the rear part of the pulse, and originating a steep edge. In Fig. 2.6 self-steepening is combined with self-phase modulation (Fig. 2.5). The peak displacement towards the part of the pulse where the higher frequencies are results in an increase in the production of blue-shifted frequencies.

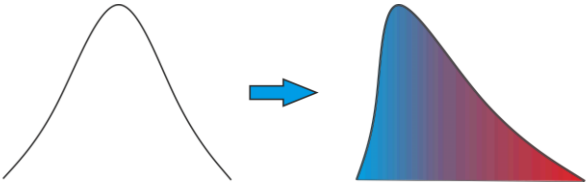

Figure 2.6. Self-steeping displaces backwards the pulse peak enhancing the blue frequencies located at the rear part (self-phase modulation).

2.3.1 Supercontinuum generation

Supercontinuum generation is one of the most spectacular nonlinear effects ever known. When an ultrashort laser is weakly focused into a transparent material, a filament can be generated and a significant spectral broadening is observed. For the case of IR pulses the spectral range of the beam can be broadened by a factor 10 (or more) leading to the appearance of a continuum emission covering the visible and extending towards the infrared region (Fig. 2.7). Although SC generation is a widely studied effect, the exact mechanisms that govern SC generation are still not clear for the scientific community. In general, it is difficult to characterize the full dynamics since the pulses undergo both temporal and spatial reshaping during the process. It is clear that the self-actions effects previously described, together with medium ionization, play an important role for SC generation. However, other processes, which are out of the scope of this Thesis, must be also taken into account for a more detailed study of SC generation: space-time focusing, four-wave mixing, Raman response, multiphoton avalanche, or tunnelling ionization [63].

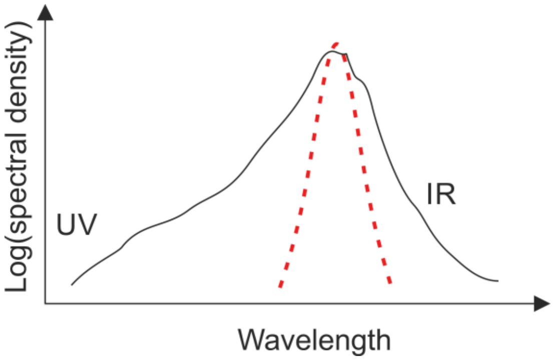

Figure 2.7. Sketch of supercontinuum generation by a femtosecond input laser pulse loosely focused. The red dotted line corresponds to the spectrum of the input pulse, while the black line is the spectrum of the SC light.

On the other hand, the influence of several macroscopic parameters on the SC generation and optical damage in different media has been experimentally studied [66-68]. The spectral broadening of the SC pulses is strongly related to the physical properties of the medium, like the band-gap [69] or material chromatic dispersion [70]. In addition, the focusing conditions of the beam affects the SC signal characteristics. When the beam is tightly focused no SC light is produced. In this sense, the numerical aperture NA becomes a critical parameter [71]. The energy coupled to each filament also influences the spectral properties of the SC signal. On the other hand, aberrations play an important role. The spherical aberration greatly influences the filament formation [72]. Chromatic aberration coming from femtosecond beam focusing with a diffractive lens allows for wavelength tunability of the SC signal by simply changing the lens-sample relative distance [73].

2.3.2 Two-photon absorption

TPA is a third-order nonlinear process in which a molecule absorbs simultaneously two photons (usually of the same wavelength). Thus, the molecule is brought to a higher electronic state [74]. Then, the molecule emits a fluorescence photon which is more energetic than those that were involved in TPA. The word “simultaneously” implies that two photons must interact with the molecule within a time interval close to the time scale for molecular energy fluctuations at photon energy scales. This is around 10^{-16} s, determined by the Heisenberg’s uncertainly principle [75]. It means that the probability for TPA to occur is very poor for low intensities: if there are only a few photons, the probability that two of them interact at the same time with the molecule is quite low. As we explain below, the use of ultrashort pulsed laser and its capability to achieve enormous peak intensities constitute a valuable tool for TPA and cross sectioning.

In reference [74] it is shown how the probability for TPA is proportional to the square intensity $I(t)^2$ of the input laser source. Hence, the fluorescence intensity $I_f(t)$ can be considered to be proportional to the molecular cross section δ_2 and to $I(t)^2$:

$$I_f(t) \approx \delta_2 I(t)^2 \approx \delta_2 P(t)^2 \left[\pi \frac{(NA)^2}{hc\lambda}\right]^2, \tag{2.21}$$

where $P(t)$ is the instantaneous laser power, c the speed of light and NA is the numerical aperture of the focusing objective lens. For Eq. (2.21) we have used the spot size of a focused Gaussian beam as the area of fluorescence emission [76]. In general, we are interested in the time average fluorescence signal $\langle I_f(t)\rangle$ over a certain period of time T:

$$\langle I_f(t)\rangle = \frac{1}{T}\int_0^T I_f(t)^2 dt = \delta_2 \left[\pi \frac{(NA)^2}{hc\lambda}\right]^2 \frac{1}{T}\int_0^T P(t)^2 dt. \tag{2.22}$$

We now develop this expression for the case of a continuous laser (CW) and pulsed laser. For a CW laser we can consider the power as constant, so $P(t)_{CW} = P_{ave}$. The sub-index "*ave*" stands for *average* power. In this case, Eq. (2.22) is equal to [74, 75]:

$$\langle I_f(t)\rangle_{CW} = \delta_2 {P_{ave}}^2 \left[\pi \frac{(NA)^2}{hc\lambda}\right]^2. \tag{2.23}$$

Now let's consider a pulsed laser with temporal width τ_p and repetition rate $f_p = \frac{1}{T}$. In this way, we can relate the average power P_{ave} of the pulsed laser with the pulse peak power P_{peak} as $P_{ave} = \tau_p f_p P_{peak}(t)$. Thus, the power of the pulsed laser $P(t)_p$ is simplified as:

$$P(t)_p = \begin{cases} \dfrac{P_{ave}}{\tau_p f_p}, & for \quad 0 < t < \tau_p \\ \\ 0, & for \quad \tau_p < t < \dfrac{1}{f_p} \end{cases} \tag{2.24}$$

From Eq. (2.22) and Eq. (2.24) we can derive an expression for the time average intensity for pulsed lasers:

$$\begin{aligned} \langle I_f(t)\rangle_p &= \delta_2 \frac{{P_{ave}}^2}{(\tau_p f_p)^2} \left[\pi \frac{(NA)^2}{hc\lambda}\right]^2 \frac{1}{T}\int_0^{\tau_p} dt \\ &= \delta_2 \frac{{P_{ave}}^2}{\tau_p f_p} \left[\pi \frac{(NA)^2}{hc\lambda}\right]^2. \end{aligned} \tag{2.25}$$

By comparing Eq. (2.23) and Eq. (2.25) we can state that the fluorescence intensity per molecule is the same for CW and pulsed lasers if the average power of the CW laser is kept higher by a factor of $1/\sqrt{\tau_p f_p}$ [75]. It means that a CW laser of 10 W will give us the same fluorescence emission intensity than a 100 MHz and 100 fs duration pulsed laser with only 30 mW of average power. Moreover, in general, the shorter the pulse duration of a pulsed laser the larger the generated fluorescence signal (for the same average power and repetition rate). The fluorescence intensity cannot be increased indefinitely, saturation of the signal arises at some point depending on the molecule characteristics like the excited-state life time [74, 75]. In this sense, the interaction of light with the sample can lead to several effects that modify the medium response to the light. Photobleaching, consisting in a photochemical alteration of the fluorophore molecules, results in the irreversible destruction of fluorescence in a defined region within the sample. The concentration of high powers in very small volumes can cause optical breakdown phenomena resulting in plasma formation and destructive thermomechanical effects [74]. Single photon absorption of the high-power infrared radiation can produce thermal damage in the sample [77]. Finally, phototoxicity [78], caused either by a direct heating of the tissue or by light activation of the fluorophore, results in the generation of reactive oxygen species that yields to structural and subsequent functional alterations in the sample.

Supposing conical illumination geometry, the excitation power falls off with the square of the distance from the lens focal point. Eq. (2.25) shows that the relationship between fluorescence signal and excitation power is quadratic. Therefore, the fluorescence signal decreases with the fourth power of distance from the focal point of the objective. In practice, it means that only the focal point region will contribute to generate 2 photon fluorescence. Because outer zones are not implicated in the excitation process, a confocal-like effect is obtained. Sub-femtoliter excitation volumes can be achieved with this technique, allowing TPA to be a good method for 3D optical sectioning.

2.3.3 Second Harmonic generation

SH generation is a nonlinear process that takes place when the photons of an input beam are frequency doubled after propagation through a nonlinear medium with second-order susceptibility [79]. This is a particular case of sum-frequency generation. It is a second order nonlinear effect, i.e., that the highest dominant susceptibility term is $\chi^{(2)}$, and thus we set $\chi^{(3)}$ is set to zero (although this term can be also relevant at the same time). For the study of the SH generation phenomenon let's consider only a monochromatic wave with no spatial dependence simplified as follows:

$$E(t) = Ae^{i\omega t} + c.c. \tag{2.26}$$

where c.c. stands for complex conjugate. We now implement Eq. (2.26) in the polarization equation from Eq. (2.2). Thus, the polarization term $P(t)$ is given by [60]:

$$\begin{aligned} P(t) = \left[\mathcal{E}_0\chi^{(1)}Ae^{i\omega t} + c.c.\right] + 2\mathcal{E}_0\chi^{(2)}AA^* \\ + \left(\mathcal{E}_0\chi^{(2)}A^2e^{i2\omega t} + c.c.\right). \end{aligned} \tag{2.27}$$

The first term of this equation is the linear contribution to the polarization. The term $2\mathcal{E}_0\chi^{(2)}AA^*$ is named the optical rectification, which is not time dependent and so creates a static electric across the nonlinear crystal. The term $\mathcal{E}_0\chi^{(2)}A^2e^{i2\omega t}$ applied to Eq. (2.1) leads to the generation of radiation at the SH frequency. The intensity of the SH signal tends to increase with the square of the intensity of the applied laser light [50].

Chapter 3. Programmable diffractive optical elements

Spatial light modulator is a term generally used to define those devices that are able to modify phase, amplitude or polarization of light waves in space and time. In the 1980s, most known SLMs were those that were placed on overhead projectors to project computer monitor contents to the screen. Nowadays, modern projectors have been developed where the SLM is built inside the projector. These kind of SLMs modulate only the intensity of an input beam. However, phase modulation of the beam is also possible with current SLMs, aimed primarily for microdisplay applications.

There are many types of SLMs depending on the addressing mode and modulation mechanism. The addressing mode makes reference to the type of input signal that modifies the optical properties of the SLM device. We can roughly identify two addressing modes: optically addressed SLM (OASLM) and the electrically addressed SLM (EASLM). For the OASLM a light image is sent and detected by a photodetector. The spatial shape and brightness of the image determine the spatial modulation of phase and amplitude at the OASLM. For the EASLM, a spatially distributed electrical signal, which is usually computer generated, modifies the medium properties allowing for incident light modulation.

On the other hand, the modulation mechanism refers to the intermediate step between addressing the SLM with an input signal and actually altering the incident light beam. We can distinguish three subgroups of light modulators depending on their modulation mechanism. In table 3.1 a comparison among them is shown. The first one is formed by deformable mirrors. The surface deformation of these mirrors allows wavefront control. The second one corresponds to digital micromirror devices (DMDs), where micrometric mirrors are rotated ±10-12°, to an on or off state. They are especially suitable for amplitude modulation. The third one corresponds to liquid crystal displays (LCDs). The use of LC materials in SLMs is based on their optical and electrical anisotropy.

	Deformable mirrors	**DMDs**	**Liquid crystal SLMs**
Modulation	Continuous, phase.	Binary, amplitude.	Continuous*, phase and amplitude.
Resolution	30-200 actuators	Full HD, 5 µm	Full HD, 8 µm
Speed	Some KHz	Up to 32 KHz	Typically 50-100 Hz
Diffraction efficiency	100%	Depends on pattern. Low for phase modulation	Up to 80%
Polarization sensitivity	No	No	Specific polarization required

*Table 3.1 Comparison between the main groups of spatial light modulators. * The modulation of SLMs is not technically continuous, as there is only a range of available phase values from 0 to 255 levels.*

As it can be seen in table 3.1, DMDs operate at high speed rates (up to several tens of KHz) and exhibits similar resolutions compared to LCDs [80]. This characteristic makes them more suitable, in terms of efficiency, for amplitude modulation than for phase modulation. Deformable mirrors offer high light modulation efficiency and no polarization sensitivity, but the resolution (typically 30 – 200 actuators) is low compared to DMDs or LCDs. On the other hand, the use of liquid crystals to build SLMs results in several advantages in terms of dynamic range, sensitivity or spatial resolution that make them our choice for phase modulation [81]. Regarding damage thresholds, deformable mirrors resist the highest energies, whereas LC SLMs are the most sensitive devices of the three mentioned to high energies. Exact damage threshold for the SLM used in this thesis can be found in the annex at the end of this Thesis.

The optical and electrical anisotropy of LCs means that the optical properties of a LC can be modified by means of an electric field allowing for spatial light modulation of an incident beam. Depending on the LC molecules arrangement inside the microdisplay cells, we can find SLMs based on vertical aligned nematic (VAN), parallel aligned nematic (PAN) or twisted nematic (TN) technologies. The main characteristics of LCDs, and LCOS in particular, are commented in the next section.

In advance, the SLMs offer the possibility to modify the beam phase at a microscale. It means that precise modifications of the beam can be implemented in order to generate arbitrary wavefronts, favoring aberration suppression. On the other hand, the programmable control of SLMs, together with their refresh rate of the order of the millisecond, enables versatile phase control almost on real time. At the end of this chapter, we propose two different experiments where the capabilities of SLMs are exploited. Both setups consist in just a SLM and a CCD, implying compactness and easy to align procedures. First, a new method for both aberration characterization and subsequent aberration suppression is demonstrated. Second, the M^2 propagation factor of a laser beam is measured by means of a SLM. In the case of the M^2 measurement, the use of a SLM and the lack of external optical devices, suppose advantage in terms of time and alignment with respect to conventional measurement methods.

3.1 PROGRAMMABLE LIQUID CRYSTAL ON SILICON SLM AND FEMTOSECOND PULSES

This section discusses the main considerations of working with electrically addressed phase-only SLMs and femtosecond lasers. This is the case of the SLM used in our laboratory, which has PAN technology. These panels are chosen as they allow for phase, amplitude or polarization modulation of high quality with large spatial resolution [81]. Moreover, with PAN displays it is possible to modulate only the phase without influence on the polarisation or intensity (phase only modulation). For the case of EASLMs, where PAN SLMs are enclosed, a pixelated electrode applies a drive signal to the liquid crystal. This interconnect problem limits the number and size of the pixels. In this sense, it is of particular interest the use of LCOS SLMs. LCOS SLMs are reflective devices where a single layer of LC is placed over a silicon chip. The control pixelated electrode array is fabricated onto the silicon itself. An operation scheme of LCOS technology is shown in Fig. 3.1. This configuration has two main benefits: the creation of big two dimensional (2D) arrays with pixel count $>10^6$, and enhanced local control due to the fact that individual pixels are typically much smaller than for a conventional liquid crystal SLM [47]. Moreover, LCOS SLMs are under active development, and the latest progresses [82, 83] in its performance aim for smallest pixel sizes (up to 4 µm), faster response time (up to 1 ms for ferroelectric liquid crystals), bigger efficiency (currently around 70-80 %) and bigger spatial resolution (up to 8000x4000 pixels).

When dealing with LCOS SLMs and typical KHz signal from a femtosecond laser amplifier some considerations must be taken into account for proper operation:

- In reference [84], Bock et al. analyse the temporal and spectral response for PAN and VAN LCOS SLMs under sub-20 fs pulsed illumination. They show that the main temporal distortion that the SLM introduces is related to the induced quadratic spectral phase of the glass substrate (see Fig. 3.1). This phase factor can be easily precompensated by a prism compressor. Neglecting this quadratic phase factor, the rest of the introduced spectral phase by the SLM is measured, resulting in a phase spectral function with very low contrast. Hence, LCOS-SLMs show an excellent temporal transfer behaviour. The pulse duration of the input beam is almost unaffected for the whole range of applied voltages.
- Some measurements have been performed to evaluate the influence of high pulse peak powers to the phase modulation behaviour of Holoeye HEO 1080P phase-only SLM [85]. The measurements, carried out for 30 fs pulses with 1 kHz repetition rate, suggest that pulse peak powers up to 20 GW/cm² (higher intensities are not tested) can be modulated without any degradation of the display and change in the performance.
- The response of the SLM is calibrated for one specific wavelength. However, when dealing with ultrashort pulses, a broadband spectrum of wavelengths is involved. For the experiments carried out in this

Thesis, the performance of our SLM for the whole spectrum of our laser can be approximated to that calibrated for the central wavelength of our laser. Aspects dealing with calibration are more carefully considered in next section.

- The electrical drive signal applied to each pixel is actually a variable amplitude wave, typically a few hundred Hz or above [47]. This results in temporal-phase oscillations that can introduce a non-uniform instantaneous deviation greater than $\lambda/5$ [86], an effect known as "flicker". The overall response of the SLM is time averaged over these fluctuations. However, for applications where time-averaging is not feasible this may be a problem [87]. It means that one pulse may "see" a different phase than the next one. Several strategies have been proposed for flicker minimization, ranging from using higher refreshing rates, cooling of the SLM [86], reducing the depth of modulation [88] or triggering of the SLM signal.
- The efficiency of the SLMs is not 100%. Therefore, depending on the SLM model, about 20% to 40% of the light will not be modulated resulting in a "zero order" that may disturb the measurement process. In this sense, the most usual solution consist in introducing a linear phase in the SLM to separate the modulated and no-modulated parts of the beam. As we will see in chapter 5, the linear phase should not be very big in order to preserve the spatiotemporal properties of the input beam.
- Crosstalk is another undesirable effect where the phase modulation of a pixel depends also on the voltage applied over adjacent pixels. The phase between two adjacent pixels with different encoded signals gradually changes from one to the other, preventing abrupt spatial variations in the phase modulation [89].

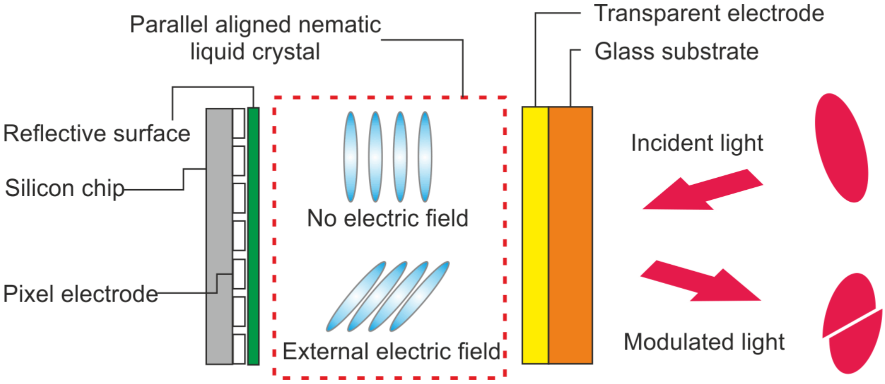

Figure 3.1 Sketch of LCOS device. The circuit to control the addressed electric signal is fabricated on the silicon itself. Incident light passes through the LC layer and is reflected back by a mirror place on top of the silicon chip. The phase of the light polarized in the same direction than the LC molecules orientation is changed via electric field control.

3.1.1 SLM calibration

Before operation, an accurate calibration of the SLM is needed for the correct use as programmable diffractive device. This is especially crucial for applications that require high wavefront control. For phase-only SLMs, the relation between the input signal, typically 256 grey levels (GLs), and the output optical phase (up to 2π or more) must be determined. Diagram from Fig. 3.2 resumes the working flow when dealing with SLMs. The GL-voltage response is stored in a look-up table (LUT). The SLM fabricant usually includes a standard LUT that the control software uses to convert GLs into the voltages applied to the liquid crystal molecules. In this sense, the calibration can be carried out either in the first conversion stage, or in the second. If the LUT remains unchanged, the user must calibrate the conversion from phase to GL in order to finally addressed to the SLM the correct phase. The resulting phase-GL calibration curve is usually nonlinear and may be some GLs that remain unused. In a second manner, the user can force a linear response between phase (0-2π) and GL (0-255) and then modify the software LUT to have the correct GL-voltage calibration curve. This last way is more convenient since all the GLs are used and the phase-GL curve is linear.

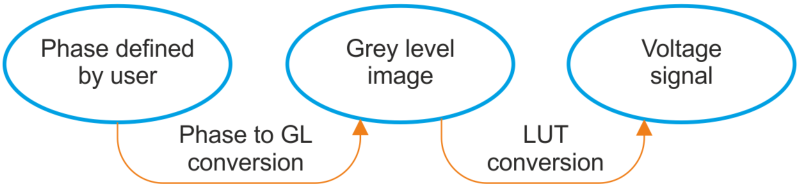

Figure 3.2 Working diagram of SLMs. The phase defined by the user is converted into grey levels (0-255) and then converted again into the voltages applied to the liquid crystal molecules. The conversion from GLs to voltages is performed via a LUT stored in the system.

In general, four factors are responsible for the need of calibration [90]: a) the existence of a global static phase $\Phi(x, y)$ due to a curvature of the SLM surface or for other possible nonuniformities caused by thickness variations of the LC layer across the aperture; b) the nonlinear response of the phase to the applied voltage $\Phi(V)$, which is explained by the nonlinear alignment of the LCs molecules by the electric field between the electrodes [84]; c) the temporal dependence $\Phi(t)$ of the phase on the addressing signal and d) the wavelength λ dependence of the SLM response $\Phi(\lambda)$: calibration is performed for a specific wavelength. Most of the calibration methods deal with the $\Phi(V, \lambda)$ dependence, i.e., they calibrate the phase to voltage response for a specific wavelength. Many times the $\Phi(x, y)$ response of the SLM is overall for the whole SLM, since the spatial phase variations are usually low and do not play an important role in most of the experiments. However, local calibration is needed when SLMs are utilized in error-sensitive applications such as holographic imaging or pulse shaping. In this way, several works have been proposed to take into account the spatial phase $\Phi(x, y)$. Xun and Cohn [91] compensated a spatially nonuniform phase-only LCOS device by adding a fixed reference phase. Joaquín Oton et al. [92] calculated a multipoint phase compensation pattern using fringe matching. In reference [93], Zichen Zhangin et al. measured and compensated spatial phase variations of a SLM by taking into account not only the effects of the spatial nonuniformity of a LCOS device, but also the dynamic phase response due to imperfections in the uniformity of the LC layer. The temporal dependence $\Phi(t)$ is related to the “flicker” effect previously commented. The influence of flicker for displaying a DOE is studied by I. Moreno et al. in reference [87]. In general, the integration times for the light coming from the SLM are longer than the phase fluctuation period due to flicker, and so the $\Phi(t)$ can be averaged and not taken into account.

Many methods have been proposed so far for SLM calibration. A review of some of these methods can be found in reference [94] and [95]. It is possible to classify them in two main categories: interferometric methods and cross-polarization methods. Interferometric methods [96-98] rely all on the same principle: the SLM screen is divided in two equal parts: one half of the SLM is scanned through the full range of phase modulation values possible while the other half of the SLM applied no phase modulation. Then, by measuring the interference fringes shift with a camera, the calibration curve is retrieved. Michelson and Mach-Zehnder type interferometers, together with opaque plates with two slits, are the most widespread configuration for interferometric methods.

Another way of calibration takes advantage of the change of birefringence as function of grey scale for amplitude modulation. For SLMs based on a nematic-electronic controlled birefringence mode, the calibration curve can be directly determined from intensity modulation measurements by using cross-polarizers [99-101]. The first polarizer sets input beam polarization at 45º relative to the axis in which liquid crystal molecules are aligned. A second polarizer called the “analyzer” is set at the same (45º) or crossed (-45º) orientation respect to the input polarization. This configuration is termed as the “intensity modulation mode” as phase variations are converted onto intensity fluctuations for calibration purposes. These fluctuation are then translated into phase shifts for calibration.

Other methods have been proposed based on other different techniques. As an example, Kohler et al. [102] apply the spread-spectrum phase retrieval (SSPR) method for SLM calibration, while Ferreira et al. [103] use lateral shearing interferometry. Calibration by using Fresnel images has been also reported [104].

In our case, calibration was performed by means of the intensity modulation method. The phase variations are converted onto intensity fluctuations for calibration purposes. Different grey level images are sent to the SLM and the optical transmittance defined as the ratio between the output and the input light intensity is found to be

$$T(GL) = \frac{1}{2}\cos(\varphi), \tag{3.1}$$

with φ the phase shift. In this way, the calibration curve $\varphi = f(GL)$ is theoretically expressed through

$$\varphi = cos^{-1}[2T(GL)]. \tag{3.2}$$

Fig. 3.3 shows the calibration curve for the amplification stage of our pulsed laser for λ=800 nm, in which just a limited range of gray levels, chosen from a convenient interval within the [0, 255] scale, is needed to get the required 2π phase modulation. In Fig. 4 of reference [**I**] the calibration for the PLUTO VIS-NIR modulator is shown for λ=633 nm.

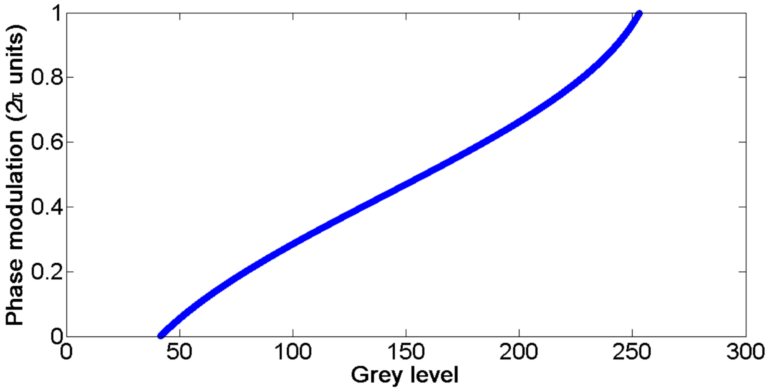

Figure 3.3 Phase modulation versus grey level. It is not necessary to use the full 256 grey level scale to achieve a 2π phase modulation.

3.2 FOCUSING WITH A SLM

Liquid-crystal displays working as electronically addressed SLMs have been widely used to generate programmable diffractive lenses [105] and the mathematical models to encode the lens function in a device constrained by its pixelated structure and phase quantization analyzed [106, 107]. In order to focus the beam, a quadratic phase factor $\Phi(r) = kr^2/2f$ corresponding to a diffractive lens (DL) is encoded onto the SLM. The focal length is f, with k the wavenumber and r the radial coordinate on the SLM pupil. As function $\Phi(r)$ increases with the increasing of the radial coordinate, the phase factor easily exceeds 2π modulation. Most of the SLMs only reach 2-3 π modulation. So, in practice, the SLM displays the phase wrapped in 2π steps [108] (see Fig. 3.4a). Moreover, the phase $\Phi(r)$ cannot be wrapped continuously: the pixelated nature of SLMs gives place to the stepped structure from Fig. 3.4b.

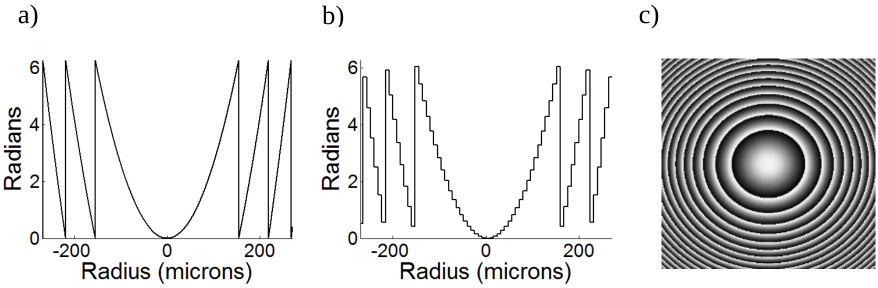

Figure 3.4 a) Phase profile for a lens with f=15 mm and wavelength λ=800 nm, b) phase profile with the same parameters than previous but for a "stairstep" function corresponding to a SLM with pixel size 8 μm, and c) Phase map corresponding to a diffractive lens. The fringes are concentric rings with increasing phase from 0 to 2π. Fringes width decrease with the increasing of distance to the center what can produce aliasing.

Thus, the pixelated nature of SLMs, together with its limited size, impose some restrictions for the phase codification. The phase wrapping may lead to aliasing in the outer regions of the lens since the width of each wrapped zone decreases with the increasing of the distance to the center. A detailed mathematical model that describes the behaviour of lenses encoded in a low-resolution device can be found in Ref. [106]. In short, Carcolé et al demonstrated the existence of an optimum focal length for best lens performance in terms of the FWHM focal distribution for a given codification device. The key point is to define blocks of pixels that always contribute constructively to the focal intensity. For current pixel size in the μm range, the FWHM spreading at the focal plane is remarkably low for focal lengths extending from a few millimeters to several centimeters. In a simplified model, the focal length of the encoded lens consisting of several Fresnel zones is directly related to the outermost zone width, Δr, and the lens diameter, d, through $f=d\Delta r/\lambda$. In practice, the outermost zone must be displayed with at least two pixels to avoid aliasing, so Δr actually equals the pixel size. This reduces the focalization efficiency of the outer zones to about 40% [109]. In addition, if clipping of the laser beam may be avoided, the lens diameter should be adjusted to several times the beam width over the SLM. Focusing artifacts (such as multiple focal lengths and higher-order diffractions) due to the pixelated and the quantized nature of the SLM must be also taken into account. The typical grey level image sent to the SLM for lens codification is displayed in Fig. 3.4c.

So far, we have seen the radial dependence of the lens efficiency due to pixelation. Therefore if a constant response over the whole encoded lens is needed, the amplitude of the complex mask should change radially to compensate for the mentioned efficiency loss. The wrapped phase $\Phi(r)$ ranges from 0 to 2π. In order to gain control over the energy coupled in the focus for a encoded lens, $\Phi(r)$ is multiplied by α. The parameter α varies from 0 to 1 and allows for the control of the diffraction efficiency of the lens [110]. In this way, the new encoded phase is

$$\Psi(r) = \alpha(r) mod\left[\frac{kr^2}{2f}, 2\pi\right]. \tag{3.3}$$

The operator *mod(a,m)* returns the remainder after division of a by m, where a is the dividend and m is the divisor. It indicates that the phase is wrapped in 2π steps. The parameter $\alpha(r)$ has been intentionally made dependent on the radial coordinate r. However, it can be the same for the whole encoded phase. When the efficiency of the whole lens wants to be modified in a constant way, $\alpha(r)$ will be constant **[V]**. When, for example, the efficiency of the outer zones must be changed with respect to that of the inner zones, $\alpha(r)$ will vary with r **[II]**. For α =1 nearly all the light reflected of the lens is directed into the focus. However, for α<1 the energy coupled to the main focus is reduced. The relation between the value of α and the corresponding efficiency η for the generated pattern is given by [110]:

$$\eta = sinc^2(\alpha - 1), \tag{3.4}$$

where $\mathrm{sinc(x)} = \mathrm{sin(\pi x)}/\,(\mathrm{\pi x})$.

In the following sections, we take advantage of the reprogrammable nature of SLMs to propose new methods to characterize the aberration of the beam and its M^2 propagation factor. This is done, for all cases, with a very simple setup consisting in a SLM plus a CCD.

3.3 WAVEFRONT RETRIEVAL USING AN ANNULAR LENS

Wavefront aberrations of a laser beam are spatial phase distortions that play a major role when focusing the laser to a high-quality focal spot. Defocusing, astigmatism or comma are examples of well-known aberrations introduced by the human eye [111-113] that usually require of active correction (typically surgery or lenses). Wavefront aberrations originated by imperfections, misalignments and stress of the optical mounts in the chains inside femtosecond amplifier systems enlarge the focal spot. In this sense, it is well-established that the measurement and the correction of wavefront aberrations of the laser pulse is crucial for high quality focusing [114-116].

3.3.1 Characterization of wavefront aberrations

The characterization of the wavefront aberrations is expressed in mathematical terms by means of the Zernike polynomials. These functions, usually defined in polar coordinates (ρ, θ), are normalized to the unit circle. The radial coordinate ρ ranges from 0 to 1, and θ from 0 to 2π. Each of the Zernike polynomials, defined by two index numbers (n, m), consists of three components: a normalization factor, a radial-dependent component and an azimuthal-dependent component. Thus, the Zernike polynomials $Z_n^m(\rho, \theta)$ are defined as [117]:

$$Z_n^m(\rho,\theta) = \begin{cases} N_n^m R_n^m(\rho)\cos(m\theta), & for \quad m \geq 0 \\ N_n^m R_n^m(\rho)\cos(m\theta), & for \quad m \geq 0 \end{cases} \tag{3.5}$$

where N_n^m is the normalization factor, and R_n^m the radial component of the polynomials (see reference [117] for definitions). There are several different implementations of Zernike polynomials depending on the normalization, coordinate system and ordering. In this Thesis, Zernike polynomials are considered as it is established by the *Z80.28-2009-American National Standard for Ophthalmics* [118], which is also consistent with reference [117].

Several phase measurement methods have already been proposed and demonstrated. The most popular is the Shack–Hartmann wavefront sensor (SHS) where the measurement of the local phase slopes of the wavefront provides the entire beam phase [115, 119-122]. This technique requires a microlens array that divides the pulsed beam into a number of beamlets. An outline of SHS operation is included in Fig. 3.5.

Wavefront measurement and reconstruction are unambiguously defined only for monochromatic radiation. However, the SHS has been investigated for the case of broadband laser pulses (spectral bandwith larger than 100 THz) [123]. It was demonstrated that SHS can be used to accurately measure broadband pulse wavefronts. The wavefront retrieved for the whole spectrum of the laser is in good agreement with wavefront resulting from the individual sum of the monochromatic wavefronts that form the pulse, each balanced with a factor given by the corresponding normalized spectral irradiance of the laser beam. Based on this measurement, the numerical propagation of the laser pulse's wavefront can be calculated and it is accurate. For instance, SHS has been implemented to test the temporal stability of pulsed laser beams [124].

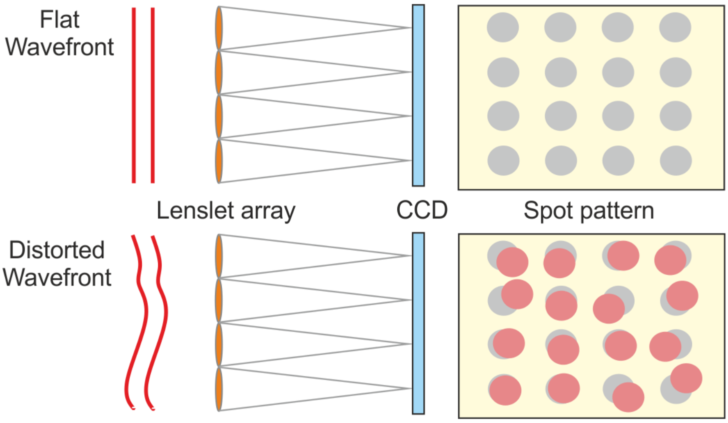

Figure 3.5. Shack–Hartmann wavefront sensor operation diagram. The input wavefront is focused onto a CCD screen. For the case of the distorted wavefront, the spatial deviation of the foci with respect to those of the flat wavefront is used to measure the aberrations carried out by the beam.

3.3.2 Experimental results

We have developed a novel technique for wavefront retrieval of short pulses coming from commercial amplifier systems running at mJ energy levels and temporal pulse durations at tens of femtoseconds **[VI]**. To implement our method, only an SLM and a camera are needed (Fig. 3.6), preventing the use of external wavefront sensors. This method provides accurate results even when implemented with low dynamic range cameras.

The input wavefront is measured at the SLM screen plane. To do that, we first generate the phase profile $\Phi(r) = kr^2/2f$ corresponding to a converging diffractive lens. To avoid aliasing at the outer regions of the lens we encoded a DL of 130 mm of focal length for 800 nm in the SLM. At the same time, this lens function is decomposed into N concentric rings that tile the whole active area of the SLM. The election of the width and number N of concentric rings is explained later. Then, each concentric ring is encoded onto the SLM in a sequential way. For each ring, the corresponding focused irradiance is recorded with the camera. It is important to mention that for the zone of the SLM where there is no ring, a phase pattern corresponding to a diverging lens is encoded in order to eliminate the contribution at the focus from that part of the SLM. In Fig. 3.7a the irradiance pattern is shown for one of the rings. The deviation from the expected Airy pattern suggests the presence of aberrations on the beam.

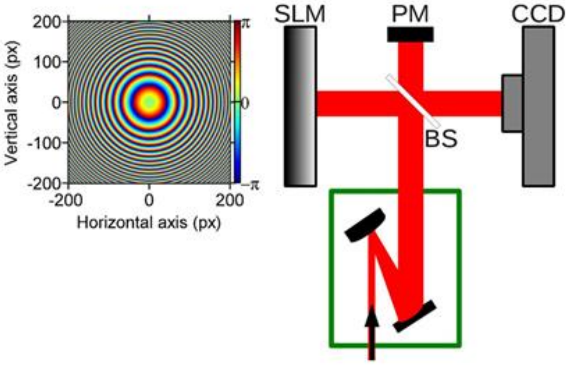

Figure 3.6 Experimental setup used for the SLM calibration, aberration measurements and M^2 propagation factor measurement. The beam is generally expanded to fill the SLM screen to user specification. A beam splitter (BS) is used to work at normal incidence, and a power meter (PM) is placed to measure the average power of the beam when needed (replaced by a beam blocker if not needed).

By means of a least-square fitting procedure, the phase and amplitude distribution of the input beam over the SLM plane is retrieved for each ring (see Fig. 3.7c and 3.7d). For the fitting procedure, the angular variation is parameterized at a number of reference points (12 for amplitude and 12 for phase) uniformly distributed at the SLM plane for subsequent spline interpolation. One of the 12 phase elements was fixed to remove the insensitive effect of a global shift in the absolute phase. To ensure that the fitting procedure is self-consistent, the ring position and the width were added as free test parameters. The intensity distribution at focus derived from each set of intensities and phases was calculated through the Fourier transform. The ring position and the width test parameters were checked in each reconstruction and were in agreement with the segmentation used in the experiment. Based on the retrieved phase and amplitude, the intensity of the beam is theoretically calculated at the CCD plane and compared with the experimentally recorded (see Fig. 3.7b). Good agreement between simulation and experiment was found for all the cases.

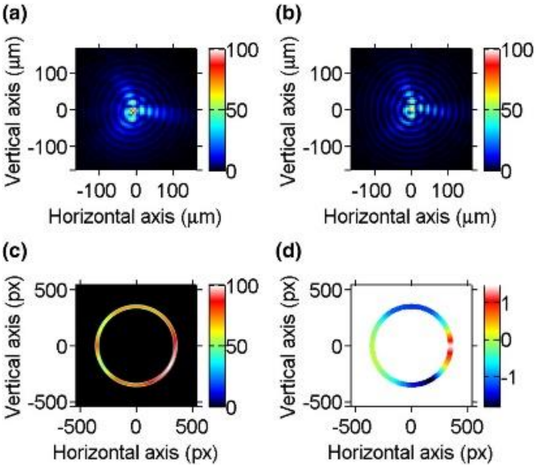

Figure 3.7 Phase recovery procedure for a ring-shaped zone (10th ring) over the SLM plane: a) experimental measurement of the focal irradiance; b) calculated irradiance distribution from the fitted phase; c) retrieved intensity which for our experiment is almost uniform; d) retrieved phase.

The ring-based wavefront retrieval is of particular interest for the QDST pulse shaper **[II]** that we will see in chapter 4. Each zone corresponds to a circular ring whose inner, r_{in}, and outer radius, r_{out}, were chosen in such a way that the propagation time difference (PTD) for pulses originated at the two edges of the zone to the geometrical focus is smaller than the femtosecond pulse width. This PTD can be calculated by the formula $\left(r_{out}^2 - r_{in}^2\right)/(2fc)$ [125, 126], which is derived in chapter 4. In our experiment, we considered a PTD of 22 fs, i.e., the area of each ring was 5.32 mm^2. In addition, we chose an approach based on ring overlapping. This means that one zone overlapped with the following by a distance equivalent to half of the PTD. With the above parameters, the total number of rings employed was N = 23.

The key point in our pupil segmentation method is to take into account the broadband nature of short pulses to focus light nearly free of chromatic artifacts. As mentioned earlier, the broader the spectrum of the laser the higher the number of ring-shaped zones needed in the procedure. Following the generalized Huygens-Fresnel diffraction integral, the monochromatic depth of focus (DOF) for an annulus ring of a DL can be expressed by the formula $1{,}76 f^2 \lambda_0 / \left(r_{out}^2 - r_{in}^2\right)$. With the above mentioned area of 5.32 mm^2, the DOF for the central wavelength is equal to 14 mm. On the other hand, the effective focal length dependence of the diffractive lens on the wavelength generates a longitudinal chromatic aberration of the focusing system for ultrashort pulses. The chromatic aberration can be taken into account by the expression $f(\lambda) = f\lambda_0/\lambda$. Considering a pulse with 50 nm of bandwith at FWHM, the spatial separation among foci (longitudinal chromatic aberration) for different wavelength is then 8 mm. Whenever the DOF is longer than the longitudinal chromatic aberration of the focusing system we will be able to record with the camera structures close to the Airy pattern. Then, the retrieval process will be more accurate. The ideal number of rings corresponds to that which allows us to recover a structure close to the Airy pattern for each ring.

In Fig. 3.8, the intensity corresponding for 3 different rings is studied. The phase distribution corresponding to several ring-shaped zones used in the experiment can be found in Fig. 3.8a–c. The focal irradiance measured with the camera for the corresponding rings are in Fig. 3.8d–f. Contribution of the innermost zone of the DL (ring 1) corresponds almost to the Airy pattern as can be seen in Fig. 3.8d. However, as expected, the output pattern recorded by the camera differs more from the ideal theoretical focal distribution of a homogeneous annulus for the outermost zones of the lens. This effect, attributed to the optical aberrations, have a strong dependence with the radial coordinate and prevents us to obtain a high-quality Airy spot when the whole area of the SLM is used to focus the beam. Once the phase is retrieved for each ring, the complex conjugate phase is sent to the SLM and the intensity patterns measured again. In Fig. 3.8g–i, the results for the focal irradiance distribution generated by the above zones after wavefront sensing and compensation are showed.

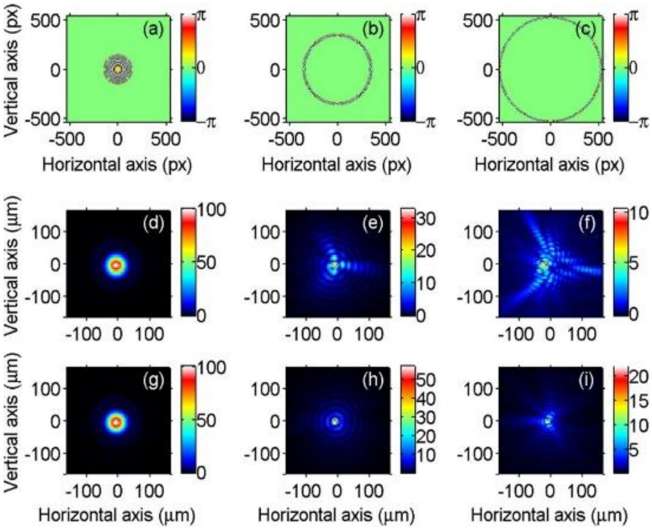

Figure 3.8 a–c Phase transmission function encoded in the SLM corresponding to a DL with only one ring active, in particular the 1st, 10th and 23rd, respectively. The measured irradiance in the focal plane for each ring without (d–f) and with g–i wavefront correction

To compare our results, we also calculated the aberrated wavefront with the Fresnel phase retrieval method using the conventional iterative fourier transform algorithm (IFTA) [127, 128]. We considered that the intensity over the SLM was constant and measured the focal irradiance pattern generated by the whole DL. In the iterative calculation, we analyzed the convergence of the algorithm by measuring the root mean square (rms) error between the image in the focal plane measured with the camera and the reconstructed image. The retrieved phase over the SLM pupil in our case is shown in Fig. 3.9a. The phase for the conventional IFTA method is shown in Fig. 3.9b. Visual differences between both images are quantified by measuring the Zernike coefficients for each method. This is shown in Fig. 3.9c, where we have omitted the constant and the linear phase terms as they do not provide relevant information (Z_0^0, Z_1^{-1} *and* Z_1^1 Zernike polynomials).

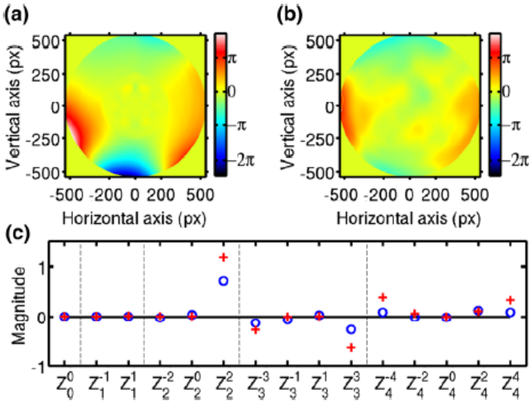

Figure 3.9 Spatial phase reconstruction performed with the Fresnel phase retrieval a) with annular lens array, and b) with the full area. The Zernike coefficient corresponding to the method shown in a) (plus symbol) and method shown in b) (circle) are displayed in c.

3.4 M^2 BEAM QUALITY FACTOR MEASUREMENT

Finally, the potential of the SLM+CCD is used to measure the M^2 beam propagation factor of a laser beam **[I]**. The M^2 provides a measurement of the deviation of the beam with respect to that of a TEM_{00} Gaussian beam due to contributions from higher-order transverse modes, truncation or other distortions introduced by lenses, apertures, or other optic systems. The setup for this experiment is the same to that of Fig. 3.6. However, in this case the CCD is replaced by a beam profiler to automatize beam radius measurement.

The determination of the beam propagation factor is crucial for both scientific and industrial fields. The ISO standard (ISO/DIS 11146) provides a convenient method for measurement. In this technique, the laser beam to be evaluated is relayed through a lens in a fixed position and multiple beam-width measurements are made along the waist region behind the lens [129]. Finally the beam propagation factor is obtained through the fitting of the experimental data. The beam width is measured in agreement with the second-order moment criterion. This method involves mechanical scanning of the intensity sensor along the beam propagation direction. In practical terms, this requires a high degree of alignment and parallelism. Also, the measurement is time-consuming (of the order of tens of seconds) and thus, sensible, to environmental fluctuations and beam changes.

The same idea can be performed by means of a SLM. In our approach, a set of lenses with tunable focal length is encoded sequentially onto the phase-only liquid crystal SLM. A variable quadratic-phase factor in the spatial domain displayed on the SLM plays the role of the programmable lens. Whenever the focal length is changed, a different axial plane is imaged onto the beam profiler, which is kept at a fixed position. In this way, a complete digital control of the measurement system is attained without the need of any moving component as a main difference with the ISO standard procedure.

On the other hand, for a fixed distance z between the SLM and the beam profiler, the squared rms of the light pattern depends on the focal length as:

$$\sigma_s^2 = a + \frac{b}{f} + \frac{c}{f^2}, \tag{3.6}$$

where a, b and c are fitting parameters that can be easily related to the actual beam parameters of the incident beam through

$$M^2 = \frac{4\pi}{\lambda z^2}\sqrt{ac - \frac{b^2}{4}}. \tag{3.7}$$

In this way, the M^2 can be calculated measurement with no need of moving-elements. We measured the beam propagation factor of a commercial He-Ne laser (λ=632nm, 20mW) emitting a TEM_{00} mode with linear polarization as a coherent beam source and beam diameter of about 2 mm. An example of the data for the squared beam radius against the focal length displayed onto the SLM is plotted in Fig. 3.10.

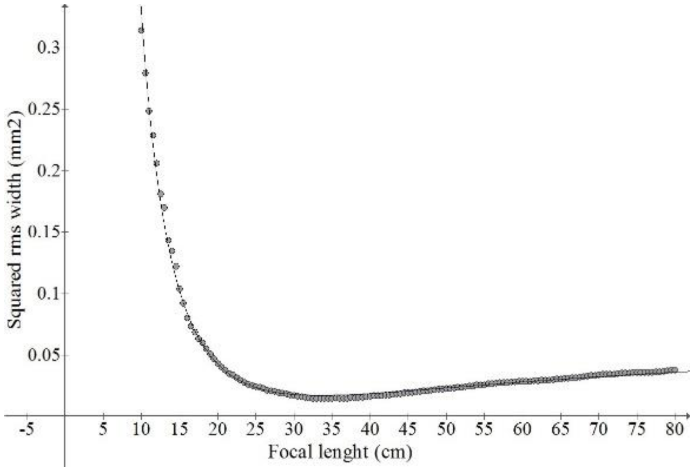

Figure 3.10 Experimental results for y axis

The beam profiler was fixed at a distance of 43.5 cm from the SLM. We oversampled the focal length range between 10 cm and 80 cm with 140 sampling points. Focal lengths variations of a few millimeters generate focal distributions with a detectable focal depth in terms of the CCD pixel size. For the free-motion method a hyperbolic fit yields values for the M^2 of 1.12/1.15 in horizontal/vertical direction of the laser, respectively. The effort for a complete measure (140 sampling points) lasted around 10s. This time interval is shortened if the number of sampling points is reduced according to the ISO standard (10). The results for the beam propagation factor following the ISO approach were 1.07/1.08 in horizontal/vertical directions after mechanical scanning of the beam profiler along the propagation direction. Thus a concordance level of less than 5% between both methods is found. Yet, the accuracy of both methods is comparable and mainly determined by beam profiling measurement accuracy.

Chapter 4. Temporal shaping

User-defined temporal waveforms in the femtosecond regime with control of phase, amplitude, or polarization are a pre-requisite in many experiments. In particular, programmable pulse shaping in the temporal domain has served as an enabling technology for a broad range of applications, both in ultrafast science and technology, and a great review of them can be found in references [46, 47]. Some examples of applications that benefit from pulse shaping techniques are: quantum control of chemical reactions [130], selective enhancement of high harmonic (soft X-ray) radiation from atoms driven by strong laser fields [131], spectrally selective nonlinear microscopy [132, 133], or dispersion compensation in fiber optics [134], optimized compression of pulses in the single cycle regime [135], and the generation of high power pulses from chirped pulse amplifier systems [54].

The short duration of femtosecond pulses prevent the use of electronic devices for direct pulse shaping purposes. So far, no signal is capable to induce pulse modulation with sub-fs resolution to modify the pulse directly in the time domain. Instead, pulse shaping is usually performed in the frequency domain. The frequency and time domains are related via the Fourier transform, so the basic idea is to introduce controlled modifications to each frequency component of the pulse in order to induce a change in its temporal profile. This is usually achieved through a space-to-time transformation, where spatial masking of an optical beam causes its temporal modulation. This is the case of the widespread Fourier-transform pulse shaper, first proposed by A.M. Weiner for femtosecond lasers [52]. In Fig. 4.1 a sketch of the pulse shaper is shown.

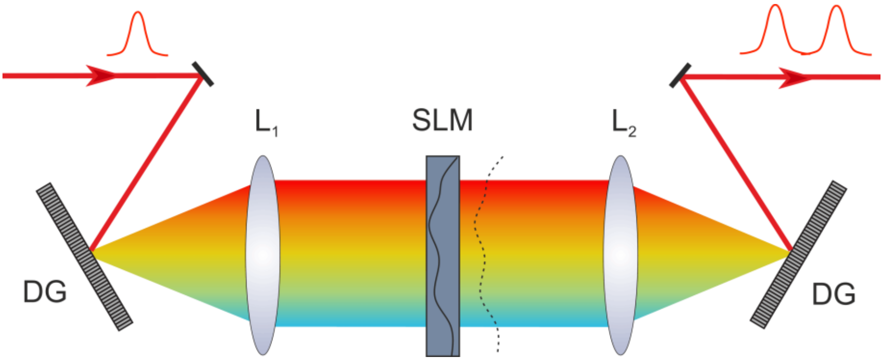

Figure 4.1 Fourier (frequency domain) pulse shaper. The input pulse is dispersed by a first diffraction grating (DG) and collimated by the lens L_1. The beam reaches the SLM where a phase mask is encoded in order to manipulate each individual frequency component of the pulse. A second lens and DG recombine the shaped beam at the output of the pulse shaper.

For this method the individual frequency components are angularly dispersed by a diffraction grating, and then focused to small diffraction-limited spots at the back focal plane of the first lens (L_1). Then, by placing an appropriate amplitude and phase mask at this plane, the amplitude and phase for each one of the spectral components is manipulated. The mask is usually displayed onto a dual programmable SLM, allowing for versatile shaping of the pulse. Finally, a second lens (L_2) and grating recombine all the frequencies into a single collimated beam and a shaped output pulse is obtained, whose pulse shape is given, in essence, by the Fourier-transform of the pattern transferred by the mask onto the spectrum. L_1 and L_2 are usually cylindrical lenses.

It is also worth to mention other popular technology for femtosecond shaping termed AOPDF, from Acousto-optic programmable dispersive filter. The operation principle is quite different to that of the Fourier-transform pulse shaper, but it is equally based on the idea of individual frequency modulation. The AOPDF performance relies on a longitudinal interaction between a polychromatic acoustic wave and a polychromatic optical wave in the bulk of a birefringent crystal [54]. Two optical modes can be coupled efficiently by acousto-optic interaction only in the case of phase matching. The input optical pulse is initially travelling through the ordinary axis of the crystal. Every frequency *w* travels a certain distance before it encounters a phase-matched spatial frequency in the acoustic grating (see Fig. 4.2 below). At that position part of the energy is diffracted into the extraordinary axis. As the velocities of the ordinary and extraordinary modes are different, each frequency will see a different time delay. The amplitude of the output pulse is controlled by the acoustic power at each position.

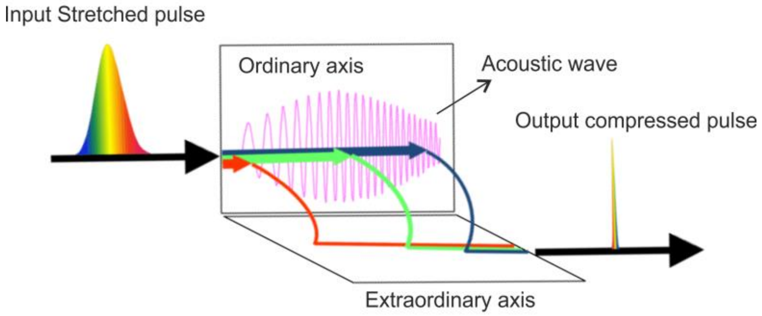

Figure 4.2 Schematic of an AOPDF. At certain positions of the ordinary axis, the condition of phase matching between the optical wave and the acoustic wave is fulfilled and each optical frequency is diffracted to the extraordinary axis. It introduces a time delay between the optical frequencies and shaping of the pulse is achieved (for pulse compression in this figure).

However, other different approaches for ultrafast shaping have been developed in order to give response to different user requirements, such as more compact, dynamic or fast-operation setups. In this sense, the direct space-to-time (DST) pulse shaper [136] or the QDST [125, 126] are alternatives that fulfil the previous requirements and have been used in many different experiments: study of molecular alignment [137], generation of fractal pulses [138] or bandpass optical filters [139, 140]. Both methods are based on two different DOEs, the diffraction grating for DST and the DL for QDST. The advantages of these approaches are the compactness of the setups, as the Fourier-transform of the spatial patterns is not needed. This fact makes possible the generation of pulse shapers consisting only in a SLM where a determinate phase mask is encoded **[II]**. Therefore, user-define shaping can be achieved on real time through a computer connected to the SLM.

4.1 PROGRAMMABLE PULSE SHAPER

Looking for robustness, compactness and easy-to-align programmable pulse shapers, we have developed a QDST pulse shaper that can be reduced to a simple phase mask encoded onto a SLM **[II]**. In such a proposal, the entire size of the pulse shaper is very small, there is almost no need for optical alignment, and obviously no extra refractive focusing elements are required. The basis of the QDST method can be easily explained by using geometrical optics in the paraxial approximation. In order to demonstrate it, let's suppose that we encode a quadratic phase factor corresponding to a diffractive lens of focal length *f* in a SLM (same than Eq. (3.3) with α=1). For the femtosecond pulses that reach the SLM, there will be a PTD among pulses coming from different parts of the encoded mask. This is due to the optical path difference between the rays, as shown in Fig. 4.3.

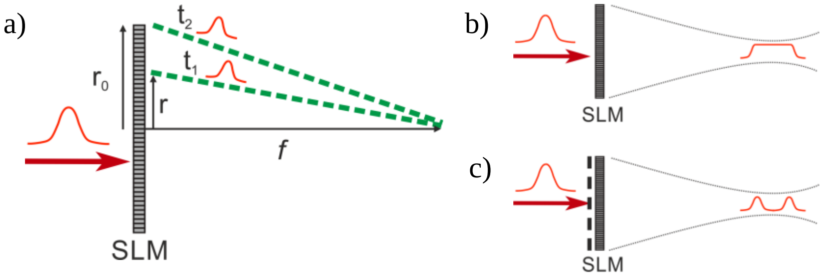

Figure 4.3 a) Optical paths for two pulses coming from different parts the SLM, where a focusing mask of focal length f is encoded, b) the temporal profile of the pulse is broaden due to different arrival times to the focal point (PTD), and c) properly blocking certain parts of the SLM may arise to modulate the temporal shape of the pulse at the output.

The time difference $\Delta t = t_2 - t_1$ between pulses coming from the radial positions r and r_0, can be calculated based on the geometrical path differences between both of them. Considering that the group velocity of the pulses equals c, we can write:

$$t_2 - t_1 = \frac{f}{c}\left(\sqrt{1+\frac{r_0^2}{f^2}} - \sqrt{1+\frac{r^2}{f^2}}\right). \tag{4.1}$$

In the paraxial approximation $f >> r_0$, so we can approximate the square root in terms of the Taylor series as $\sqrt{1+x} = 1 + \frac{1}{2}x$ (valid for x<<1). Thus, the time difference Δt between pulses at the focal spot can be expressed as:

$$\Delta t = \frac{r_0^2 - r^2}{2fc}. \tag{4.2}$$

From the above equation, we can calculate the temporal window of the pulse shaper by making $r = 0$. In this sense, the temporal window defines the available temporal range for pulse shaping. Eq. (4.2) means that the temporal window can be enlarged in 2 different ways: making r_0 as big as possible or making f as smaller as possible. For the first option, we are limited by the finite size of the SLM. In our case, it imposed a practical limitation of $r_0 = 4.3\ mm$ to the radial extension of the phase mask. For the case of reducing f we have other type of limitation. It is the pixelated nature of SLMs. The finite number of pixels of the SLM causes the efficiency of the encoded DLs to depend on the radial coordinate. This unwanted effect originates a modulation in the temporal response of the QDST pulse shaper, decreasing the peak intensity of the shaped pulses coming from the outer zones of the encoded DL. For longer focal lengths the above-mentioned dependence can be turned off, but unfortunately in these cases the temporal window of the QDST pulse shaper is also reduced. Taking this into account, we codified a DL with focal length of 135 mm, which corresponds to a temporal window of about 230 fs. In this case, the phase of the outermost ring of the DL is encoded with only two phase levels.

The experimental setup is shown in Fig. 4.4. For the experiment we used the amplifier output of our FemtoPower compact Pro Ti:sapphire femtosecond laser (see annex). It is important to note that the pulse shaper consists only on a SLM. The rest of the elements corresponds to a cross-correlation setup for pulse characterization. Cross correlation provides a good approximation about the tailored intensity profile, but no phase information is available. At the entrance of the interferometer, the light coming from the ultrashort laser source is split with a pellicle beam splitter (BS_1) into two pulses: the reference pulse and the shaped pulse. The latter is first expanded via 4x all-mirror beam expander (BE) and sent, using a second beam splitter (BS_2), to the phase-only SLM, where the phase mask of the QDST pulse shaper is encoded. The reference pulse is a replica of the initial ultrashort pulse and it is inserted in a delay line, whereas the shaped pulse has the desired temporal profile. The delay line allows us to vary the path length of the reference pulse.

The shaped and reference pulses are spatially and temporally overlapped into a BBO type I crystal of 70 µm thickness. In our case, the crystal is thin enough to ensure a phase-matching process without loss of spectral components. The reference pulse is focused by means of a pair of refractive lenses (L_3), with an equivalent focal length of 250 mm. Since the length of bulk material is approximately the same in both arms, the effects of group-velocity dispersion were pre-compensated with a prism pair at the post compression stage of the laser. By recording the intensity of the central SH signal for each position of the delay line, the approximated intensity profile of the shaped pulse is determined (temporally stretched by the convolution with the reference pulse). In order to select the SH signal generated only in the close vicinity of the DL focus, we formed a 2x magnified image of the BBO crystal plane onto a CCD camera with a telescope composed of lenses L_4 and L_5.

The phase encoded to the phase-only SLM is that which allows contribution from focusing rings and blocks the light from the rest of the SLM:

$$\Phi(r) = \Psi(r) - \varphi_{SP} = \alpha(r) mod \left[\frac{kr^2}{2f}, 2\pi\right] - \varphi_{SP}. \qquad (4.3)$$

As seen in Eq. (3.3), the phase $\Psi(r)$ is that of a diffractive lens with efficiency correction. The efficiency factor $\alpha(r)$ is equal to 0 in those zones of the mask that must be blocked to avoid light contribution from those areas (in practice, the phase of a diverging lens is encoded in these areas). To compensate the radial dependence of the efficiency of the encoded DLs, the transmission term $\alpha(r)$ is radially modified in order to shape the relative height of the generated train of pulses. The quadratic phase factor is calculated for the central wavelength of the amplifier system of our laser, and for the mentioned focal length f=135 mm, chosen to keep the compromise between the biggest possible temporal window and codification of the outer zones of the SLM. In this proposal, the pulse shaper consists only in a phase mask encoded in the SLM, which makes it programmable. By purely phase modulation, different parts of the beam are blocked or focused. Previous proposals were based on the same principle, but using a bulk mask to radially block the beam and a diffractive lens to focus [125].

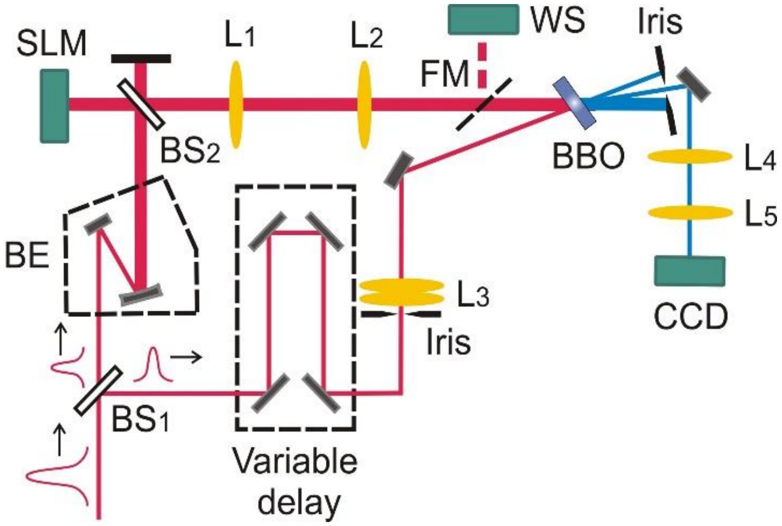

Figure 4.4 Sketch of the experimental setup. The pulse shaper consist in just the SLM. The rest elements are part of the measurement system to characterized the shaped signal

The introduction of the phase φ_{SP} in Eq. (4.3) has a different explanation. In practice, wavefront aberrations play an important and undesirable role. In Fig. 4.5a the SH irradiance patterns at the BBO crystal plane for the outermost ring zone of the DL is shown. It is clear that the expected Bessel like pattern is completely lost because of the presence of aberrations, and so the temporal pulse shaper cannot be implemented. For this purpose, we deviated the shaped pulse before the BBO crystal using a flip mirror (FM) (see Fig. 4.4), and sent it towards a commercial Shark-Harmman wavefront sensor (WS), where the spatial phase φ_{SP} at the SLM plane was measured. Therefore, we add the phase $-\varphi_{SP}$ to Eq. (4.3) to compensate from these aberrations. In Fig. 4.5b, the compensated irradiance SH pattern is shown.

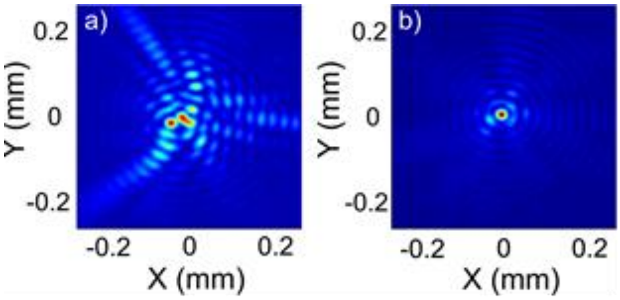

Figure 4.5 SH irradiance patterns at the BBO crystal plane for the outermost ring zone of the DL, without a) and with b) wavefront correction.

In Fig. 4.6, three different examples of temporal profiles obtained with the QDST pulse shaper are shown. The first case, see Fig. 4.6a, is a sequence of two pulses of equal peak intensity, delayed 200 fs between them. The temporal width of the shaped pulses, considering their convolution with the reference pulse, is about 80 fs intensity FWHM. The second example shown in Fig. 4.6b corresponds to the same temporal profile, but different relative peak intensity between pulses. Finally, the third case is a sequence of three pulses with slowly decreasing peak intensity, see Fig. 4.6c. The limited spatial size of the SLM, together with the temporal width of the initial ultrashort pulse, establish the maximum number of pulses that can be synthesized. The temporal window of the programmable QDST pulse shaper could be also increased in the near future when technological advances allow for SLM with larger working area as well as smaller pixel pitch. This is not the case for static phase masks, were the available techniques (e.g., photolithography) can achieve several centimetres for the mask size while keeping high spatial resolution. However, photolithographic masks do not allow for dynamic temporal shaping.

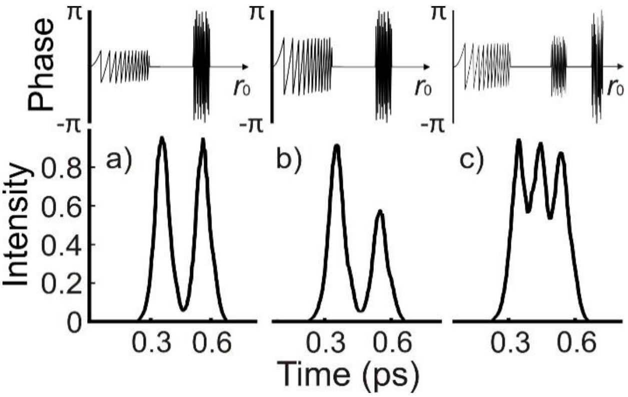

Figure 4.6 Intensity cross-correlation measurements of temporal profiles synthesized by the QDST pulse shaper (bottom). Example of a radial phase profile of corresponding masks (top).

Chapter 5. Transversal spatial shaping

SLMs are an essential tool for modulation and analysis of light. Up to now, they have been extensively studied to modify the temporal profile of ultrashort pulses. Such is the case of the examples shown in the previous chapter: the Fourier transform pulse shaper or the QDST pulse shaper proposed by our group. Comparatively less attention has been paid to the use of SLMs for the generation of user-defined spatial light patterns specifically designed for ultrashort sources. However, spatial shaping of femtosecond lasers into any user-defined diffractive pattern is an issue of great interest. The possibility of generating light structures with micrometer precision results in a significant reduction of time considering material processing [141, 142]. Complex light patterns are implemented at one shot, and thanks to the programmable nature of SLMs, they vary in time up to a millisecond rate. A similar benefit involves the use of beam shaping techniques in nonlinear microscopy [23, 143, 144]. It allows for the design of scanless setups with simultaneous imaging of large areas. This is of particular interest in neuroscience, where the activity of large neural circuits must be mapped at the same time under femtosecond illumination [22]. For instance, they can be used for simultaneously photo-manipulation of living samples in a variable and temporally dynamic manner and/or for the stimulation or inhibition of multiple neurons at once to achieve specific excitatory/inhibition effects.

DOEs offer great versatility to generate almost any desired light pattern, and they are usually the choice for spatial shaping. Moreover, CGHs encoded in a SLM enables dynamic codification. They offer clearly more flexibility and customizability than imprinted fixed elements. In this sense, several algorithms have been developed, such as Gercherg-Saxton [145], to determine the phase which needs to be encoded in the SLM to have a certain light distribution at a given point. This process is known as phase retrieval, and it is unambiguously defined for a specific wavelength, which is the case of monochromatic (or quasi-monochromatic) light sources. In these cases, decomposition of the electric field according to its spatial and temporal dependence is possible: $E(x, y, z, t) = E(t)E(x, y, z)$. It is assumed that the modifications in the spatial profile of the beam do not affect its temporal profile.

For the case of ultrashort lasers, which have a large spectral bandwidth, the previous decomposition of the electric field is not possible. When the pulse propagation through an optical system is wavelength dependent, each wavelength component of the pulse may experience a different spatial propagation. As previously commented, it leads not only to distorted spatial patterns, but also to a spatial dependence of the pulse duration. The spatiotemporal distortions may introduce an inherent drop of the peak intensity inhomogeneously distributed over the generated diffractive pattern. Thus, when dealing with ultrashort illumination, it is mandatory to characterize the spatiotemporal dynamics of the beam at the output of the optical system in order to properly understand the beam behaviour for further applications.

5.1 FEMTOSECOND GENERATION OF A FLAT-TOP BEAM

In this section we perform an experimental characterization of the spatiotemporal behaviour of an ultrashort pulse after passing through a Gaussian to flat-top beam (FTB) diffractive converter. We aim to introduce a proof of concept experiment to test the chromatic artifacts introduced by a commercial DOE under femtosecond illumination. The election of a flat-top converter DOE is not arbitrary. The use of FTBs instead of Gaussian beams may be advantageous in some applications involving ultrashort lasers. Experiments in high-field physics have benefited from FTBs, where they have been demonstrated to lead to more efficient proton acceleration [146]. In atto-science, FTBs have been employed to generate isolated attosecond pulses and controlled high-order harmonics, reaching broadband extreme UV beams with extremely low divergence [37, 42].

When the optical system includes DOEs, the response depends on the wavelength and therefore knowing the pulse dynamics in its spatial and temporal coordinates is critical. This is especially important when the resulting beam is used in a second stage where the spatiotemporal profile of the pulse is an important parameter. For this purpose, we carried out the complete spatiotemporal dynamics and propagation of femtosecond FTBs. In this way, 30-fs input pulses were shaped by a Gaussian to FTB converter DOE and characterized by means of the STARFISH technique [17], which is explained below. As a DOE, we used a commercial flat-top shaper (TH-033, HOLO/OR). This shaper does not need a Fourier lens, since the diffractive pattern is integrated on a refractive lens. It is designed to operate at λ=800 nm and a working distance WD of 200 mm, for a 6 mm input Gaussian beam diameter (D_{in}). The final size of the flat-top pattern is around 3 mm (D_{out}). In Fig. 5.1 it is shown a schematic of the diffractive device.

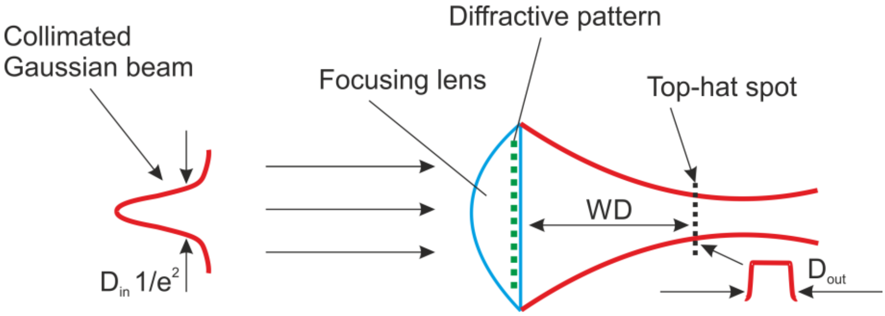

Figure 5.1. Schematic of the Gaussian to FTB converter. The DOE is inserted inside a focusing lens.

The diffractive flat-top beam shaper is a phase element that transforms the Gaussian input beam into a uniform spot with sharp edges at a specific working distance WD. It is important to note that the flat-top spot is not at the minimum spot location (minimum waist), but near it.

The experimental setup for the spatiotemporal characterization of the beam is shown in Fig. 5.2. In this case we used a different laser than in previous experiments. This laser corresponds to the amplifier output of the

HE Pro CEP laser (see annex). It delivers pulses centred at 800 nm of around 23 fs duration, with 1 kHz repetition rate and energy up to several mJ. A spatial filter allowed us to obtain a fairly good Gaussian beam profile. This is achieved with two lenses, L_1 and L_2, of focal lengths f_1=250 mm and f_2=300 mm respectively. It allows us to obtain a 6 mm (D_{in}) Gaussian beam at the input of the DOE as it is required by the design specifications. The wavefront sensor (WFS) is placed in order to check the collimation of the resulting beam before the flat-top DOE.

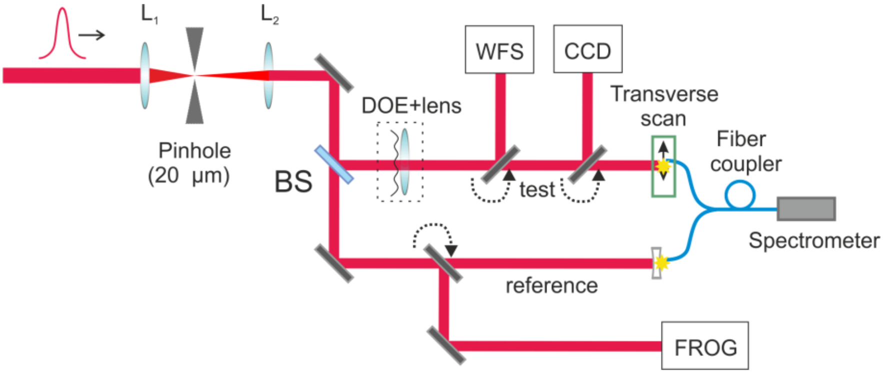

Figure 5.2 Experimental setup for the spatiotemporal characterization of the DOE. The beam splitter (BS) divides the beam into the reference and test lines. The dotted curved arrows in some mirrors means that they are flip mirrors. These mirrors are used to deviate the beam to the wavefront sensor (WFS), the CCD camera and the FROG measure system.

The measurement of the spatiotemporal light distribution at the flat-top beam plane was performed by using the STARFISH technique [19]. This reconstruction technique consists of spatially resolved spectral interferometry using a fiber optic coupler as interferometer. Here, the light from the ultrafast laser source is split in two arms: the reference and the test beam. The reference and the test beam are collected into the fiber input ports. The test arm spatially scans the transverse profile at the output plane of the DOE and the reference arm controls the relative delay between the pulses required for the interferometry (around 2 ps in the experimental conditions of the present study). For each transverse position, both pulses are combined inside the fiber coupler and leave it through the output common port that is directly connected to a standard spectrometer where the interference spectrum is measured (resolution 0.1 nm, AvaSpec-2048, Avantes). The reference beam is not scanned and its spectral phase is obtained on-axis just by means of a conventional frequency-resolved optical gating measurement (FROG). From the spectral interference, the spectral phase and amplitude at each point are obtained by data processing using conventional algorithms. Finally the temporal profile is recovered by Fourier transformation.

In Fig. 5.3 we show a set of measured results corresponding to the plane which is 200 mm away from the DOE. In the part a) of the figure the recorded spatio-spectral phase for the test beam is shown in logarithmic scale. From this representation it is clear that the DOE response is wavelength dependent. Lower wavelengths are less spatially dispersed than higher ones.

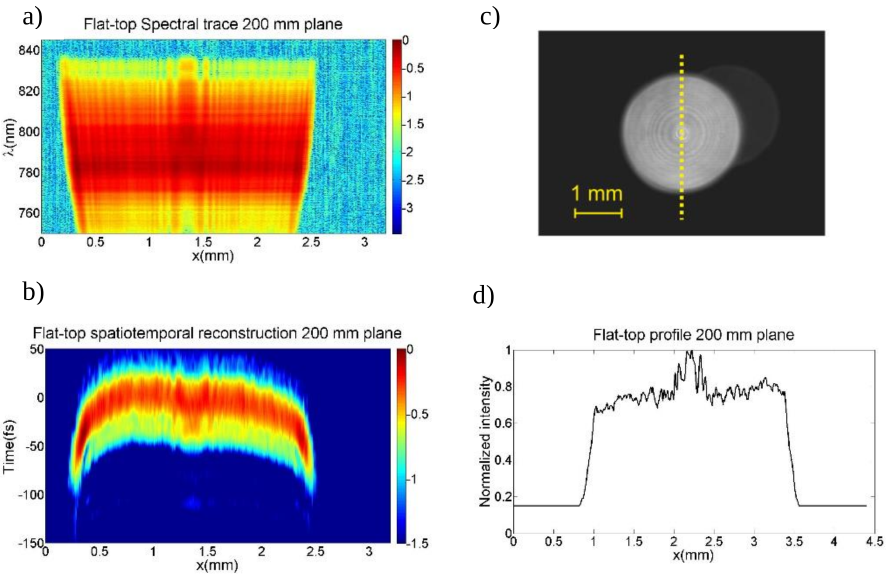

Figure 5.3 Experimental analysis of flat-top beam generation.

In the part b) of Fig. 5.3 the spatiotemporal reconstructed trace is represented also in a logarithmic scale. At a first view, a curved structure is observed. This implies that light from the outer part of the pattern is delayed approximately in 50 fs with respect to the central part of the beam. In the part c), we show the spatial pattern of the flat-top beam. In the part d) we plot the profile of the spatial part of the beam that corresponds to the vertical dotted line of part c).

From the analysis of Fig. 5.3, we can extract several conclusions. First, it is clear that each individual wavelength of the pulse experiences a slightly different propagation after passing through the flat-top DOE. It affects the spatial profile at the output plane, which is narrower for shorter wavelengths (Fig. 5.3a). Second, from the analysis of Fig. 5.3b we can assume that the temporal width of the pulse is homogeneous for almost the whole spatial profile, but present some inhomogeneities and a delay in the wings. It supposes an evidence of temporal distortions, since the spatiotemporal profile of the beam is not completely uniform. The last conclusion is related to the particular operation principle of the considered DOE. As we have stated in the first two conclusions, the effect of chromatic artefacts are appreciable both in space and time. However, it is clear that they do not introduce strong distortions that completely destroy the dynamics of the beam. The main reason is that only low spatial frequencies are involved in this experiment. The flat-top converter generates a circle of light symmetrically distributed along the propagation axis, as it is appreciated in Fig 5.3c. In fact, in the intensity profile of Fig. 5.3d, a peak of light is observed in the middle of the light distribution that can be interpreted as a “zero non-diffracted order”. Therefore, the lack of high spatial frequencies result in the presence of small spatiotemporal distortions. This conclusion is fully developed in the next section of this chapter.

The characterization carried out by the STARFISH technique must be taken into account for forward applications where this DOE is used with ultrashort illumination, as for example, to assess the validity of flat-top shapers for femtosecond laser processing. Although the distortions appear to be low, it is necessary a careful consideration about how critical are for each particular application. The characteristics of the pulse and the type of DOE influence the final response of the optical system. As we will see in the next section, the use of ultrashort pulses and DOEs is not necessary translated into high spatiotemporal distortions. However, when high spatial frequencies and very short pulses are involved, these distortions become significant and may need active correction for further applications.

5.2 FEMTOSECOND PULSES AND HIGH SPATIAL FREQUENCIES

For ultrashort pulses the irradiance patterns generated with SLMs involving high spatial frequencies appear naturally blurred [147]. This effect is very easily understood by looking at Fig. 5.4, where a very simple example of the dispersion associated to DOEs (a diffraction grating in this case) under broadband spectra illumination is shown. A pulsed laser passes through a diffraction grating of period p_0 that separates the beam into several diffraction orders. Then, the diffraction pattern is focused by an achromatic lens (L_1) of focal length f_0.

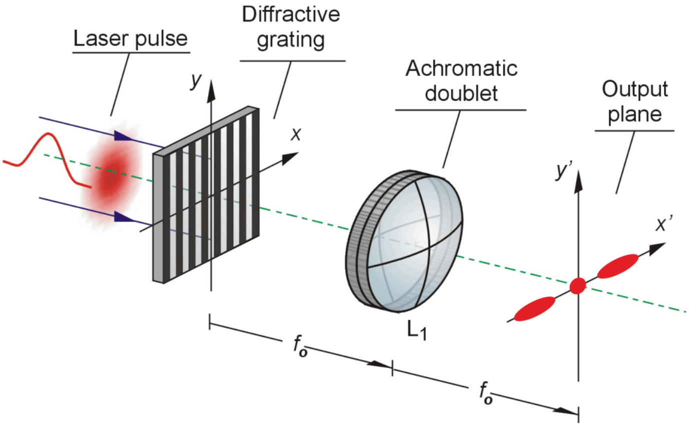

Figure 5.4 Multifoci generation by means of a diffraction grating and an achromatic lens. The wavelength dependence of the angular dispersion associated to this system generates elongated light spots for the nonzero orders.

At the focal plane of the lens, the diffraction pattern for the non-zero orders appear naturally elongated. Apart from possible distortion effects due to wavefront aberrations or light dispersion, this usually unwanted physical phenomenon is mainly attributed to the linear dependence of the scale of the Fraunhofer irradiance patterns with the wavelength of light, usually known as spatial chirp. The angular dispersion of the grating is different for each spectral component, and thus the finite bandwidth of the laser source results in an increase of the eccentricity of the focused spots. Simultaneously, a temporal stretching of the pulses is also reported [148] due to the PTD between pulses coming from different parts of the grating. This time stretching principle is the same than that illustrated in Fig. 4.3 to show how works our proposed QDST pulse shaper. It cannot be precompensated with the chirping of the original pulse as group-velocity dispersion broadening.

In mathematical terms, the temporal and spatial stretching associated to the above example can be demonstrated as follows. Considering a one-dimensional model for the scalar electric field $E(x,t)$ we can write the input electric field to the diffraction grating of Fig. 5.4 as:

$$E(x,t) = E_0 \exp(-x^2/4\sigma_x^2) \exp(-t^2/4\sigma_t^2), \tag{5.1}$$

where σ_x and σ_t correspond to the root mean square (rms) width of the spatial and temporal irradiance profiles, respectively. In Eq. (5.1), the input pulse is split into its spatial and temporal components. This description is only correct to define the input beam before the optical system. After passing through the optical system, the spatiotemporal coupling has been taken into account and it is no longer possible to consider the temporal and spatial parts as if they were independent. In the spectral domain, the pulse is defined by the carrier frequency w_0 and the rms width of the power spectrum $\sigma_w = 1/(2\sigma_t)$.

For the configuration of Fig. 5.4, σ_x' and σ_t' represent the rms width of the spatial and temporal irradiance profiles at the output plane, which is different depending on the n th-order diffraction maximum. The relative temporal and spatial stretching are calculated as σ_t'/σ_t and σ_x'/σ_0. The value σ_0 is the spatial rms width of the zero diffraction order for the carrier frequency w_0. Thus, the relative spatial and temporal broadening, with respect to the unaffected zero diffraction order, can be estimated by the expression [55]:

$$\frac{\sigma_t'}{\sigma_t} = \frac{\sigma_x'}{\sigma_0} = \sqrt{1 + \left(\frac{4n^2\pi^2\sigma_x^2}{p_0^2 w_0^2 \sigma_t^2}\right)}. \tag{5.2}$$

To have a more intuitive idea of this fact, in Fig 5.5 we perform a plot of the relative stretching versus the input pulse width for the first-order diffraction maximum and four different grating periods: 5lp/mm, 20 lp/mm, 100 lp/mm and 250 lp/mm. The period in milimeters is calculated dividing 1 mm by the number of line pairs per milimiter (lp/mm). For the calculation we have used values which are consistent with the use of our amplifier FemtoPower compact Pro laser output (λ_0= 800 nm) and our SLM. In this way, we substitute in Eq. (5.2) n=1, σ_x= 2.16 mm, w_0= 2πc/λ_0 and values for σ_x ranging from a few femtosecond to several tens of femtosecond. Note that in Fig. 5.5 the values for the temporal pulse width are displayed at intensity FWHM, which is equal to $2\sqrt{2ln2}\sigma_t$.

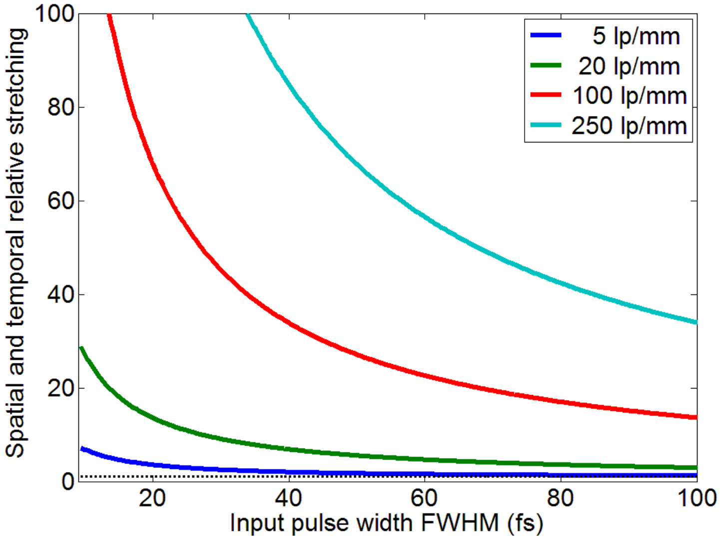

Figure 5.5 Relative stretching versus the input pulse width FWHM for the first-order diffraction maximum and different grating periods. Dotted black line equals to one, representing no relative stretching.

From the previous figure, it is important to note that the effects of chromatic dispersion depend not only on the pulse parameters, but also in the optical response of the system. It is clear that, in general, the significant bandwidth of ultrashort pulses results in a coupling of the spatiotemporal effects causing the degradation of the output image and the stretching of the pulse duration. However, for low spatial frequencies, as it is the case of the flat-top converter of previous section, the degradation effects may be moderate. The spatiotemporal distortions are greater for higher diffraction orders, resulting in an inherent drop of the peak intensity inhomogeneously distributed over the output plane of the system. Similar effects are expected to happen when the diffraction grating is replaced by a CGH encoded in a SLM. When high spatial frequencies are involved, the diffraction pattern will appear blurred and temporally stretched.

The distortions calculated before are very relevant when the laser interacts with nonlinear media in a second stage. As shown in Eq. (2.2) the nonlinear response of the medium depends on the 2th, 3th or higher power of the field amplitude, making the intensity drops due to the spatiotemporal distortions more evident. In particular, for TPA fluorescence signal generation, it is important to keep the pulse as short as possible to increase the fluorescence signal as suggested in Eq. (2.25). Thus, dispersion compensation techniques are required to minimize these effects at the target [56, 148].

5.3 DISPERSION COMPENSATION MODULE

Different solutions have been proposed to overcome the distortions associated to the use of DOEs and ultrashort laser sources. Several efforts were conducted in the past few years to compensate for the angular dispersion in DOE-based systems working with femtosecond light beams, with the temporal stretching remaining uncorrected. In the paper by Amako et al. [149], the femtosecond beam is split by means of a diffraction grating and the lateral walk-off among the different spectral components of diffraction maxima is corrected by focusing the pulsed light with a DL. The focal length of a DL is proportional to the wave number of the incoming radiation, which is the key point to attain dispersion compensation. The pulse is temporally stretched at the focal plane, which leads to a considerable reduction of the laser peak power in the output plane. A system consisting of a Dammann grating and a subsequent m-time-density grating, arranged in a conventional double grating mounting, has been proposed to reduce the angular dispersion associated with the mth-order beam generated by the Dammann element [150]. Here, pulse broadening due to diffraction is not as large as that produced by the grating pair used in other techniques because of the low period of the Dammann grating, 10 lines/mm. Kuroiwa et al. have shown that the large chromatic dispersion effects induced by DOEs can be reduced when the focalization of the pulse is achieved with a refractive lens, instead of being included in the CGHs design [151]. In the field of micromachining, Jesacher et al. have proposed a way to fabricate 3D structures with high spatial quality by doing machining at different depths of a crystal, but close to the optical axis to avoid chromatic aberrations [152]. Very recently, Hasegawa et al. [153] proposed a method for spatial wavelength dispersion control that uses a pair of SLMs. One is employed to encode a Fourier hologram that creates an arbitrary bidimensional intensity pattern. The other introduces an angular dispersion to the beam that allows us to obtain diffracted limited spots at the output of the system.

Of particular interest is the hybrid diffractive-refractive lens triplet DCM proposed in reference [55], which is formed by one refractive lens and two diffractive lenses (see Fig. 5.6). This proposal allows for first order compensation of both spatial and temporal dispersion associated to DOEs **[IX]**. A full mathematical description based on the spatiotemporal nature of the wave equation can be found in reference [154]. The DCM compensate only for first-order dispersion, while higher order as GDD or TOD remain uncompensated.

In practical terms, the imposed conditions for dispersion compensation are translated into three geometrical constraints between the components of the DCM triplet. Therefore, they must fulfil that: $l = f_0$, $d^2 = -f_{0,1}f_{0,2}$, and $d' = -d^2/(d + 2f_{0,1})$, where l is the distance between L_1 and DL_2, and d the distance between DL_1 and DL_2. Only a real plane is obtained when DL1 and DL2 are diverging and converging, respectively.

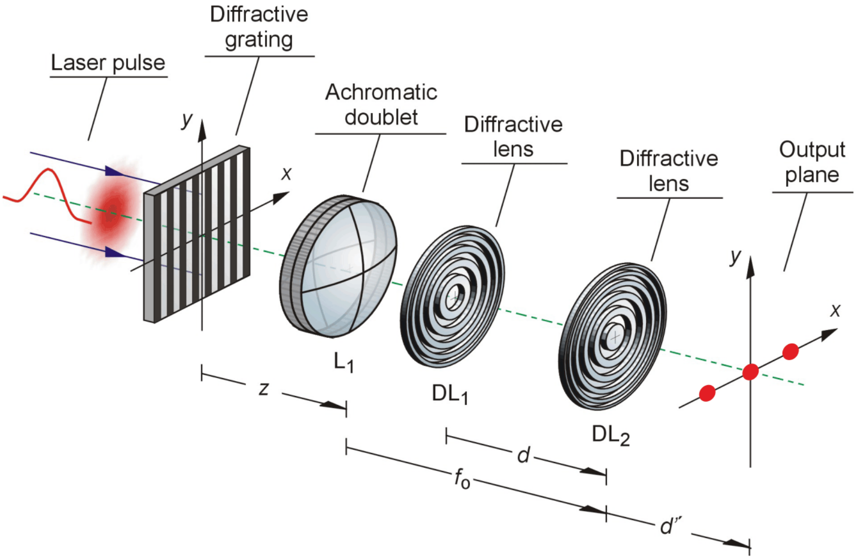

Figure 5.6 Multifoci generation sketch with the DCM. Spatiotemporal distortions are compensated by a triplet composed by one achromatic lens of focal length f_0 *and two diffractive lenses DL1 and DL2 of focal lengths* $f_{0,1}$ *and* $f_{0,2}$*, respectively*

In figure 5.7, extracted from reference [148], it is shown an example of the potential of DCM for spatiotemporal dispersion compensation. For this experiment the configuration setup was the same than Fig. 5.4 for the non-compensated system and same than Fig 5.6 for the compensated system.

The diffraction grating used for the experimental results shown in Fig. 5.7 results had a fundamental frequency of 11.8 lp/mm, with $f = 200\,mm$ and $f_{0,1} = -f_{0,2} = -150\,mm$. The temporal width of the pulses was 28 fs amplitude FWHM and the central wavelength of the corresponding spectra $\lambda_0 = 800\,nm$. Spatiotemporal reconstruction at the output plane was performed by the STARFISH technique [10]. Light distributions for the 0, +1, +2 and +3 diffraction orders are shown. For the zero order there are no differences (as expected) between the compensated and non-compensated configurations. However, for non-zero orders the spatiotemporal spreading of the beam is far from being negligible and it is relatively well compensated by the DCM.

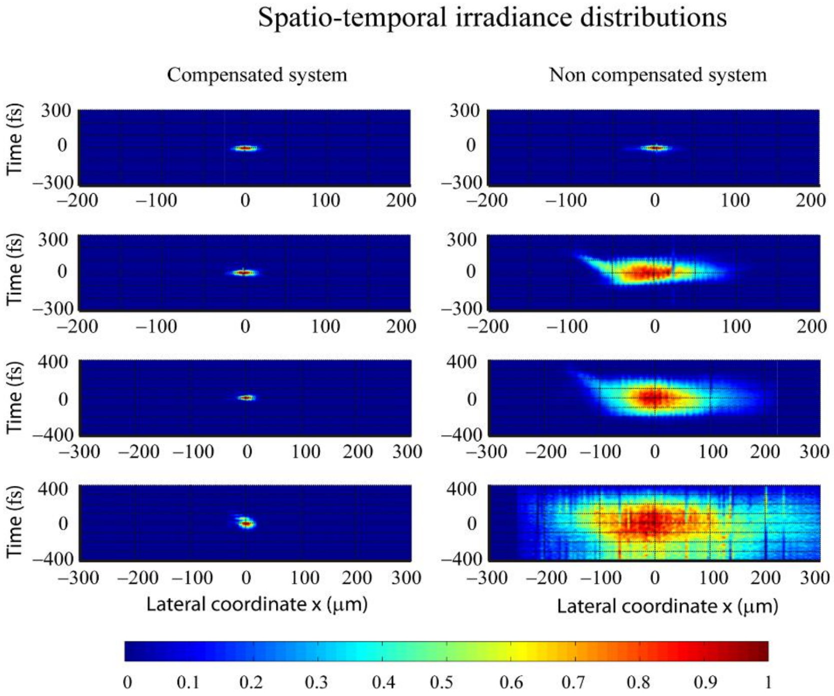

Figure 5.7 Normalized spatiotemporal light intensities for the 0, +1, +2 and +3 diffraction orders coming from the diffraction grating and focused by an achromatic lens. In the left column the compensated measurements taken with the DCM are shown and compared to those without DCM (right column).

5.4 APPLICATION FOR SCANLESS TWO-PHOTON MICROSCOPY

Time resolution is one of the most limiting factors in scanning two-photon imaging. In practical terms, the dwell time –the illumination time required per pixel to yield an image with a high enough signal-to-noise ratio for subsequent analysis- limits the acquisition of a full frame to a time period that is usually hundreds of millisecond or longer. On the other hand, current high-gain femtosecond amplifiers running at kilohertz repetition rate usually supplies pulse energies (of several milijoules) that exceed by far the amount of energy needed in most of the applications where they are used. In particular, for nonlinear microscopy, 90-95% of the light is discarded. Therefore, some experiments have been performed in the fields of multiphoton microscopy to improve the temporal resolution by splitting the excitation beam into multiple beamlets by means of DOEs encoded onto a SLM. In this way, the incoming laser beam is shaped into a user-defined light pattern [23, 143] making possible a scanless two-photon microscopy. However, as previously commented, splitting a short pulse by means of a DOE is problematic because of wavelength dependence of the diffraction phenomenon. Light patterns in the sample appear naturally blurred, thus reducing image resolution, and temporally stretched, which dramatically influences the efficiency of the TPA process. To get an idea, the two-photon signal intensity is reduced to 0.5% of the available signal for a spatial frequency of 30 lp/mm encoded onto the DOE [148], due to spatial and temporal stretching of the pulsed beam at the sample plane.

Taking all this into account, we have proposed a proof of concept optical system for efficient generation of wide-field fluorescence signals in two-photon microscopy, reducing spatiotemporal distortions associated with the use of ultrashort light sources and DOEs **[III]**. The main idea is to encode properly designed CGHs onto a SLM in order to generate user-defined extensive light patterns in two dimensions. To counteract spatiotemporal distortions, we propose the use of the DCM, which is inserted between the SLM and the sample. It supposes a dispersion first-order correction, obtaining a two-photon fluorescence signal with higher spatial resolution and improved efficiency compared to the case without DCM.

Our experimental setup is shown in Fig. 5.8. The amplifier output of our FemtoPower compact Pro laser is used as pulsed source. The pulsed laser beam impinges by means of a beam splitter onto a Fourier CGH encoded onto a phase-only SLM. The CGHs are calculated by using the well-known Gerchberg–Saxton IFTA, but carried out in two stages as proposed by Wyrowski [43]. The dashed box in Fig. 5.8 is the DCM. As it was introduced before, it is made up of an achromatic lens L_1 (focal length f_1=300mm) coupled to a diffractive lens pair, DL_1 and DL_2. The focal lengths of DL_1 and DL_2, for the central wavelength of the laser are $f_{0,1} = -f_{0,2} = -150\,mm$. After the DCM, in order to properly excite the fluorescence signal in Rhodamine B (RB), we use a telescope with a refractive lens L_2 (focal length f_2=100mm) and a 20x microscope objective MO_1 with focal distance 10 mm. To observe the fluorescence signal, the RB plane is imaged onto a conventional CCD sensor by means of a 50x microscope objective MO_2. We place a suited filter F before the CCD camera to prevent from propagation of the infrared signal.

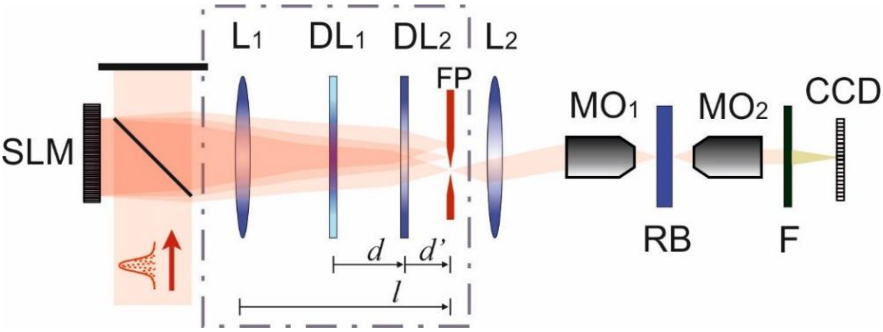

Figure 5.8 Schematic of the diffractive-refractive optical system used to improve TPA and fluorescence emission in RB.

Proof of concept is provided by sending different light patterns to the RB sample. In this sense, several CGHs are generated to create user-defined laser profiles. Bike, spiral and a 5x5 matrix shapes are generated, and their computer reconstructions shown in Figs. 5.9a, 5.9d and 5.9g. The spatial spectrum of the samples ranges from frequencies of around 25 lp/mm to about 38 lp/mm. Within this interval, the effects of theoretical spatial and temporal broadening enlarge foci by a factor of 25 to 40 times in both spatial and temporal domains with respect to that of the unaffected zero diffraction order (SLM acting as a mirror).

In a first configuration, the DCM is removed from the setup and the fluorescence signal recorded. This is shown in Figs. 5.9b, 5.9e and 5.9h. As expected, the fluorescence pattern is blurred due to the spatial spreading of each frequency contained in the finite spectrum of the femtosecond pulse.

Moreover, in order to detect significant signal from the RB, average beam power is set to 5 mW. Temporal stretching causes a loss of fluorescence signal. From Eq. (2.25) it is clear that the number of emitted photons at the sample depends inversely on the pulse width.

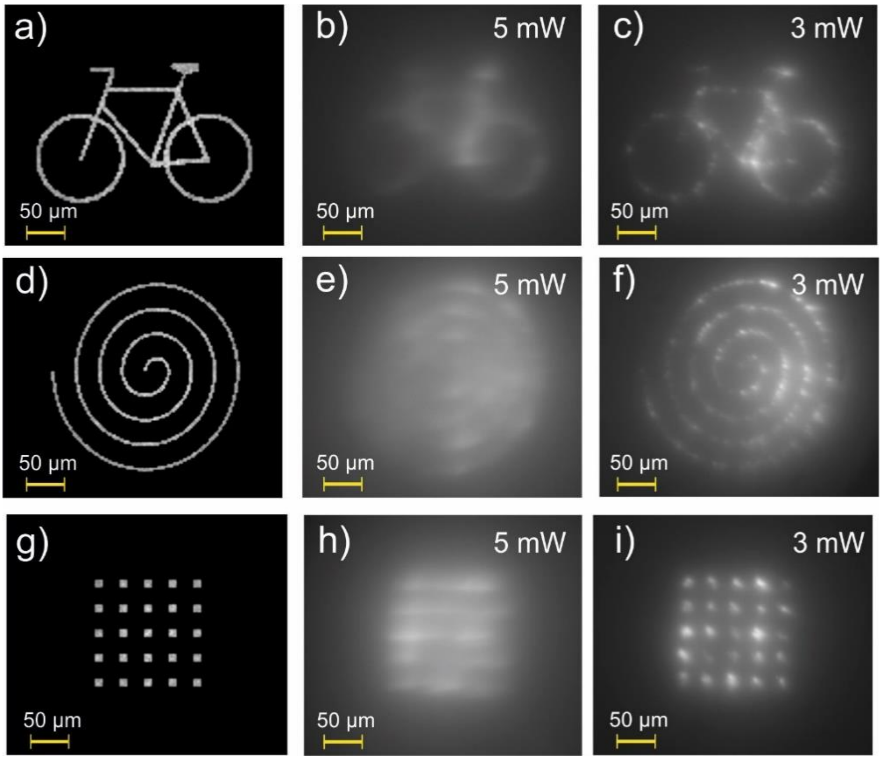

Figure 5.9 Light patterns used for TPA in RB. Left column (a, d and g) corresponds to computer reconstructions of the encoded holograms. In the central column (b, e and h), the recorded light pattern without DCM are shown. Right column (c, f and i) corresponds to the improved fluorescence signal recorded when DCM is implement in the optical system.

In a second configuration, the DCM is placed and fluorescence signal recorded again as shown in Figs. 5.9c, 5.9f and 5.9i. As done in the previous configuration, in order to ensure wide-field fluorescence signaling all over the sample plane for the repetition rate and the pulse width of our laser system the average power has to be adjusted to 3mW. The dispersion compensation abilities of the DCM preserve the spatial and temporal width of the laser pulse at the sample plane, and consequently the fluorescence signal is obtained for a 40% less energy than in the previous case. The transverse spatial resolution for the CGH reconstruction is maintained due to the spatial chirp compensation capacity of the module, and so the blurring distortion is eliminated in a big degree.

In summary, this method evidences a great correction of both angular and temporal dispersion, which in practical terms means that it applicability can be relevant in techniques such as nonlinear microscopy or material machining with high bandwidth lasers.

Chapter 6. Triggering nonlinear processes

In chapter 2 we established mathematically the differences between linear optics and nonlinear optics. The nonlinear phenomena are the result of an interaction between an intense electric field and matter. In practice, the laser is the only source able to produce sufficiently high optical fields to induce appreciable nonlinear response of materials [155]. The generation of new ultrashort and ultraintense laser sources are the gateway to new regimes in physics, as it is the case of the “ultrarelativistic systems”, where electrons and ions move close to the speed of light accelerated by a pulsed laser [156]. In this sense, extreme light applications are nowadays considered as disruptive technologies able to broaden the frontiers of physics during the next decades, and also enabling new technological devices for real-world applications.

The wavelength of the pulsed laser is determined by the amplification crystal’s band structure, which in the case of Ti:sapphire crystal is centred around 800 nm, so the wavelength tunability is limited to a certain range around that wavelength (650-1100 nm). On the other hand, one of the most spectacular phenomena of nonlinear optics is the generation of new wavelengths. Barely a year after the invention of the laser, Franken et al. obtained experimental evidences of SH generation from a ruby laser using a quartz crystal [79]. Nowadays, wavelength conversion processes are widespread as a source for generation of pulsed lasers [8]. This is the case of optical parametric amplification (OPA) [157], a technique that allows generating broad frequency tunable lasers by controlling the frequency of the signal coming from a nonlinear crystal. Many applications require laser pulses centred at other wavelengths in the visible, UV, or mid-IR regions of the spectrum. Most experiments of ultrafast spectroscopy require pulses at differing wavelengths dictated by the absorption features of the sample [158]. On the other hand, biological tissues absorb in visible-

UV range and proteins in the deep UV. Therefore, the generation of broadband spectrum sources with frequency tunability is of great interest.

In nonlinear optics, filamentation is an attractive phenomena as it is capable of generating light pulses of large spectral width. Filamentation of near infrared femtosecond pulses can eventually give rise to an extreme spectral broadening, ranging from the ultraviolet to the infrared regions, termed SC generation. The basic phenomena involved in filamentation and SC generation were explained in chapter 2. In this way, filamentation, together with hollow core fiber, is nowadays one of the most widespread techniques to achieve spectral broadening (white light generation) [60]. Therefore, filamentation constitutes a valuable phenomenon for the generation of very short pulses by properly compressing the SC signal. Apart from this, filamentation has also been exploited for other purposes such as remote atmospheric diagnostics [159], lighting protection [160], laser induced breakdown spectroscopy (LIBS) [161] or medicine [29].

Unfortunately, having control over nonlinear processes is far from simple. In general, the nonlinear regime results in complex phenomena where the spatiotemporal dynamics of the pulse and its interaction with matter is not fully understood yet in many cases. References [60, 162] make a review of the main physical factors and experimental conditions that have been demonstrated to play a role in SC generation. To name a few, numerical aperture, polarization, pulse duration, input chirp, input wavelength and pulse energy are parameters to be considered for nonlinear generation. In this sense, the use of SLMs for triggering nonlinear processes have several advantages as they offer great flexibility and versatility. As we will see in the next sections, the strong chromatic aberration induced by DLs allows the shaping of the spectral properties of the pulses generated in SH generation [163] or in SC generation [73, 164]. Several DLs can be easily implemented at once onto the SLM, generating a diffractive microlens (DML) array. Hence, several beams independently controlled can be used for multifilamentation generation. The programmable nature of SLMs is of great interest to dynamically control some of the parameters (NA, focal length, focusing efficiency) involved in nonlinear processes. In addition, it has been shown that SLMs can compensate for aberrations carried out by the beam, as well as intensity inhomogeneities.

6.1 ON-AXIS NONLINEAR EFFECTS WITH DAMMANN LENSES

In this section, we use Dammann lenses implemented onto a SLM to trigger nonlinear effects **[IV]**. Specifically, we demonstrate the application of Dammann lenses to SH generation and filamentation in transparent dielectrics. Dammann diffraction gratings are binary phase distributions of alternative 0, π zones for well-defined transient points [36, 165]. These gratings generate far-field diffraction patterns characterized by a number N of diffraction orders all having the same intensity. This concept can be easily extended to lenses. The phase of a converging refractive lens for monochromatic radiation can be represented by $\pi r^2/\lambda f$, where r denotes the radial coordinate, f the focal length, and λ the wavelength of light. The lens function $exp(i\,\pi r^2/\lambda f)$ can be binarized by applying the Dammann grating formalism to the squared radial coordinate r^2 [41]. The resultant binary lens function will create a series of N focal planes having focal lengths of f/n with equal peak intensities, where $n = (\dots,-3,-1,1,3,\dots)$, for an even number of orders, and $n = (\dots,-2,-1,0,1,2,\dots)$ for an odd number of orders [166]. Dammann lenses are unambiguously defined for a particular λ, thus obtaining N on-axis focal spots of the same intensity when a CW is used as illumination source. However, for ultrashort pulsed illumination with temporal widths lower than 100 fs, the generated irradiance patterns are significantly affected by chromatic aberrations.

The experimental setup to test Dammann lenses for nonlinear processes is shown in Fig 6.1. For the experiment we used the amplified output of our laser system, and Dammann lenses were encoded onto the Holoeye Pluto SLM. The reflected beam from the SLM passes through a 1x telescope composed of a pair of lenses L_1 and L_2 of focal lengths f_1=f_2=100 mm. The telescope makes an image of the SLM plane after the lens L_2.

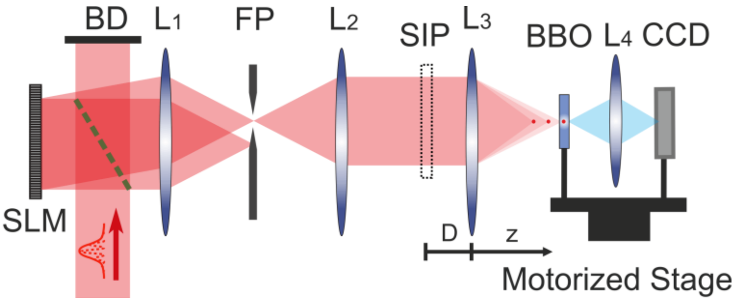

Figure 6.1 Experimental set-up. The input beam is split in two rays by a beam splitter (green dotted line) to work with the SLM at normal incidence. A beam dumper (BD) is used to block the unused part of the beam.

To avoid the zero diffraction order of the SLM, we overlap a linear phase of period 0.3 mm to the Dammann lens, and use in the experiment its first diffraction order. In addition, to ensure an equal spacing among all Dammann foci, a third lens L_3 is placed at the focal length distance F=D=50 mm from the SLM image plane (SIP). This configuration allows us to obtain a number N of equally spaced focused spots with the same peak irradiance. The focal planes ($z=f_n$ from L_3) of the foci can be determined by the expression

$$\frac{1}{f_n} = \frac{1}{F} - \frac{n}{(nD - f)} . \tag{6.1}$$

First of all we analyze the influence of broadband light spectra on the irradiance given by Dammann lenses under ultrashort pulsed illumination. The Huygens-Fresnel diffraction equation in the ABCD matrix formalism is used to simulate the irradiance I(z) along the propagation axis. Here, the on-axis irradiance obtained with a Dammann lens of five equal foci separated by 2.05 mm is shown. As it can be seen in the top part of Fig. 6.2, the simulation was carried out for two different Fourier transform limited Gaussian laser pulses, and an ideal CW source.

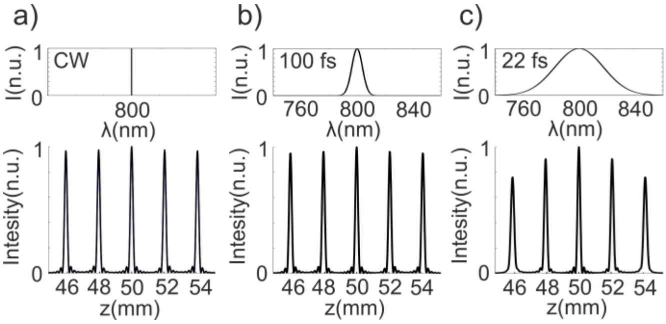

Figure 6.2 . Simulated irrandiance pattern obtained with a Dammann lens which is illuminated with (a) monochromatic beam, (b) 100 fs laser pulse, and (c) 22 fs laser pulse.

The theoretic irradiance uniformity in the case of the CW source is approximately 10^{-5} [167]. However, small discrepancies in the height of the peaks are caused mainly due to deviations of the 0-π transition locations from their ideal values when encoding Dammann lenses onto a SLM due to the pixelated nature of SLMs. For an ultrashort laser pulse of 100 fs falls of 0.3% and 1.5% (for n=±1 and n=±2 orders, respectively) are registered. The equivalent values for 22 fs pulses were 6% and 20%. Therefore, chromatic aberrations will increase the spatial width and decrease the peak irradiance of the foci, reducing the uniformity of the generated irradiance patterns.

In order to show the potential of Dammann lenses to generate non-linear effects, we developed a couple of experiments. First, we explored SH generation originated by a programmable set of on-axis Dammann foci. To do that, a type-I (BBO) crystal (θ=29.2º, 20 μm thickness) was displaced along the different foci generated with Dammann lenses in the focal region of L_3. With the help of the lens L_4, magnified images of each focus were formed onto a charge-coupled device camera (CCD). To avoid transmission of infrared light a suitable filter was placed in front of the CCD. The scanning device (made up of BBO crystal, lens L_4 and CCD) was mounted on a motorized stage which allows for computer controlled movements via Matlab code. The thickness of the nonlinear crystal ensures enough spectral acceptance for the SH generation of the fundamental pulses, which energy was carefully set to avoid the damage of the crystal during the scan.

In Fig. 6.3, experimental results are shown. Furthermore, images of the transversal focal spots, the spectrum of our laser and the encoded Dammann phase mask are provided as insets. This Dammann phase mask generates a set of N=4 foci separated by 1.92 mm. The motor step was set to 20 µm. The SH irradiance recorded with the CCD is plotted as a function of the distance z from the lens L_3, and represented by a red dotted line. Within the paraxial Fresnel approximation, the experimental results are compared to numerical simulations (black line) of the squared normalized irradiance I^2 (z) calculated for the measured spectrum of our laser. From a visual inspection of Fig. 6.3 it is apparent that experimental results are in good agreement with the simulations. We believe that almost inappreciable differences in the locations of the peak irradiances are mainly due to possible deviations of the pulsed laser beam (towards convergence behaviour) from its collimated state before the L_3 lens. In addition, the increase in the axial width of experimental data with respect to simulations is mainly attributed to the discrepancy of our beam from the plane wave illumination considered in simulations. Misalignment can also influence the broadening of the foci slightly.

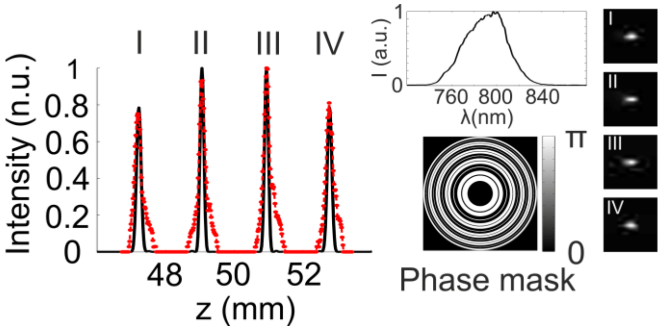

Figure 6.3. On-axis multifocal SH generation with Dammann lenses: experiment (red dotted line) and theory (black line). Dammann phase mask, pulse spectrum, and images of the foci from a lateral side of the nonlinear crystal are shown as insets.

In a second set of experiments, the stage was removed and a fused silica sample (20x10x5 mm3, all faces polished) was placed along the multifocal axial distribution. The number and separation of the focal spots can be controlled through the parameters of the Dammann lenses. The plasma emission of the filaments was registered in a CCD from one of the sides of the sample. Fig. 6.4a and 6.4b correspond to four filaments with separations of 2.1 mm and 0.4 mm, respectively. In Fig. 6.4c three filaments separated by 2.14 mm are generated, whereas in Fig. 6.4d the number of filaments is increased to six with a distance among them of 0.85 mm. As it might be expected both the shape and intensity of the filaments change with their distance from the air-glass interface due to the spherical aberration induced by light refraction [72, 168].

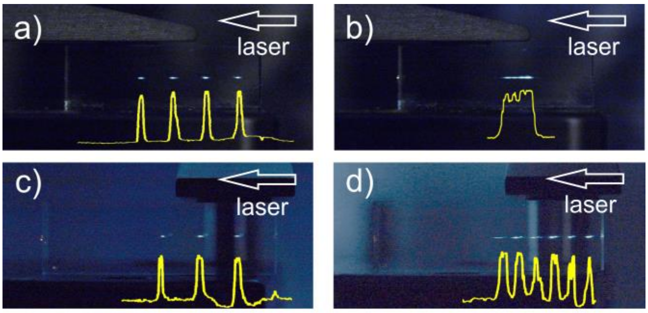

Figure 6.4. Examples of multifilament generation in fused silica glass. The number of filaments and distances between them are changed by encoding different Dammann lenses.

Keeping unchanged the experiment configuration, we measured the supercontinuum spectra generated by 4 foci with different separations, going from 0.2 mm to 2.5 mm. They were measured at the rear face of the supercontinuum sample. The spectrum ranges go from 450 nm to 1000 nm and are plotted in Fig. 6.5.

Finally, it is important to note that the efficiency of this experiment is mainly affected by three factors: 1) the SLM, attending the device efficiency and losses due to the electronic nature of SLMs, 2) the inherent Dammann lens efficiency and 3) the droop of the efficiency caused by the limitations in the integration of the Dammann lenses in a SLM due to the limited pixel size. The SLM used for this experiment shows a reflectivity of approximately 60% and diffraction efficiencies of more than 80%. Thereby a total light efficiency of more than 50% per addressable diffractive device is possible. Dammann diffraction lenses efficiency depends on the number of foci. However, a usual value for this efficiency it is 80% [36]. Finally, the last factor affecting efficiency it is the deviation of the 0-π transitions point's locations. Due to the pixelated nature of the SLM, the position of these transition points will slightly differ from its ideal position. As a consequence, part of the light will not be properly diffracted, affecting the uniformity and efficiency of the generated pattern. Although this effect might be minimized [169], it reduces to an extra 90% the system efficiency. We have obtained this result by theoretical simulations of different Dammann lenses, comparing those whose transient points where well defined, to those whose transient points where poorly defined. Taking all these factors into account the total estimated efficiency should be around 40%.

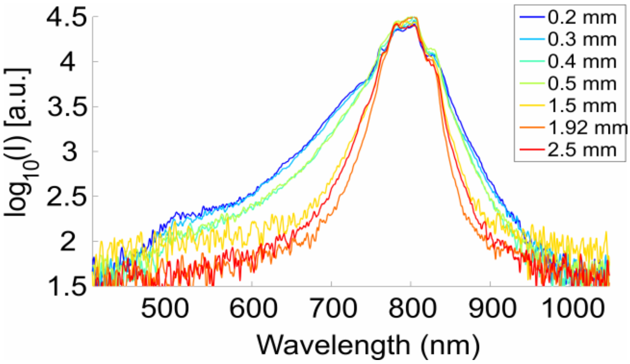

Figure 6.5 Spectral measurements for different separation among foci.

In summary, by using a phase-only SLM programmable, on-axis multiple MFs have been generated in a fused silica glass with femtosecond laser pulses. By changing the Dammann lenses parameters, we a complete control over the position, width and peak intensity of the MFs is achieved. Several applications are expected to benefit for these results, such as in-depth parallel processing of transparent dielectrics or the creation of long filaments by the concatenation of shorter ones.

6.2 CONTROLLED MULTIFILAMENTATION

In this section we focus on the deterministic generation of multifilamentation processes by means of SLMs **[V]**. The conditions for the generation of filaments and multifilaments with ultrashort laser pulses were briefly commented in chapter 2. We can distinguish two regimes: when the laser power is slightly above the critical power P_{cr} for self-focusing and when the laser power is much higher than P_{cr}. For the first case a single filament develops. For the second, modulation instability can cause a random distribution of co-propagating filaments formed from a single laser beam spontaneously. Understanding the interaction between these filaments and gaining control over their distribution is vital for the realization of any practical application [170]. To avoid the random space–time localization of MFs, the initial beam is modified by methods that include, among others, amplitude modulation by a periodic mesh [171] or nonlinear interaction of two overlapping beams [172]. However, the controlled generation of multifilaments is still a challenge that must face many practical limitations. For example, when dealing with non-uniform or/and aberrated beams, the spatial dependence of the pulse characteristics makes indispensable a local and programmable control of the phase adaptable for each situation. Gaining control over the spatial filaments distribution is an important task in applications such as filamentation-based tumor treatment [29], a novel technique which has been recently proposed for cancer therapy. In such case, careful management of both the position and the energy of the filaments is decisive to control the radiological dose and avoid damage of the adjacent healthy tissue.

DOEs allow us to modify the spatial and temporal shape of the pulse and have already shown their potential in several applications. In reference [163] the efficiency of second-order nonlinear processes is increased by recording diffractive gratings in a birefringent crystal. SC generation based on diffraction effects is analyzed in [173], where Fresnel diffraction through circular apertures enhances SC generation by exploiting the lensing effect. More recently, the conjunction of femtosecond sources and DLs was exploited for the tunability of some nonlinear processes. The large spectrum associated to ultrashort sources, together with the strong dependence of diffraction on the wavelength, causes new observable facts. In this sense, wavelength tunability of second and third harmonic femtosecond pulses generated in nonlinear crystals [174] was achieved by changing the relative distance between the crystal and the DL, which acts in a focusing configuration. The same configuration has been used for SC generation where a strongly peaked structure appears in the blue region of the SC spectra. Moreover, the central wavelength of this peak can be easily controlled by simply changing the lens-crystal distance, a phenomenon that does not occur for achromatic refractive lenses placed in the same configuration [73, 164].

The experimental setup is shown in Fig. 6.6. The beam, which corresponds to the output of our FemtoPower compact Pro amplifier, is incident on the SLM. The phase encoded onto the SLM consisted of an array of 3x3 DMLs.

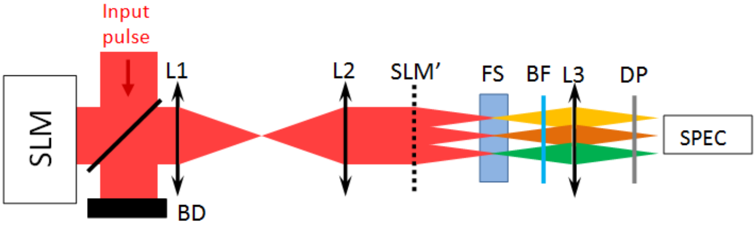

Figure 6.6. Experimental setup. The input pulse is divided at the 55:45 beam splitter (BD: beam dumper) and reaches the SLM. The pattern generated by the microlens array is focalized in the fused silica (FS) sample. The exiting light is filtered out with a band-pass filter (BF) and collected with a lens and a diffusing plate (DP) into a spectrometer.

The reflected beam from the SLM passed through the beam splitter, and then, a 1x telescope (L_1 and L_2) of focal lengths $f_1=f_2=100$ mm. The telescope is placed to be able to focus into the FS sample, as the focal length of the DML is smaller than the distance from the SLM to the rear part of the BS. The SLM screen is imaged at the focal plane of L_2 (labelled as SLM' in Fig. 6.6).

The focal length and the efficiency of each microlens is addressed by voltage following Eq. (3.3). The first is responsible for the tunability of the central wavelength of the SC, whereas the latter modifies the energy coupled to each filament. The encoded phase is for each microlens:

$$\Psi_j(r) = \alpha_j mod\left[\frac{kr^2}{2f_j}, 2\pi\right], \tag{6.2}$$

where j-index refers to each DML. The radial dependence has been removed from that of Eq. (3.3) since α_j is the same for the whole microlens. The efficiency is given by Eq. (3.4).

In a first set of experiments, we adjust the parameter α_j for each microlens. The parameters of the encoded microlens array were uniformly set to f_j= 60 mm and α_j=1 in the beginning. A fused silica sample (5x10x20 mm^3, all faces polished to optical grade) was placed in such a way that the multiple beams entered through the 5 mm long face and focused inside the sample (see Fig. 6.6). The pulse energy, controlled by a variable attenuator, was carefully adjusted just above the threshold to the produce SC with the central beam.

For a beam with spatial intensity inhomogeneties, the generated SC beams differ in intensity and spectral content. In Fig 6.7a the irradiance profile of our laser over the SLM is shown. Therefore, a different fraction of the incident energy will be delivered to the different DMLs (termed A, B….I in Fig. 6.7a). This problem can be overcome by means of the parameter α_j: if the diffraction efficiency is modified, the energy coupled to the foci can be equalized. Hence, filaments are formed at the same position inside the sample, yielding a similar spectrum.

To determine the value of each α_j, we measure the threshold for SC generation for each microlens. The threshold is defined as the minimum pulse energy required to just start SC generation (detected with the spectrometer). The measured values ranged from 30 µJ for the central microlens (E) to 160 µJ in the case of one of the external lenses. These values refer to the energy impinging the array of DMLs, not a single DML. In Fig. 6.7b we show the visible output signal projected on a screen for an input energy of 76 µJ with all the efficiency parameters set to α_j=1. As it can be seen in the figure, SC is produced only in the central and the four adjacent foci provided the energy delivered to the external lenses does not exceed the threshold. To equalize the energy coupled to each focus, we set the energy to 170 µJ, a bit above of the biggest SC threshold. Under this configuration, the energy delivered to all the foci was just above the SC threshold and a homogeneous visible signal was generated (see Fig. 6.7c).

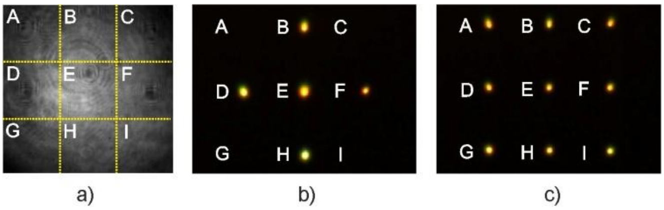

Figure 6.7. Beam profile at the SLM plane for 76 µJ input energy. The yellow lines denote the edges of the DLMs; b) SC signal for 76 µJ input energy and c) SC signal for 170 µJ input energy with efficiency correction as explained in the text.

Once the coupled energy to each focus is the same, we pursue control over the spectral properties of the so-generated beams. The position of the filament, and thus the spectral content of the SC generated signal, can be controlled by slightly modifying the focal length of the DMLs and keeping the pulse energy constant. To do that, the pulse energy was set to 200 µJ and the values of α_j were set to the computed values for foci homogeneization. Then, we set different focal lengths for each row of lenses (i.e. f_A=f_B=f_C=61 mm, f_D=f_E=f_F=56.3 mm and f_G=f_H=f_I=60 mm). As expected, the position of the filaments produced inside the silica sample is varies from one to other (see Fig. 6.8a), and so the spectra of the generated SC changes in agreement with our expectations, as it can be seen in Fig. 6.8b. Moreover, the DMLs with the longer focal lengths (A-C) forms short filaments, clipped by the rear face of the sample. This is associated with spectra tuned towards the shortest wavelengths, which is in accordance with the observations in [73]. In contrast, for the shortest focal lengths (D-F), filaments develops slightly behind the front face. Under these conditions, three colored patters were observed at the output of the sample (see Fig. 6.8c).

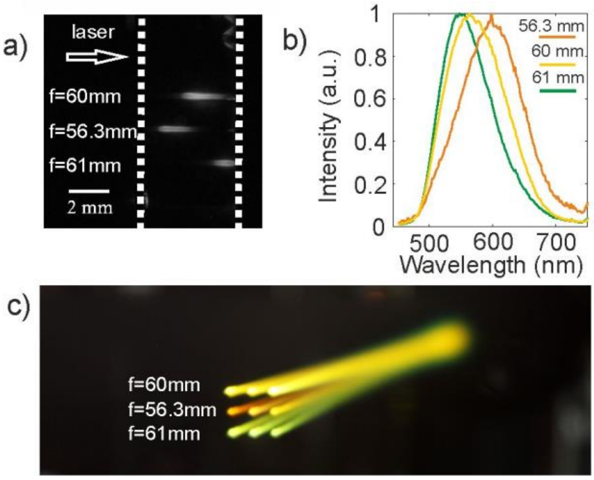

Figure 6.8. a) filaments' profiles inside the fused silica sample (the dotted lines indicate the sample's input and output faces); b) corresponding spectra measured behind the FGB37 filter and c) photograph of the generated SC light.

In summary, we have reported controlled MF in fused silica by encoding a DML array in a phase-only SLM. We have demonstrated a precise control on (i) the energy coupled to the filaments by means of the α parameter, and (ii) the spectrum of the generated SC light by changing the focal length of the DMLs.

6.3 CONTROLLING INTERFERENCE EFFECTS AMONG DIFFERENT FILAMENTS

So far, on-axis filamentation and spectral control of multifilaments have been shown by exploiting the potential of SLMs. In this section, we introduce the SLM as a suitable device not only to generate SC illumination, but also to study the interference properties of the generated SC light **[VII]**. As shown in previous section, local control over the optical phase enables us to gain fine control over the filaments. This also allows us to control the interference effects of the SC light coming from two (or more) geometrically close filaments, such as changing the visibility of the fringes in real-time. For this purpose, two microlenses are implemented onto the SLM, as it can be seen in Fig. 6.9.

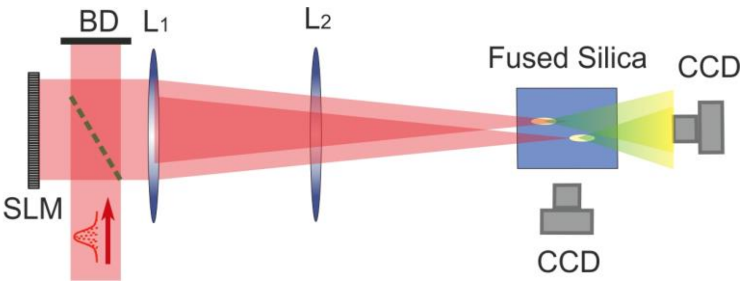

Figure 6.9. Experimental setup with the SLM. (BD: beam dumper; L_1 and L_2: refractive lenses)

Basically, the experimental conditions for measuring the interference effects of the SC generated by two adjacent filaments are the same than those from previous section. Only two important variations are introduced:

- Instead of the nine filaments shown in previous section, just two filaments are generated now. For this purpose, two adjacent DMLs of 1.44x1.44 mm^2 each one are encoded onto the SLM. The efficiency of each lens in controlled through the α_j parameter.
- In order to reduce the lateral separation of the foci, two opposite linear phases of the same period (80 μm) were overlapped to each of the DMLs. In this way, two filaments were formed, with a lateral separation of 0.2 mm.

In general, when using the same focal length for both DMLs, the filaments appeared at different depths of the sample. This focal offset can be attributed to beam inhomogeneities in terms of amplitude and phase, which may eventually lead to different position and length of the filaments. The wavefront of our laser was measured and no significant wavefront distortions were observed. However, the non-homogeneous intensity beam profile yielded an unequal energy distribution between both DMLs. As a direct consequence, the beam carrying more energy self-focused closer to the sample's front face. This is shown in the top part Fig. 6.10a, where there is a capture of the longitudinal position of the filaments inside the FS sample. A separation of ~640 µm between them is observed. For this situation, the image recorded by the CCD placed behind the FS sample is that shown as an inset in the bottom part of Fig. 6.10a. The profile along the transversal direction in the CCD screen is also shown. No significant interferences are observed.

In a second configuration, we adjust the design parameter α_j, and consequently the efficiencies of the DMLs. The energies coupled to both foci were equalized. Therefore, same focusing conditions stand for both foci, yielding the generation of two filaments at the same longitudinal position (see top part of Fig. 6.10b). Now, clear fringes are observed and we obtained a fringe visibility V=0.78. The visibility of the fringes is defined as [175]:

$$V = \frac{I_{max} - I_{min}}{I_{max} + I_{min}}. \tag{6.3}$$

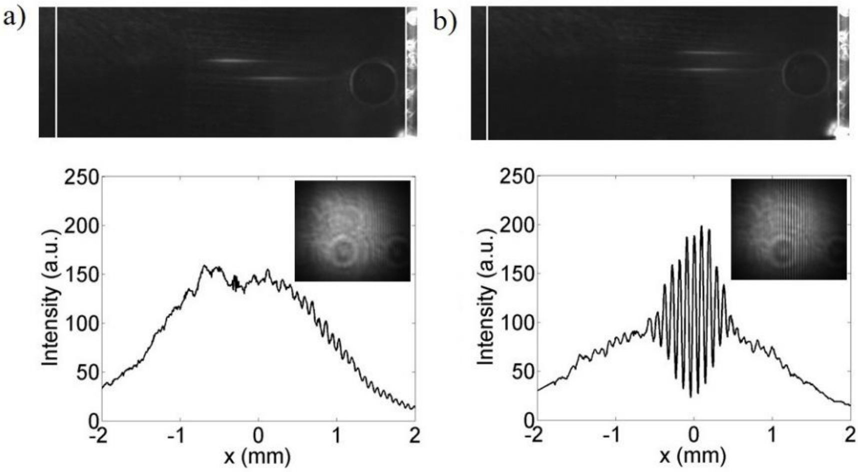

Figure 6.10. Pictures of the filaments' profile (top) and corresponding fringe profile (bottom) a) without and b) with efficiency compensation Inset: interferogram. c) Visibility of the central fringe as a function of the focal length of one of the DMLs.

So far, we have two different results. In a first configuration, the filaments are not in the same position along the propagation axis. In this case interferences are not observed. In a second configuration, the filaments are in the same position along the axis. In this situation interferences are observed. The reason for the existence or not of the interferences is explained in terms of the temporal overlapping of the SC pulses coming from each filament. This temporal separation of the pulses can be partially attributed to the group velocity mismatch between infrared (input pulses) and visible SC pulses, together with the different divergences of the SC and infrared beams. Let's consider the situation where the filaments develop at different positions. As filaments develop in different longitudinal positions, the amount of material traversed by the two different SC pulses will be different for each filament. The group velocity difference between pulses in the infrared and visible regions introduces a time delay between them at the output of the FS sample. Therefore, the two SC pulses do not temporally overlap anymore, and thus interferences at the CCD plane are not observed.

This is in good agreement with the experiments that we also carried out using a Mach-Zehnder interferometer. The complete study can be found in the original article attached to this thesis [**VII**]. In short, the Mach-Zehnder interferometer allows us to control the temporal delay of the two focused pulses and the generation of two filaments with different geometrical separations along the propagation axis. When no time delay is introduced between filaments, i.e. t=0 fs, interference fringes are observed when filaments geometrically overlap (Fig. 6.11a). When filaments develop at different on-axis positions no interferences are observed. This cases agree with the SLM configuration. However, in Fig. 6.11b is shown a different case measured with the Mach-Zehnder interferometer. In this situation filaments develop at different positions but fringes are observed. The reason is that the temporal delay between them is changed, as it is shown in the bottom part of Fig. 6.11b. Now SC pulses overlap again in time at the output of the FS sample.

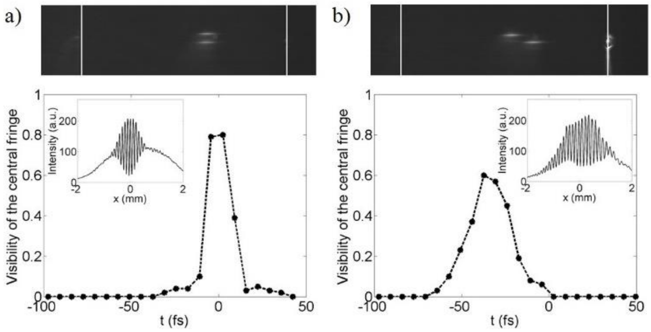

Figure 6.11 Panel a) corresponds to the case where one of the both geometrical foci rely on the same plane, whereas in b) one was slightly displaced. Top: images of filaments profiles. Bottom: visibility of the central fringe as a function of the time delay. Insets show the spatial fringes extracted from the interferogram.

In addition, we performed a study of the fringe visibility as a function of the filaments' relative position. This was done by changing the focal length of DML$_2$. In Fig. 6.12 we depicted the visibility of the fringe located at x=0 (the center of the two beams) as a function of the focal length of DML$_2$. As expected, once the suitable α_j parameter was encoded in both lenses, the highest coherence degree was found for f=60 mm (i.e., same focal length for both DMLs) achieving a visibility of 0.78, and decreased monotonically as the filaments were progressively separated.

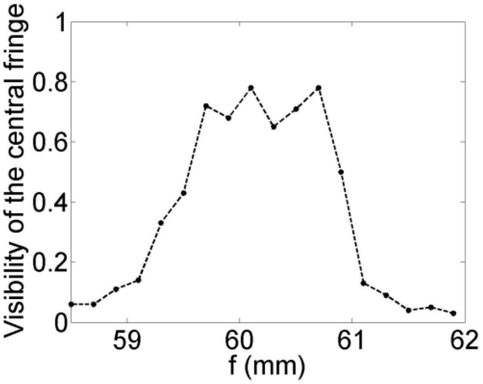

Figure 6.12. . Visibility of the central fringe as a function of the focal length of one of the DMLs

So although the SLM setup is more compact than the interferometric one, it cannot be directly used to study interference phenomena between SC beams unless the efficiency of each DML is corrected. Therefore, just by changing the α_j parameter we can tune the maximum fringe visibility obtained with our SLM proposal. In this way, dynamic control of the fringe visibility is obtained by using DMLs encoded onto a SLM. First, the careful tuning of the DML's efficiency allowed for the optimization of the maximum fringe visibility. On the other hand, by changing the focal length of each DML, we can control easily the fringe visibility at a specific point of space. Thus, the use of a SLM allows for the implementation of compact and robust setups, with large control capabilities in the fringe visibility. The results for the SLM setup are in good agreement with the measurements obtained with the interferometric setup. Moreover, the easy alignment and operation of these systems overcome the problems of the tedious interferometric setups.

Chapter 7. Conclusions

The contribution of the present report to the field of ultrashort optics has several aspects: from the development of new optical devices for ultrashort pulse management, to the application of those devices for triggering laser-matter interaction processes. In this sense, the key point of this Thesis is the use of reconfigurable phase-only SLMs based on LCOS technology for spatial and temporal shaping of femtosecond pulses. The management of femtosecond pulses demands specific strategies to obtain the desired output response while preventing undesirable distortions. Our results show that programmable diffractive optics encoded in SLMs is a powerful tool for ultrashort (~30 fs) beam management. The reconfigurable nature of SLMs allows wavefront control of an input pulsed beam at a micro scale level. In this way, we have developed devices for transferring amplitude and/or phase maps onto the spatial and temporal profile of an ultrashort pulse. Moreover, our proposals result in very compact optical devices, allowing easy-to-align setups especially suitable for non-expert users. We believe that this fact may promote the use of ultrafast technology in many different scientific fields that demands user-friendly devices for ultrashort pulse control.

In this Thesis we have roughly identified three main challenges for ultrashort shaping by means of SLMs: the nature of SLMs, the aberrations carried out by the beam, and the wavelength dependence of diffraction phenomena. The pixelated nature of SLMs and its finite size can eventually be overcome by locally controlling the efficiency response of the SLM. In this way, we have demonstrated that a QDST pulse shaper can be reduced to a simple phase mask encoded in a SLM. With this unprecedented pulse shaper in terms of size, we generated up to 3 concatenated pulses with different temporal intensities. In practical terms it means that any laboratory with just a SLM has a programmable temporal shaper. In this sense, Femtochemistry or material processing may easily benefit from our proposal as the temporal profile of the pulses has a strong influence on the dynamics of chemical reactions and laser induced damage.

The aberrations carried out by the beam may introduce important distortions that highly influence the response of pulse shaping techniques. In this sense, we have presented an innovative spatial phase retrieval method specifically designed for ultrashort pulses where only an SLM and a camera are needed. We found that our proposal, based on sequential pupil segmentation, is a well suited technique to overcome the additional blurring associated with chromatic aberrations in the Fresnel phase retrieval method. Thus, it allows us to measure polychromatic pulsed beams with high accuracy using low dynamic range cameras.

We have also shown that when a pulsed beam passes through a DOE two relevant modifications appear: angular dispersion, due to the strong dependence of the diffraction phenomenon with the wavelength, and temporal stretching, originated by the PTD in free space. For high spatial frequencies, dispersion compensation techniques are required to minimize these effects at the target. In this way, we introduced an all diffractive DCM that, together with CGHs encoded onto the SLM, allows us to obtain structured ultrashort illumination with first order corrected spatiotemporal distortions. This configuration was used for the generation of wide-field fluorescence signals in two-photon microscopy. We experimentally demonstrated that 2-D fluorescence patterns can be generated under ultrashort illumination with high spatial resolution, saving up to 40% of the intensity needed to generate fluorescence signal when no DCM is used. The application of this technique for imaging biological tissue is in progress. In particular, the BRAIN activity map project explicitly aims two-photon excitation of deep tissue, faster scanning strategies or scanless approaches using SLMs to reconstruct the full record of neural activity across complete neural circuits [25]. In this sense, we think that our technique may play an important role to achieve those goals.

Finally, we have performed three different experiments to show how the use of DOEs encoded in SLMs have a great potential to dynamically trigger nonlinear effects. First, we have studied the use of

Dammann lenses under femtosecond illumination for on-axis MF in the bulk of a FS sample. With Dammann lenses we generated multiple on-axis foci of the same intensity, with control over the quantity of foci and their separation. Thus, when focused into the FS sample, multiple filaments appear with a controlled separation of the filaments. Second, we have reported transversal controlled MF in fused silica by encoding a DML array in a SLM for SC generation. We have demonstrated a precise and independent control on (i) the energy coupled to each of the filaments by means of the α parameter, and (ii) the spectrum of the generated SC light by changing the focal length of the DMLs. In a third experiment we have gained fine control over filament interference effects. The tunability of nonlinear processes by means of diffractive optics had been previously shown. However, our experiments indicate that SLMs offer the possibility of working under adverse experimental conditions, and to easily pass from the filamentation to the multifilamentation regime. We believe that the results of these investigations can be useful in applications which demand to manipulate "at will" certain nonlinear effects with intense femtosecond pulses. Such is the case of homogenized MF patterns and/or spectral tunability, including femtosecond laser inscription for performing in-depth parallel processing of transparent dielectrics, time-resolved spectroscopy or tumor treatment by means of filamentation.

Though impressive scientific achievements have been made so far, ultrashort laser beam management is still a young research field and many exciting findings are expected to emerge on its horizon. We strongly believe that the development of programmable optics for femtosecond pulses is a prerequisite for crossing the frontier between research and applied technology. Consequently, we hope that the work developed under this Thesis open the possibility of new strategies that help the consolidation of ultrashort pulses as a transversal working tool.

Annex: Laser facilities used in this thesis

The laser system from University Jaume I is a “FemtoPower compact Pro” from the company Femtolaser. In Fig. 1 a picture of the laser is shown. It has two main beam outputs, the oscillator and the amplifier exits. Moreover, it is also possible to obtain two extra outputs for picosecond pulses before and after the amplification stage.

Oscillator. The pulse duration is <12 fs at intensity FWHM, with a spectral bandwidth >80 nm at FWHM. The repetition pulse frequency is 75 MHz, with an energy per pulse >5.3 nJ. The spatial mode is TEM_{00}, with a beam quality factor M^2 <1.3.

Amplifier. The pulse duration is <30fs at intensity FWHM, with a spectral bandwidth >40nm at FWHM. The repetition pulse frequency is 1KHz, with an energy per pulse >800 mJ. The spatial mode is TEM_{00}, with a beam quality factor M^2 <2.

Figure 1. Photograph of the Femtolaser laser system at the University Jaume I of Castellón.

As it has been used in almost all the works included in this Thesis, it is worth to comment in detail the characteristics of the used SLM:

- Two reflective phase-only parallel aligned nematic (PAN) LCoS SLMs (Holoeye Pluto) HES-6010-NIR-II (optimized for 700-1000 nm). Available modulation screen of 1920x1080 pixels, with 8µm of pixel pitch and fill factor of 87%. Modulation efficiency is around 60% [176]. Modulation exceeding 2π is reached for the working range. The damage threshold was determined to be approximately 0,25 TW/cm^2 [85] for pulsed illumination and 2W/cm^2 for CW laser.
- Reflective phase-only PAN LCoS SLM (Holoeye Pluto) HES-6010-VIS (optimized for 420-850 nm). The rest of the parameters are the same than the previously described.

The laboratory also disposes of other tools for beam manipulation and beam diagnostics:

- Beam profiler, 14 bit digital charge-coupled device camera, 1360 1024 pixels, size 6.45 m (WinCamD-UCD23)
- Shack-Hartmann sensor WFS150-5C with 150 µm and working region 300-1100 nm.
- External passive compression system up to 10 fs.
- Temporal Diagnostic: Intensity autocorrelator, FROG, and SPIDER. These equipments make it possible the temporal characterization of pulses with temporal durations spanning from a few femtoseconds to tens of picosecond and a wide range of input energies.
- CCD and spectrometers for the visible and infrared region.

For the flat-top beam generation experiment, performed during a research stay at Centro de láseres pulsados de Salamanca (CLPU), the laser that we used was:

HE Pro CEP laser: This light source is a 4th generation Femtopower system that offers ultrashort pulses (23 fs after amplifier) and few cycle pulses (5 fs or less, after hollow core fibre post-compression) with carrier envelope phase stabilised and energy in the range of mJ. It works at a central wavelength around 800 nanometres, in the near-infrared range; and in a spectral band around 50 nm FWHM (after amplifier) and > 200 nm (oscillator and after post-compression).

Resumen en español

Objeto y objetivos de la investigación.

Lo láseres ultracortos son actualmente una herramienta esencial en numerosos campos de la investigación científica. La fabricación y comercialización de láseres pulsados está avanzando muy rápido, traduciéndose en fuentes más compactas, fiables y asequibles económicamente. Como resultado, este tipo de láseres están experimentando una demanda cada vez más mayor, incluso por parte de usuarios que no son expertos en la física de los láseres pulsados.

En la mayoría de ocasiones tener una fuente de pulsos ultracortos no es sinónimo de que pueda usarse directamente en un experimento. Normalmente el haz de salida de nuestro láser necesita ser previamente manipulado. En otras palabras, algunas características del haz, como su perfil temporal o espacial, deben ser modificadas para cumplir los requisitos que el usuario crea convenientes para cada aplicación concreta. Todo esto requiere de herramientas de control del haz láser cada vez más orientadas al usuario final, que en esencia demanda dispositivos robustos y fiables, con interfaces sencillas, y con un funcionamiento versátil capaz de adaptarse a cada situación.

Esta Tesis se centra en la manipulación de pulsos de femtosegundo. En ella pretendemos explotar el potencial de los elementos ópticos difractivos (DOEs en sus siglas en inglés) para diseñar nuevos dispositivos que permitan conformar en tiempo real y de forma programable un pulso ultracorto. El uso de DOEs permite cancelar o reducir al mínimo el impacto de las aberraciones del haz de entrada y, en general, esculpir a elección del usuario cualquier tipo de fase para un control total sobre la estructura espaciotemporal del campo eléctrico. Pero lo que es más importante: los DOEs pueden ser codificados en moduladores espaciales de luz (SLMs en sus siglas en inglés). Los SLMs son dispositivos opto-electrónicos controlados por ordenador capaces de modular fase, amplitud y polarización a una escala micrométrica. Su uso permite la generación programable y versátil de DOEs capaces de modular la luz prácticamente en tiempo real. Todas estas características hacen de los SLMs dispositivos tremendamente atractivos para el usuario final.

En resumen, el objetivo de esta tesis es doble:

- El primero es el desarrollo de nuevos dispositivos completamente ópticos para manipular pulsos de femtosegundo de una forma controlada. Esto es llevado a cabo mediante la codificación de DOEs en SLMs.
- El segundo es el estudio de los dispositivos mencionados arriba para nuevas aplicaciones en el campo de la óptica no lineal.

Planteamiento y aportaciones originales.

En primer lugar, hemos desarrollado dispositivos para transferir mapas de amplitud y/o fase al perfil espacial y temporal de un pulso ultracorto. Esto se ha llevado a cabo mediante la codificación de lentes difractivas, lentes de Dammann y hologramas generados por ordenador (CGHs en sus siglas en inglés) en los SLMs. De esta forma, hemos demostrado que un conformador temporal de haz puede ser reducido a tan solo una máscara de fase codificada en un SLM. Con este conformador temporal, que no tiene precedentes en términos de tamaño, hemos demostrado la generación de hasta tres pulsos concatenados, todo ello con control individual de la intensidad temporal de cada uno.

El conformado de pulsos ultracortos puede verse influenciado por las aberraciones del haz laser, hasta el punto de introducir distorsiones que invalidan las técnicas de conformado en términos de eficiencia y calidad del perfil espacial y temporal generado. Por esta razón, hemos desarrollado un método nuevo para medir y corregir las aberraciones del haz especialmente diseñado para pulsos ultracortos. Este método solo requiere de un SLM y una cámara, y arroja resultados precisos incluso cuando se trabaja con cámaras con poco rango dinámico y haces policromáticos. Las aberraciones no solo son medidas, sino que gracias a la naturaleza programable de los SLMs pueden ser corregidas por el propio SLM. Esto permite medir y corregir aberraciones con el SLM situado exactamente en la posición donde vaya a ser usado en futuros experimentos, sin necesidad de introducir sensores de frente de onda externos.

Por otro lado, hemos demostrado que cuando un haz pulsado pasa a través de un DOE aparecen dos efectos relevantes: dispersión angular, debido a la fuerte dependencia del fenómeno de la difracción con la longitud de onda, y ensanchamiento temporal originado por la diferencia temporal de propagación entre pulsos (PTD en sus siglas en inglés) en el espacio libre. Esto se traduce en un acoplamiento espaciotemporal que causa una notable degradación de la imagen de salida y un ensanchamiento temporal del pulso. Por este motivo, para frecuencias espaciales altas se necesitan técnicas de compensación de la dispersión que minimicen estos efectos en el objetivo. De esta manera, hemos introducido un dispositivo compensador de la dispersión (DCM en sus siglas en inglés) que, junto con CGHs codificados en SLMs, nos permite generar iluminación ultracorta estructurada con una corrección a primer orden de las distorsiones espaciotemporales. Esta configuración ha sido empleada para la generación de señal de fluorescencia de campo amplio en microscopía a dos fotones. El uso de esta técnica mejora la resolución temporal de las técnicas de microscopía multifotón de escaneo convencionales, ya que no es necesario un escaneo secuencial de la muestra. Nuestra propuesta permite extender las técnicas de campo amplio a láseres ultracortos, evitando distorsiones. Esto tiene muchas ventajas, ya que la eficiencia de excitación y la profundidad de penetración se incrementan conforme menor es la duración temporal de nuestro pulso.

En una segunda parte, hemos explotado las características de los dispositivos antes mencionados para nuevas aplicaciones en el campo de la óptica no lineal. En este sentido hemos desarrollado tres experimentos que muestran el enorme potencial que tienen los DOEs codificados en SLMs para controlar dinámicamente efectos no lineales. Primero, hemos estudiado el uso de lentes de Dammann bajo iluminación ultracorta para generar multifilamentos en eje en un vidrio de sílice fundida. Las lentes de Dammann permiten la generación de múltiples focos en eje con la misma intensidad, permitiendo el control tanto de la cantidad de focos como de la separación entre ellos. Cuando el patrón de multifocos es focalizado en el vidrio de sílice fundida, aparecen múltiples filamentos con una separación controlada. En segundo lugar, mediante la codificación de una matriz de microlentes en el SLM, hemos demostrado la generación controlada de multifilamentos también en el plano transversal del vidrio de sílice fundida. Hemos demostrado control preciso e independiente sobre a) la energía acoplada a cada filamento, y b) el espectro de supercontínuo generado mediante el control dinámico de la focal de cada microlente. Mediante esta misma configuración, también hemos comprobado en un tercer experimento que podemos controlar efectos interferenciales entre los filamentos que se forman.

Conclusiones

La contribución del presente trabajo al campo de la óptica ultrarrápida tiene diferentes vertientes, que van desde el desarrollo de nuevos dispositivos ópticos para el control de pulsos ultracortos, a la aplicación de estos dispositivos para moldear procesos de interacción laser-materia. El punto clave de esta tesis es la utilización de SLMs de fase basados en tecnología de cristal líquido para el conformado espacial y temporal de pulsos de femtosegundo.

Nuestro resultados muestran que la óptica difractiva programable es una poderosa herramienta para el conformado de haces ultracortos (~30 fs). Además, nuestras propuestas se traducen en sistemas ópticos muy compactos, favoreciendo montajes fáciles de alinear especialmente útiles para usuarios no expertos. Creemos que este hecho puede promover el uso de tecnología ultrarrápida en diferentes campos científicos que demandan dispositivos fiables y sencillos para manejar pulsos ultracortos.

El perfil temporal de un pulso ultracorto juega un papel fundamental en el control de la dinámica de las reacciones químicas, así como en el daño inducido a un material cuando es procesado mediante este tipo de iluminación. Por ello, creemos que el desarrollo de un conformador temporal de pulsos que consta tan solo de una máscara codificada en un SLM puede ser beneficioso para el campo de la femtoquímica y el de procesado de materiales con pulsos de femtosegundo.

Por otro lado, hemos demostrado la generación de microscopía multifotón estructurada con iluminación ultracorta, aumentando así la resolución espacial y ahorrando hasta un 40 % de energía respecto a sistemas sin compensación de la dispersión. La aplicación de esta técnica para realizar imágenes de tejido biológico tiene un gran potencial. En concreto, el proyecto BRAIN, que tiene como objetivo registrar mapas neuronales extensos, demanda explícitamente técnicas de excitación a dos fotones en tejido profundo, estrategias de escaneo más rápidas o estrategias de campo amplio sin escaneo utilizando SLMs para reconstruir la actividad neuronal a través de circuitos neuronales completos. En este sentido, creemos que nuestra técnica puede jugar un papel importante para conseguir estos objetivos.

La sintonización de procesos no lineales ya había sido demostrada con anterioridad. Sin embargo, nuestros experimentos indican que el uso de SLMs ofrece la posibilidad de trabajar bajo condiciones experimentales adversas. También, gracias a la versatilidad de los SLMs, permite fácilmente la generación de multifilamentos. Por ello, creemos que los resultados de nuestras investigaciones pueden ser útiles en aplicaciones que demanden manipular ciertos efectos no lineales con pulsos de femtosegundo. Este es el caso de la generación de patrones de multifilamentos, la sintonización espectral de señal de supercontinuo, el procesado en profundidad de materiales dieléctricos o el tratamiento de tumores mediante filamentación.

Aunque se han hecho avances científicos muy remarcables hasta la fecha, el conformado de pulsos ultracortos es aún un campo de investigación joven con un gran horizonte por delante de nuevos y excitantes descubrimientos. Creemos firmemente que el desarrollo de óptica programable para pulsos de femtosegundo es un prerrequisito para cruzar la frontera entre el campo de la investigación y el de la tecnología aplicada. En consecuencia, esperamos que el trabajo desarrollado en esta Tesis abra la puerta para nuevas estrategias que ayuden a la consolidación de los pulsos ultracortos como una herramienta de trabajo transversal.

References.

1. Hecht, J., *The Laser Guidebook*. 1986: McGraw-Hill.
2. Silfvast, W. T., *Laser Fundamentals*. 2004: Cambridge University Press.
3. Weber, M. J., *Handbook of Laser Wavelengths*. 1998: CRC Press.
4. McClung, F., et al., *Giant Optical Pulsations from Ruby.* Journal of Applied Physics, 1962. **33**(3): p. 828-829.
5. Hargrove, L. E., et al., *Locking of He–Ne Laser Modes Induced by Synchronous Intracavity Modulation.* Applied Physics Letters, 1964. **5**(1): p. 4-5.
6. Moulton, P. F., *Spectroscopic and Laser Characteristics of Ti:Al2O3.* JOSA B, 1986. **3**(1): p. 125-133.
7. Strickland, D., et al., *Compression of Amplified Chirped Optical Pulses.* Optics Communications, 1985. **55**(6): p. 447-449.
8. Diels, J.-C., et al., *Ultrashort Laser Pulse Phenomena*. 2006: Academic press.
9. Krausz, F., et al., *Attosecond Physics.* Reviews of Modern Physics, 2009. **81**(1): p. 163.
10. Alonso, B., et al., *Spatiotemporal Amplitude-and-Phase Reconstruction by Fourier-Transform of Interference Spectra of High-Complex-Beams.* Journal of the Optical Society of America B, 2010. **27**(5): p. 933-940.
11. Iaconis, C., et al., *Spectral Phase Interferometry for Direct Electric-Field Reconstruction of Ultrashort Optical Pulses.* Optics Letters, 1998. **23**(10): p. 792-794.
12. Miranda, M., et al., *Simultaneous Compression and Characterization of Ultrashort Laser Pulses Using Chirped Mirrors and Glass Wedges.* Optics Express, 2012. **20**(1): p. 688-697.
13. Trebino, R., *Frequency-Resolved Optical Gating: The Measurement of Ultrashort Laser Pulses*. Vol. 1. 2000: Springer.
14. Sibbett, W., et al., *The Development and Application of Femtosecond Laser Systems.* Optics Express, 2012. **20**(7): p. 6989-7001.
15. Snavely, R., et al., *Intense High-Energy Proton Beams from Petawatt-Laser Irradiation of Solids.* Physical Review Letters, 2000. **85**(14): p. 2945.
16. Huang, D., et al., *Optical Coherence Tomography.* Science, 1991. **254**(5035): p. 1178.

17. Hee, M. R., et al., *Femtosecond Transillumination Optical Coherence Tomography.* Optics Letters, 1993. **18**(12): p. 950-952.
18. Mourou, G., et al., *The Extreme Light Infrastructure: Optics' Next Horizon.* Optics and Photonics News, 2011. **22**(7): p. 47-51.
19. Zewail, A. H., *Femtochemistry: Atomic-Scale Dynamics of the Chemical Bond.* The Journal of Physical Chemistry A, 2000. **104**(24): p. 5660-5694.
20. Momma, C., et al., *Precise Laser Ablation with Ultrashort Pulses.* Applied Surface Science, 1997. **109**: p. 15-19.
21. Vogel, A., et al., *Mechanisms of Femtosecond Laser Nanosurgery of Cells and Tissues.* Applied Physics B, 2005. **81**(8): p. 1015-1047.
22. Alivisatos, A. P., et al., *Nanotools for Neuroscience and Brain Activity Mapping.* ACS nano, 2013. **7**(3): p. 1850-1866.
23. Nikolenko, V., et al., *Slm Microscopy: Scanless Two-Photon Imaging and Photostimulation with Spatial Light Modulators.* Frontiers in Neural Circuits, 2008. **2**.
24. Packer, A. M., et al., *Two-Photon Optogenetics of Dendritic Spines and Neural Circuits.* Nature Methods, 2012. **9**(12): p. 1202-1205.
25. Alivisatos, A. P., et al., *The Brain Activity Map Project and the Challenge of Functional Connectomics.* Neuron, 2012. **74**(6): p. 970-974.
26. Mosk, A. P., et al., *Controlling Waves in Space and Time for Imaging and Focusing in Complex Media.* Nature Photonics, 2012. **6**(5): p. 283-292.
27. Katz, O., et al., *Focusing and Compression of Ultrashort Pulses through Scattering Media.* Nature photonics, 2011. **5**(6): p. 372-377.
28. McCabe, D. J., et al., *Spatio-Temporal Focusing of an Ultrafast Pulse through a Multiply Scattering Medium.* Nature Communications, 2011. **2**: p. 447.
29. Meesat, R., et al., *Cancer Radiotherapy Based on Femtosecond Ir Laser-Beam Filamentation Yielding Ultra-High Dose Rates and Zero Entrance Dose.* Proceedings of the National Academy of Sciences, 2012. **109**(38): p. E2508-E2513.
30. Paul, P. M., et al., *Observation of a Train of Attosecond Pulses from High Harmonic Generation.* Science, 2001. **292**(5522): p. 1689-1692.
31. Goulielmakis, E., et al., *Single-Cycle Nonlinear Optics.* Science, 2008. **320**(5883): p. 1614-1617.
32. Malka, V., et al., *Practicability of Protontherapy Using Compact Laser Systems.* Medical Physics, 2004. **31**(6): p. 1587-1592.

33. Vorobyev, A. Y., et al., *Direct Femtosecond Laser Surface Nano/Microstructuring and Its Applications.* Laser & Photonics Reviews, 2013. **7**(3): p. 385-407.
34. Baldacchini, T., et al., *Superhydrophobic Surfaces Prepared by Microstructuring of Silicon Using a Femtosecond Laser.* Langmuir, 2006. **22**(11): p. 4917-4919.
35. Stratakis, E., *Nanomaterials by Ultrafast Laser Processing of Surfaces.* Science of Advanced Materials, 2012. **4**(3-4): p. 407-431.
36. Dammann, H., et al., *Coherent Optical Generation and Inspection of Two-Dimensional Periodic Structures.* Journal of Modern Optics, 1977. **24**(4): p. 505-515.
37. Dubrouil, A., et al., *Controlling High Harmonics Generation by Spatial Shaping of High-Energy Femtosecond Beam.* Optics Letters, 2011. **36**(13): p. 2486-2488.
38. Goorden, S. A., et al., *Superpixel-Based Spatial Amplitude and Phase Modulation Using a Digital Micromirror Device.* Optics Express, 2014. **22**(15): p. 17999-18009.
39. Matsumoto, N., et al., *Generation of High-Quality Higher-Order Laguerre-Gaussian Beams Using Liquid-Crystal-on-Silicon Spatial Light Modulators.* Journal of the Optical Society of America A, 2008. **25**(7): p. 1642-1651.
40. Mendoza-Yero, O., et al., *Encoding Complex Fields by Using a Phase-Only Optical Element.* Optics Letters, 2014. **39**(7): p. 1740-1743.
41. Moreno, I., et al., *Encoding Generalized Phase Functions on Dammann Gratings.* Optics Letters, 2010. **35**(10): p. 1536-1538.
42. Strelkov, V., et al., *Generation of Isolated Attosecond Pulses by Spatial Shaping of a Femtosecond Laser Beam.* New Journal of Physics, 2008. **10**(8): p. 083040.
43. Wyrowski, F., *Diffractive Optical Elements: Iterative Calculation of Quantized, Blazed Phase Structures.* Journal of the Optical Society of America A, 1990. **7**(6): p. 961-969.
44. Beckers, J. M., *Adaptive Optics for Astronomy-Principles, Performance, and Applications.* Annual Review of Astronomy and Astrophysics, 1993. **31**: p. 13-62.
45. Martínez-Cuenca, R., et al., *Closed-Loop Adaptive Optics with a Single Element for Wavefront Sensing and Correction.* Optics Letters, 2011. **36**(18): p. 3702-3704.
46. Weiner, A. M., *Femtosecond Pulse Shaping Using Spatial Light Modulators.* Review of Scientific Instruments, 2000. **71**(5): p. 1929-1960.

47. Weiner, A. M., *Ultrafast Optical Pulse Shaping: A Tutorial Review.* Optics Communications, 2011. **284**(15): p. 3669-3692.
48. Masters, B. R., et al., *Handbook of Biomedical Nonlinear Optical Microscopy*. 2008: Oxford University Press New York:.
49. Tang, S., et al., *Effect of Pulse Duration on Two-Photon Excited Fluorescence and Second Harmonic Generation in Nonlinear Optical Microscopy.* Journal of Biomedical Optics, 2006. **11**(2): p. 020501-020501-3.
50. Boyd, R. W., *Nonlinear Optics*. 2003: Academic press.
51. Träger, F., *Springer Handbook of Lasers and Optics*. 2007: Springer.
52. Weiner, A. M., et al., *High-Resolution Femtosecond Pulse Shaping.* Journal of the Optical Society of America B, 1988. **5**(8): p. 1563-1572.
53. Tournois, P., *Acousto-Optic Programmable Dispersive Filter for Adaptive Compensation of Group Delay Time Dispersion in Laser Systems.* Optics Communications, 1997. **140**(4–6): p. 245-249.
54. Verluise, F., et al., *Amplitude and Phase Control of Ultrashort Pulses by Use of an Acousto-Optic Programmable Dispersive Filter: Pulse Compression and Shaping.* Optics Letters, 2000. **25**(8): p. 575-577.
55. Mínguez-Vega, G., et al., *High Spatiotemporal Resolution in Multifocal Processing with Femtosecond Laser Pulses.* Optics Letters, 2006. **31**(17): p. 2631-2633.
56. Martínez-León, L., et al., *Spatial-Chirp Compensation in Dynamical Holograms Reconstructed with Ultrafast Lasers.* Applied Physics Letters, 2009. **94**(1): p. 011104.
57. Siegman, A. E., *Lasers*. 1986: University Science Books.
58. Herzig, H. P., *Micro-Optics: Elements, Systems and Applications*. 1997: CRC Press.
59. Mao, S., et al., *Dynamics of Femtosecond Laser Interactions with Dielectrics.* Applied Physics A, 2004. **79**(7): p. 1695-1709.
60. Borrego Varillas, R., *Role of Wavefront Aberrations of Amplified Femtosecond Pulses in Nonlinear Optics*. 2012, University of Salamanca.
61. Shen, Y.-R., *Principles of Nonlinear Optics.* 1984.
62. Chiao, R., et al., *Self-Focusing of Optical Beams*, in *Self-Focusing: Past and Present*. 2009, Springer. p. 129-143.
63. Couairon, A., et al., *Femtosecond Filamentation in Transparent Media.* Physics Reports, 2007. **441**(2): p. 47-189.
64. Bergé, L., et al., *Multiple Filamentation of Terawatt Laser Pulses in Air.* Physical Review Letters, 2004. **92**(22): p. 225002.

65. Schröder, H., et al., *From Random to Controlled Small-Scale Filamentation in Water.* Optics Express, 2004. **12**(20): p. 4768-4774.
66. Nguyen, N., et al., *Optical Breakdown Versus Filamentation in Fused Silica by Use of Femtosecond Infrared Laser Pulses.* Optics Letters, 2003. **28**(17): p. 1591-1593.
67. Liu, W., et al., *Femtosecond Laser Pulse Filamentation Versus Optical Breakdown in H2o.* Applied Physics B, 2003. **76**(3): p. 215-229.
68. Poumellec, B., et al., *Modification Thresholds in Femtosecond Laser Processing of Pure Silica: Review of Dependencies on Laser Parameters [Invited].* Optical Materials Express, 2011. **1**(4): p. 766-782.
69. Nagura, C., et al., *Generation and Characterization of Ultrafast White-Light Continuum in Condensed Media.* Applied Optics, 2002. **41**(18): p. 3735-3742.
70. Kolesik, M., et al., *Physical Factors Limiting the Spectral Extent and Band Gap Dependence of Supercontinuum Generation.* Physical Review Letters, 2003. **91**(4): p. 043905.
71. Ashcom, J. B., et al., *Numerical Aperture Dependence of Damage and Supercontinuum Generation from Femtosecond Laser Pulses in Bulk Fused Silica.* Journal of the Optical Society of America B, 2006. **23**(11): p. 2317-2322.
72. Sun, Q., et al., *Effect of Spherical Aberration on the Propagation of a Tightly Focused Femtosecond Laser Pulse inside Fused Silica.* Journal of Optics A: Pure and Applied Optics, 2005. **7**(11): p. 655.
73. Romero, C., et al., *Diffractive Optics for Spectral Control of the Supercontinuum Generated in Sapphire with Femtosecond Pulses.* Optics Express, 2011. **19**(6): p. 4977-4984.
74. Pawley, J. B., *Confocal and Two-Photon Microscopy: Foundations, Applications and Advances.* Microscopy Research and Technique, 2002. **59**(2): p. 148-149.
75. Hawkes, P. W., et al., *Science of Microscopy.* 2007.
76. Teich, M. C., et al., *Fundamentals of Photonics.* Canada, Wiley Interscience, 1991: p. 3.
77. So, P. T., et al., *Two-Photon Excitation Fluorescence Microscopy.* Annual Review of Biomedical Engineering, 2000. **2**(1): p. 399-429.
78. Steinbauer, M., et al., *Characterization and Prevention of Phototoxic Effects in Intravital Fluorescence Microscopy in the Hamster Dorsal Skinfold Model.* Langenbeck's Archives of Surgery, 2000. **385**(4): p. 290-298.

79. Franken, P., et al., *Generation of Optical Harmonics.* Physical Review Letters, 1961. **7**(4): p. 118-119.
80. Zhu, P., et al., *High-Resolution Optical Control of Spatiotemporal Neuronal Activity Patterns in Zebrafish Using a Digital Micromirror Device.* Nature Protocols, 2012. **7**(7): p. 1410-1425.
81. Maurer, C., et al., *What Spatial Light Modulators Can Do for Optical Microscopy.* Laser & Photonics Reviews, 2011. **5**(1): p. 81-101.
82. Lazarev, G., et al., *Lcos Spatial Light Modulators: Trends and Applications*. 2012, Wiley-VCH. p. 1-30.
83. Bleha, W. P., et al. *Advances in Liquid Crystal on Silicon (Lcos) Spatial Light Modulator Technology*. in *SPIE Defense, Security, and Sensing*. 2013. International Society for Optics and Photonics.
84. Bock, M., et al., *Spectral and Temporal Response of Liquid-Crystal-on-Silicon Spatial Light Modulators.* Applied Physics Letters, 2008. **92**(15): p. 151105.
85. *Holoeye Photonics Ag, Hdtv Phase Panel Developer Kit for Fs-Laser Applications, Heo 1080p Application Note*.
86. García-Márquez, J., et al., *Flicker Minimization in an Lcos Spatial Light Modulator.* Optics Express, 2012. **20**(8): p. 8431-8441.
87. Moreno, I., et al., *Time Fluctuations of the Phase Modulation in a Liquid Crystal on Silicon Display: Characterization and Effects in Diffractive Optics.* Optics Express, 2008. **16**(21): p. 16711-16722.
88. Ritsch-Marte, M. *Applications of Spatial Light Modulators for Optical Trapping and Imaging*. *Frontiers in Optics*. 2010. Optical Society of America.
89. Persson, M., et al., *Reducing the Effect of Pixel Crosstalk in Phase Only Spatial Light Modulators.* Optics Express, 2012. **20**(20): p. 22334-22343.
90. Reichelt, S., *Spatially Resolved Phase-Response Calibration of Liquid-Crystal-Based Spatial Light Modulators.* Applied Optics, 2013. **52**(12): p. 2610-2618.
91. Xun, X., et al., *Phase Calibration of Spatially Nonuniform Spatial Light Modulators.* Applied Optics, 2004. **43**(35): p. 6400-6406.
92. Otón, J., et al., *Multipoint Phase Calibration for Improved Compensation of Inherent Wavefront Distortion in Parallel Aligned Liquid Crystal on Silicon Displays.* Applied Optics, 2007. **46**(23): p. 5667-5679.
93. Zhang, Z., et al., *Diffraction Based Phase Compensation Method for Phase-Only Liquid Crystal on Silicon Devices in Operation.* Applied Optics, 2012. **51**(17): p. 3837-3846.

94. Wolfgang Osten, C. K. y. J. L., *Evaluation and Application of Spatial Light Modulators for Optical Metrology.* Óptica Pura y Aplicada, 2005. **38**(3): p. 71-81.

95. Sprünken, D. P., *A 2d Spatial Light Modulator for Spatio-Temporal Shaping* 2008.

96. Amako, J., et al., *Kinoform Using an Electrically Controlled Birefringent Liquid-Crystal Spatial Light Modulator.* Applied Optics, 1991. **30**(32): p. 4622-4628.

97. Bergeron, A., et al., *Phase Calibration and Applications of a Liquid-Crystal Spatial Light Modulator.* Applied Optics, 1995. **34**(23): p. 5133-5139.

98. Frumker, E., et al., *Phase and Amplitude Pulse Shaping with Two-Dimensional Phase-Only Spatial Light Modulators.* Journal of the Optical Society of America B, 2007. **24**(12): p. 2940-2947.

99. Zhang, Z., et al., *Simple Method for Measuring Phase Modulation in Liquid Crystal Televisions.* Optical Engineering, 1994. **33**(9): p. 3018-3022.

100. Duran, V., et al., *Cell Parameter Determination of a Twisted-Nematic Liquid Crystal Display by Single-Wavelength Polarimetry.* Journal of Applied Physics, 2005. **97**(4): p. 043101.

101. Vaughan, J. C., *Two-Dimensional Ultrafast Pulse Shaping and Its Application to Coherent Control and Spectroscopy*. 2005, Massachusetts Institute of Technology.

102. Kohler, C., et al., *Characterization of a Spatial Light Modulator and Its Application in Phase Retrieval.* Applied Optics, 2009. **48**(20): p. 4003-4008.

103. Ferreira, F. P., et al., *Direct Calibration of a Spatial Light Modulator by Lateral Shearing Interferometry.* Optics Express, 2010. **18**(8): p. 7899-7904.

104. Martínez-León, L., et al., *Phase Calibration of Spatial Light Modulators by Means of Fresnel Images.* Journal of Optics A: Pure and Applied Optics, 2009. **11**(12): p. 125405.

105. Laude, V., *Twisted-Nematic Liquid-Crystal Pixelated Active Lens.* Optics communications, 1998. **153**(1): p. 134-152.

106. Carcolé, E., et al., *Diffraction Theory of Fresnel Lenses Encoded in Low-Resolution Devices.* Applied Optics, 1994. **33**(2): p. 162-174.

107. Moreno, I., et al., *Modulation Light Efficiency of Diffractive Lenses Displayed in a Restricted Phase-Mostly Modulation Display.* Applied Optics, 2004. **43**(34): p. 6278-6284.

108. Millán, M. S., et al., *Dynamic Compensation of Chromatic Aberration in a Programmable Diffractive Lens.* Optics Express, 2006. **14**(20): p. 9103-9112.
109. Sinzinger, S., et al., *Microoptics*. 2005: Wiley-VCH Verlag GmbH & Co. KGaA.
110. Moreno, V., et al., *High Efficiency Diffractive Lenses: Deduction of Kinoform Profile.* American Journal of Physics, 1997. **65**(6): p. 556-562.
111. Oshika, T., et al., *Comparison of Corneal Wavefront Aberrations after Photorefractive Keratectomy and Laser in Situ Keratomileusis.* American Journal of Ophthalmology, 1999. **127**(1): p. 1-7.
112. Grimm, B., et al., *Objective Measurement of Wave Aberrations of the Human Eye with the Use of a Hartmann-Shack Wave-Front Sensor.* Journal of the Optical Society of America A, 1994. **11**(7): p. 1949-1957.
113. Bellucci, R., et al., *Comparison of Wavefront Aberrations and Optical Quality of Eyes Implanted with Five Different Intraocular Lenses.* Journal of Refractive Surgery (Thorofare, NJ: 1995), 2003. **20**(4): p. 297-306.
114. Akaoka, K., et al. *Closed-Loop Wavefront Correction of Ti:Sapphire Chirped Pulse Amplification Laser Beam*. 1998. Proc. SPIE 3265, Solid State Lasers VII, 219.
115. Planchon, T. A., et al., *Adaptive Wavefront Correction on a 100-Tw/10-Hz Chirped Pulse Amplification Laser and Effect of Residual Wavefront on Beam Propagation.* Optics Communications, 2005. **252**(4–6): p. 222-228.
116. Schäfer, B., et al. *Characterisation, Wavefront Reconstruction, and Propagation of Ultra-Broadband Laser Pulses from Hartmann-Shack Measurements*. *Optics & Photonics 2005*. 2005. International Society for Optics and Photonics.
117. Thibos, L. N., et al., *Standards for Reporting the Optical Aberrations of Eyes.* Journal of Refractive Surgery, 2002. **18**(5): p. S652-S660.
118. Ophthalmics., A. N. S. f., *Ansi® Z80.28-2009, Annex 6.*
119. Bahk, S. W., et al., *Generation and Characterization of the Highest Laser Intensities (1022 W/Cm2).* Optics Letters, 2004. **29**(24): p. 2837-2839.
120. Yanovsky, V., et al., *Ultra-High Intensity- 300-Tw Laser at 0.1 Hz Repetition Rate.* Optics Express, 2008. **16**(3): p. 2109-2114.

121. Wattellier, B., et al., *High-Power Short-Pulse Laser Repetition Rate Improvement by Adaptive Wave Front Correction.* Review of Scientific Instruments, 2004. **75**(12): p. 5186-5192.
122. Ruiz de la Cruz, A., et al., *Independent Control of Beam Astigmatism and Ellipticity Using a Slm for Fs-Laser Waveguide Writing.* Optics Express, 2009. **17**(23): p. 20853-20859.
123. Hauri, C., et al., *Validity of Wave-Front Reconstruction and Propagation of Ultrabroadband Pulses Measured with a Hartmann-Shack Sensor.* Optics Letters, 2005. **30**(12): p. 1563-1565.
124. Bueno, J. M., et al., *Temporal Wavefront Stability of an Ultrafast High-Power Laser Beam.* Applied Optics, 2009. **48**(4): p. 770-777.
125. Mínguez-Vega, G., et al., *Diffractive Optics for Quasi-Direct Space-to-Time Pulse Shaping.* Optics Express, 2008. **16**(21): p. 16993-16998.
126. Loriot, V., et al., *Experimental Demonstration of the Quasi-Direct Space-to-Time Pulse Shaping Principle.* Photonics Technology Letters, IEEE, 2012. **24**(4): p. 273-275.
127. Matsuoka, S., et al., *Wave-Front Measurements of Terawatt-Class Ultrashort Laser Pulses by the Fresnel Phase-Retrieval Method.* Journal of the Optical Society of America B, 2000. **17**(4): p. 663-667.
128. Jeong, T.-M., et al., *Reconstruction of Wavefront Aberration of 100-Tw Ti: Sapphire Laser Pulse Using Phase Retrieval Method.* Journal of the Optical Society of Korea, 2008. **12**(3): p. 186-191.
129. *Iso Standard 11146 "Lasers and Laser-Related Equipment – Test Methods for Laser Beam Widths, Divergence Angles and Beam Propagation Ratios"* 2005.
130. Warren, W. S., et al., *Coherent Control of Quantum Dynamics: The Dream Is Alive.* Science, 1993. **259**(5101): p. 1581-1589.
131. Bartels, R., et al., *Shaped-Pulse Optimization of Coherent Emission of High-Harmonic Soft X-Rays.* Nature, 2000. **406**(6792): p. 164-166.
132. Dudovich, N., et al., *Single-Pulse Coherently Controlled Nonlinear Raman Spectroscopy and Microscopy.* Nature, 2002. **418**(6897): p. 512-514.
133. Ogilvie, J. P., et al., *Use of Coherent Control for Selective Two-Photon Fluorescence Microscopy in Live Organisms.* Optics Express, 2006. **14**(2): p. 759-766.
134. Jiang, Z., et al., *Fully Dispersion-Compensated 500 Fs Pulse Transmission over 50 Km Single-Mode Fiber.* Optics Letters, 2005. **30**(12): p. 1449-1451.

135. Shverdin, M., et al., *Generation of a Single-Cycle Optical Pulse.* Physical Review Letters, 2005. **94**(3): p. 033904.

136. Leaird, D., et al., *Femtosecond Optical Packet Generation by a Direct Space-to-Time Pulse Shaper.* Optics Letters, 1999. **24**(12): p. 853-855.

137. Mendoza-Yero, O., et al., *Diffractive Pulse Shaper for Arbitrary Waveform Generation.* Optics Letters, 2010. **35**(4): p. 535-537.

138. Mendoza-Yero, O., et al., *Synthesis of Fractal Light Pulses by Quasi-Direct Space-to-Time Pulse Shaping.* Optics Letters, 2012. **37**(7): p. 1145-1147.

139. Minguez-Vega, G., et al., *Optical Filter Based on a Spatially Patterned Kinoform Diffractive Lens.* Photonics Technology Letters, IEEE, 2009. **21**(6): p. 347-349.

140. Mínguez-Vega, G., et al., *Reconfigurable All-Diffractive Optical Filters Using Phase-Only Spatial Light Modulators.* Optics Letters, 2010. **35**(14): p. 2406-2408.

141. Obata, K., et al., *Multi-Focus Two-Photon Polymerization Technique Based on Individually Controlled Phase Modulation.* Optics Express, 2010. **18**(16): p. 17193-17200.

142. Mauclair, C., et al., *Dynamic Ultrafast Laser Spatial Tailoring for Parallel Micromachining of Photonic Devices in Transparent Materials.* Optics Express, 2009. **17**(5): p. 3531-3542.

143. Ji, N., et al., *High-Speed, Low-Photodamage Nonlinear Imaging Using Passive Pulse Splitters.* Nature Methods, 2008. **5**(2): p. 197-202.

144. Buist, et al., *Real Time Two-Photon Absorption Microscopy Using Multi Point Excitation.* Journal of Microscopy, 1998. **192**(2): p. 217-226.

145. Gerchberg, R. W., *A Practical Algorithm for the Determination of Phase from Image and Diffraction Plane Pictures.* Optik, 1972. **35**: p. 237.

146. Bulanov, S., et al., *Accelerating Monoenergetic Protons from Ultrathin Foils by Flat-Top Laser Pulses in the Directed-Coulomb-Explosion Regime.* Physical Review E, 2008. **78**(2): p. 026412.

147. Nolte, S., *Micromachining.* Optical engineering -New York- Marcel Dekker Incorporated, 2003. **80**: p. 359-394.

148. Martínez-Cuenca, R., et al., *Multibeam Second-Harmonic Generation by Spatiotemporal Shaping of Femtosecond Pulses.* Optics Letters, 2012. **37**(5): p. 957-959.

149. Amako, J., et al., *Chromatic-Distortion Compensation in Splitting and Focusing of Femtosecond Pulses by Use of a Pair of Diffractive Optical Elements.* Optics Letters, 2002. **27**(11): p. 969-971.

150. Li, G., et al., *Splitting of Femtosecond Laser Pulses by Using a Dammann Grating and Compensation Gratings.* Journal of the Optical Society of America A, 2005. **22**(4): p. 767-772.
151. Kuroiwa, Y., et al., *Arbitrary Micropatterning Method in Femtosecond Laser Microprocessing Using Diffractive Optical Elements.* Optics Express, 2004. **12**(9): p. 1908-1915.
152. Jesacher, A., et al., *Parallel Direct Laser Writing in Three Dimensions with Spatially Dependent Aberration Correction.* Optics Express, 2010. **18**(20): p. 21090-21099.
153. Hasegawa, S., et al., *Dynamic Control of Spatial Wavelength Dispersion in Holographic Femtosecond Laser Processing.* Optics Letters, 2014. **39**(3): p. 478-481.
154. Mínguez-Vega, G., et al., *Dispersion-Compensated Beam-Splitting of Femtosecond Light Pulses: Wave Optics Analysis.* Optics Express, 2007. **15**(2): p. 278-288.
155. Krausz, F., et al., *Extreme Nonlinear Optics: Exposing Matter to a Few Periods of Light.* Optics and Photonics News, 1998. **9**(7): p. 46-51.
156. Gerstner, E., *Laser Physics: Extreme Light.* Nature, 2007. **446**(7131): p. 16-18.
157. Cerullo, G., et al., *Ultrafast Optical Parametric Amplifiers.* Review of Scientific Instruments, 2003. **74**(1): p. 1-18.
158. Klimov, V. I., et al., *Femtosecond High-Sensitivity, Chirp-Free Transient Absorption Spectroscopy Using Kilohertz Lasers.* Optics Letters, 1998. **23**(4): p. 277-279.
159. Kasparian, J., et al., *White-Light Filaments for Atmospheric Analysis.* Science, 2003. **301**(5629): p. 61-64.
160. Diels, J.-C., et al., *Lightning Control with Lasers.* Scientific American, 1997. **277**: p. 50-55.
161. Stelmaszczyk, K., et al., *Long-Distance Remote Laser-Induced Breakdown Spectroscopy Using Filamentation in Air.* Applied Physics Letters, 2004. **85**(18): p. 3977-3979.
162. Couairon, A., et al., *Femtosecond Filamentation in Transparent Media.* Physics Reports, 2007. **441**(2–4): p. 47-189.
163. Romero, C., et al., *Non-Collinear Sum-Frequency Generation of Femtosecond Pulses in a Micro-Structured β-Bab2o4 Crystal.* Optics Express, 2008. **16**(22): p. 18109-18117.
164. Borrego-Varillas, R., et al., *Femtosecond Filamentation in Sapphire with Diffractive Lenses.* Journal of the Optical Society of America B, 2013. **30**(8): p. 2059-2065.
165. Yu, J., et al., *Three-Dimensional Dammann Array.* Applied Optics, 2012. **51**(10): p. 1619-1630.

166. Davis, J. A., et al., *Creating Three-Dimensional Lattice Patterns Using Programmable Dammann Gratings.* Applied Optics, 2011. **50**(20): p. 3653-3657.
167. Zhou, C., et al., *Numerical Study of Dammann Array Illuminators.* Applied Optics, 1995. **34**(26): p. 5961-5969.
168. Huot, N., et al., *Analysis of the Effects of Spherical Aberration on Ultrafast Laser-Induced Refractive Index Variation in Glass.* Optics Express, 2007. **15**(19): p. 12395-12408.
169. O'Shea, D. C., *Reduction of the Zero-Order Intensity in Binary Dammann Gratings.* Applied Optics, 1995. **34**(28): p. 6533-6537.
170. Cook, K., et al., *Coherent Array of White-Light Continuum Filaments Produced by Diffractive Microlenses.* Applied Physics Letters, 2005. **86**(2): p. 021105.
171. Kandidov, V., et al., *Towards a Control of Multiple Filamentation by Spatial Regularization of a High-Power Femtosecond Laser Pulse.* Applied Physics B, 2005. **80**(2): p. 267-275.
172. Liu, J., et al., *Ultrafast Control of Multiple Filamentation by Ultrafast Laser Pulses.* Applied Physics Letters, 2005. **87**(16): p. 161105.
173. Ni, X., et al., *Fresnel Diffraction Supercontinuum Generation.* Selected Topics in Quantum Electronics, IEEE Journal of, 2004. **10**(5): p. 1229-1232.
174. Mínguez-Vega, G., et al., *Wavelength Tuning of Femtosecond Pulses Generated in Nonlinear Crystals by Using Diffractive Lenses.* Optics Letters, 2010. **35**(21): p. 3694-3696.
175. Born, M., et al., *Principles of Optics: Electromagnetic Theory of Propagation, Interference and Diffraction of Light*. 1999: CUP Archive.
176. *Holoeye Photonics Ag, Specification Sheet Pluto - 0,7" Hdtv Lcos Phase Only Kit.*

Publications

[I]

Free-motion beam propagation factor measurement by means of a liquid crystal spatial light modulator.

Journal of Display Technology, 8(9), 539-545. 2012

Free-Motion Beam Propagation Factor Measurement by Means of a Liquid Crystal Spatial Light Modulator

Jorge Pérez-Vizcaíno, Omel Mendoza-Yero, Raúl Martínez-Cuenca, Lluís Martínez-León, Enrique Tajahuerce, and Jesús Lancis, *Member, IEEE*

***Abstract*—In contrast to the mechanical scanning procedure described in the standard ISO/DIS 11146, the use of electronically tunable focal length lenses has proved its capability for the measurement of the laser beam propagation factor (M^2) without moving components. Here, we demonstrate a novel experimental implementation where we use a low-cost programmable liquid crystal spatial light modulator (SLM) for sequentially codifying a set of lenses with different focal lengths. The use of this kind of modulators introduces some benefits such as the possibility for high numerical aperture or local beam control of the phase of the lenses which allows for minimizing systematic errors originated by lens aberrations. The beamwidth, according to the second-order moment of the irradiance, is determined for each focal length by using a digital sensor at a fixed position with respect to the spatial light modulator. After fitting the measured data to the theoretical focusing behavior of a real laser beam, the beam propagation factor is obtained. We successfully validated the results in the laboratory where a full digital control of the measurement procedure without mechanical scanning was demonstrated.**

***Index Terms*—Beam propagation factor, laser, spatial light modulators (SLMs).**

I. Introduction

FIFTY YEARS after the invention of the laser, this light source plays a major role in several areas of current importance such as optical communications, health care and industrial applications. Most of the above applications require a detailed characterization of the laser beam profile. A monochromatic Gaussian laser beam (TEM_{00}) is defined through the propagation direction, the peak amplitude, the waist location and one additional parameter (the Rayleigh range z_R,the waist radius σ_ω or the beam divergence θ) [1]. For real lasers, the so-called M^2 propagation factor provides a measurement of the deviation of the beam with respect to that of a TEM_{00} Gaussian beam due to contributions from higher order transverse modes, truncation or other distortions introduced by lenses, apertures, or other optic systems. The determination of the beam propagation factor is crucial for both scientific and industrial fields. As a matter of fact, the efficiency of multi-photon processes originated through tight focusing of laser beams depends on the powers of the irradiance distribution, so having a small M^2 means having a better product yield. Also, in the industry field, the measurement of M^2 is meaningful for applications such as hole drilling where a beam with a M^2 factor of two will produce a hole twice bigger than the expected for a TEM_{00} Gaussian beam.

The ISO standard (ISO/DIS 11146) provides a convenient method for M^2 measurement. In this technique, the laser beam to be evaluated is relayed through a lens in a fixed position and multiple beamwidth measurements are made along the waist region behind the lens [2]. Finally the beam propagation factor is obtained through the fitting of the experimental data. The beam width is measured in agreement with the second-order moment criterion. This method involves mechanical scanning of the intensity sensor along the beam propagation direction. In practical terms, this requires a high degree of alignment and parallelism. Also, the measurement is time-consuming (of the order of tens of seconds) and thus, sensible, to environmental fluctuations and beam changes.

Fast and easily applicable methods are needed for practical use due to ever more stringent requirements regarding the quality of laser beams. Very recently, faster and free-motion methods have been proposed. Among them, we mention those based on the use of a Shack–Hartmann wavefront sensor that provides unprecedented temporal resolution (up to 10 kHz) [3], [4] and those based on simultaneous capture of the waist at several Rayleigh ranges allowing the instantaneous fit of the M^2 curve at video rate [5]. On the other hand, it has also been proposed the idea of measuring the M^2 beam parameter using an electronically controlled variable focus lens [6]–[8]. To the best of our knowledge, up to present, all of the experimental implementations are limited to a variable-focus electrowetting-driven liquid lens in conjunction with an all-digital micromirror device [6]–[8]. In contrast to conventional focusing systems, such lenses suffer from a relatively low pupil diameter, and subsequent short focal length, which in some circumstances prevents its applicability in practical laser environments [9]. More interestingly, some voltage-dependent beam aberrations (particularly spherical, comma, and chromatic aberrations) are intrinsic to varioptic liquid lenses that, in this way, introduce some amount of systematic error in M^2 measurement [10]. More interestingly, conventional liquid lenses suffer from a strong astigmatism, distortion or light scattering during focus change that need to be corrected for by using sophisticated electrode design.

In this paper, following the idea originally proposed by the Riza group in [6], electronically controlled variable focal length

---

Manuscript received March 09, 2012; revised April 05, 2012; accepted April 16, 2012. Date of publication June 26, 2012; date of current version August 03, 2012. This work was supported by the Dirección General de Investigación Científica y Técnica, Spain, under Project FIS2004-02404 and FEDER, by . the Generalitat Valenciana under Grant GV05/110, by the Ministerio de Ciencia e Innovación, Spain, under Project FIS2010–15746 and FEDER, and by the agreement between Universitat Jaume I and Fundación Caixa Castelló under Project P1-1B2009-36.

The authors are with GROC, Institute of New Imaging Technologies, Universitat Jaume I, 12071-Castelló, Spain, and also with the Departament de Ciències Experimentals, Universitat Jaume I, 12080 Castelló, Spain (e-mail: jvizcain@fca.uji.es; omendoza@uji.es; rcuenca@fca.uji.es; lluis.martinez@uji.es; enrique.tajahuerce@uji.es; lancis@fca.uji.es).

Color versions of one or more of the figures are available online at http://ieeexplore.ieee.org.

Digital Object Identifier 10.1109/JDT.2012.2200453

lenses are codified onto a phase-only liquid crystal spatial light modulators (SLMs) for beam parameter measurement. In our method, a set of lenses with different focal lengths is codified onto the SLM by quadratic phase modulation and the diffracted beam width, according to the second order moment of the irradiance distribution, is determined for each focal length by using a charge-coupled device (CCD) at a fixed position. The use of this kind of modulators introduces some benefits such as the possibility for a bigger numerical aperture or local beam control of the phase of the lenses which allows for minimizing systematic errors originated by the lens aberrations in the standard procedure. Yet, our technique also opens the possibility of real-time fine-tuning of laser beams through the programmable nature of phase-only SLMs.

Liquid-crystal displays (LCDs) working as electronically addressed SLMs have been widely used to generate programmable diffractive lenses [11] and the mathematical models to encode the lens function in a device constrained by its pixilated structure and phase quantization analyzed [12]. In this paper, we also carry out the analysis of the artifacts (such as multiple focal lengths and higher order diffractions) due to the pixilated and the quantized nature of the lenses codified onto the SLM in beam propagation factor measurements. This analysis is carried out by means of a computer simulation. Finally, SLMs permit programmable lenses working under broadband or white-light illumination that allow to extend the proposed technique for different wavelength ranges without the need of previous calibration [13], [14]. Apart from lens codification, the use of phase-only SLMs in different tasks for optical information processing and adaptive optics has been extensively reported since the 90ths with extensive success [15]–[17].

II. EXPERIMENTAL SETUP AND THEORY

A. Beam Characterization

Following the ISO standard (ISO11146), for a properly aligned astigmatic beam propagating along the z axis, the second-order spatial moments are used to describe the beam diameter and the orientation of the irradiance distribution at a given transverse plane. For instance, for the horizontal Cartesian coordinate x, we have for the rms width $\sigma_x^2(z) = \langle x^2\rangle_z - \langle x\rangle_z^2$, where

$$\langle x^n\rangle_z = \frac{1}{I_o}\int_{-\infty}^{+\infty} x^n |\psi(x,y,z)|^2\, dxdy \tag{1}$$

is the normalized nth-order moment of the beam intensity $|\psi(x,y,z)|^2$. In the above equation, I_o denotes the zeroth-order moment of the function $|\psi(x,y,z)|^2$. Likewise, an analogous definition holds for the vertical coordinate y. For a TEM_{00} Gaussian beam, the rms width propagates along the axial coordinate in accordance with the simple quadratic relationship

$$\sigma_x^2(z) = \sigma_{wx}^2\left[1+\left(\frac{z-z_{wx}}{z_{Rx}}\right)^2\right] \tag{2}$$

where σ_{wx} is the rms width at the waist plane $z = z_{wx}$ and $z_{Rx} = 4\pi\sigma_{wx}^2/\lambda$ is the Rayleigh range of the monochromatic beam of wavelength λ. Also, the second-order angular moments are the pendants of the second-order spatial moments in the far field of the beam giving the beam divergence

$$\theta_{\sigma x} = 4\lim_{z\to\infty}\frac{\sigma_x}{z}. \tag{3}$$

The M^2 propagation factor for a simple astigmatic beam is defined through the product of the beam waist width and the divergence at far field [1]

$$M_x^2 = \frac{\pi}{\lambda}\sigma_{wx}\theta_{\sigma_x} \tag{4}$$

$$M_y^2 = \frac{\pi}{\lambda}\sigma_{wy}\theta_{\sigma_y} \tag{5}$$

in horizontal and vertical directions, respectively. As is well known, the value of M^2 for a TEM_{00} Gaussian beam is 1. It is not possible to find a lower value of the beam propagation factor for actual realizable beams. The Rayleigh range is reduced accordingly as $z_{Rx} = 4\pi\sigma_{wx}^2/M_x^2\lambda$ [1]. This parameter accounts for the spreading of the beam width in accordance with (2) with a reduced Rayleigh range and provides a measure of the departure from the Gaussian behavior. Also, M^2 is invariant through propagation along ABCD optical systems. From a practical point of view, a beam, with a certain width showing lower M^2 value, will behave better for focalization (collimation) purposes in the sense that the minimum spot size (minimum beam divergence) for a given optical system will be smaller.

B. Beam Propagation in Lens-Like Media

For future interest, we enter into detail about beam transformation through a very simple ABCD system consisting of a single lens of focal length f and its propagation along free space (see Fig. 1 for notation). We are interested in how the changes in the focal length affect to beam parameters after the lens and how to express these changes in terms of the input beam parameters. By geometrical transformations, it is straightforward to obtain the formulas that relate the parameters of the incident beam to those of the beam that emerges from the lens (with "s" subscript) [1], [18]. In this way, we find both the horizontal and the vertical directions

$$z_{ws} = f - \beta(z_w + f) \tag{6}$$

$$\sigma_{ws}^2 = \beta\sigma_w^2 \tag{7}$$

and

$$z_{Rs} = \beta z_R \tag{8}$$

where the magnification parameter β is defined as

$$\beta = \left(1+\frac{2z_w}{f}+\frac{z_w^2+z_R^2}{f^2}\right)^{-1}. \tag{9}$$

By taking into account (2), (7), and (8), we find the following propagation law for the squared rms width at any transversal plane located at a distance z behind the lens [18]:

$$\sigma_s^2(z) = \frac{M^2\lambda}{4\pi z_R}\left[z_w^2+z_R^2+z^2-2zz_w + 2\frac{z^2z_w - z\left(z_w^2+z_R^2\right)}{f} + \frac{z^2\left(z_w^2+z_R^2\right)}{f^2}\right]. \tag{10}$$

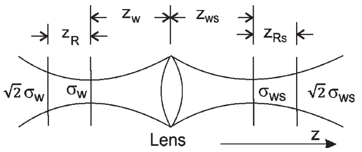

Fig. 1. Beam transformation by a thin lens. Z_{ws} and Z_w are measured from the lens to the waist of the beam before the lens and behind the lens. $Z_{ws} > 0$ for Z_{ws} behind the lens and $Z_w > 0$ for Z_w located before the lens.

which holds for both the horizontal and the vertical directions. Equation (10) can be recognized as a simple algebraic expression in terms of the focal length of the SLM

$$\sigma_s^2 = a + \frac{b}{f} + \frac{c}{f^2} \tag{11}$$

where the fitting parameters can be easily related to the actual beam parameters of the incident beam through

$$M^2 = \frac{4\pi}{\lambda z^2}\sqrt{ac - \frac{b^2}{4}} \tag{12}$$

$$z_w = \frac{\frac{c}{z} + \frac{b}{2}}{a + \frac{1}{z}\left(\frac{c}{z} + b\right)} \tag{13}$$

and

$$z_R^2 = \frac{c}{a + \frac{1}{z}\left(\frac{c}{z} + b\right)} - \left[\frac{\frac{c}{z} + \frac{b}{2}}{a + \frac{1}{z}\left(\frac{c}{z} + b\right)}\right]^2. \tag{14}$$

Equation (11) states that by transforming the beam with several spherical lenses of different focal length, the input beam parameters can be determined from a least squares fit, in accordance with (12)–(14), if we evaluate the corresponding rms width for each beam profile by using a digital camera at a fixed axial location. This is the underlying idea of our free-motion full digital technique for beam propagation measurement.

III. SLM CALIBRATION

In our approach, a set of lenses with tunable focal length is codified sequentially into a phase-only liquid crystal SLM. A variable quadratic-phase factor in the spatial domain displayed on the SLM plays the role of the programmable lens. Whenever the focal length is changed, a different axial plane is imaged onto the beam profiler, which is kept at a fixed position (see Fig. 2). In this way, a complete digital control of the measurement system is attained without the need of any moving component as a main difference with the ISO standard procedure.

We used a reflective liquid crystal on silicon (LCoS) SLM, *Holoeye Pluto*, with a panel size of 0.7”, 1920×1080 pixels, a fill factor of 87% and a pixel pitch of 8 μm. This device achieves a phase modulation exceeding 2π rad for the working wavelength in the visible region and near IR. The SLM is based on a nematic-electronic controlled birefringence mode, in which the liquid crystal molecules are initially parallel to the electrodes but tend to tilt following the direction of the applied electric field. The amplitude and polarization modulations are assumed to be negligible. Pixels are individually addressed by sending gray-level images to the modulator. Thus, every gray-level g corresponds to a given phase shift. The display has an 8-bit controller that provides 256 different values of g. The operation curve of the modulator shows in general a non-linear behavior, so a careful calibration is required.

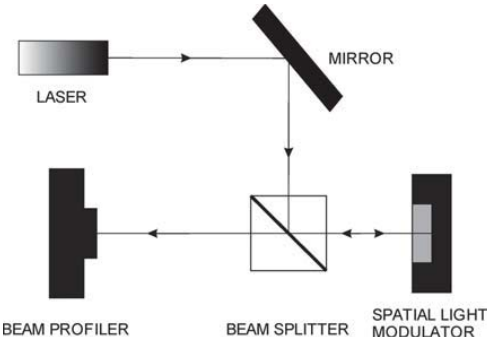

Fig. 2. Schematic of the optical device.

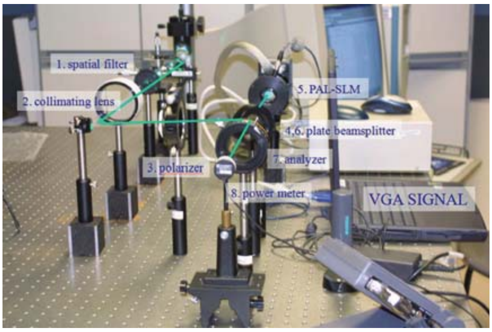

Fig. 3. Polarimetric setup for SLM calibration.

The SLM has been characterized in detail in our laboratory. We calibrated the SLM for the operating wavelength of the laser beam at 633 nm through the measurement of the intensity modulation in a polarimetric setup (Fig. 3) as a function of the addressing gray level. The input linear polarization was set at 45° relative to the axis in which liquid crystal molecules are aligned. The analyzer was set at the same orientation as the input polarization. This configuration is termed as the “intensity modulation mode” as phase variations are converted onto intensity fluctuations for calibration purposes [19], [20]. Different gray-level images are sent to the SLM and the optical transmittance defined as the ratio between the output and the input light intensity is found to be

$$T(g) = \frac{1}{2}\cos(\phi) \tag{15}$$

where ϕ is the phase shift. In this way, the calibration curve $\phi = f(g)$ is theoretically expressed through

$$\phi = \cos^{-1}\left[2T(g)\right]. \tag{16}$$

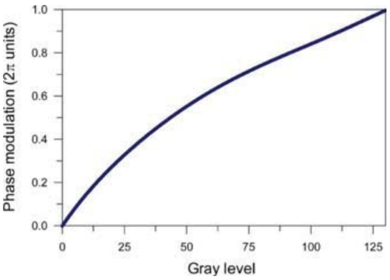

Fig. 4. Phase modulation versus gray level. It is not necessary to use the full 256 gray level scale to achieve a 2π phase modulation.

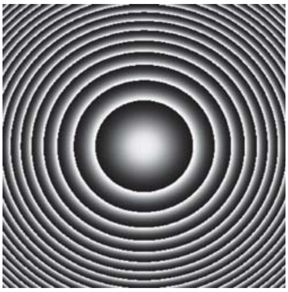

Fig. 5. Phase map corresponding to a diffractive lens. The fringes are concentric rings with increasing phase from 0 to 2π. Fringes width decrease with distance to the center what can produce aliasing.

Fig. 4 shows the calibration curve for 633 nm, in which a limited range of gray level chosen from a convenient interval among the $[0, 255]$ scale is needed to get the required 2π phase modulation.

From a practical point of view, energy limitations arise from the use of the SLM. Although a neutral density filter can be used to attenuate the laser intensity, it is convenient to recall that the laser beam power incident onto the SLM should remain under the damage threshold of the display. For the case of continuous wave laser operation, this quantity is in the order of several $\mathrm{W/cm^2}$ for a laser wavelength in the visible region of the spectrum and near IR. It should be noted that this quantity quickly decreases for UV radiation that prevents the technique to operate at this spectral region.

IV. ANALYSIS OF THE LENS CODIFICATION ONTO THE SLM

With the previous result we sent to the modulator the gray levels corresponding to the quadratic phase imparted by a lens of focal length f; i.e, $\phi(r) = kr^2/2f$, with k the wave number and r the radial coordinate onto the SLM pupil. In practice, the SLM displays the phase wrapped in 2π steps [14] (see Fig. 5). Note that this wrapping may lead to aliasing in the outer regions of the lens since the width of each wrapped zone decreases with the distance to the center. A detailed mathematical model that describes the behavior of lenses encoded in a low-resolution device can be found in [12]. In short, Carcolé *et al.* demonstrated the existence of an optimum focal length for best lens performance in terms of the FWHM focal distribution for a given codification device. The point is to define blocks of pixels that always contribute constructively to the focal intensity. For current pixel size in the μm range, the FWHM spreading at the focal plane is remarkably low for focal lengths extending from a few millimeters to several centimeters. In a simplified model, the focal length of the codified lens consisting of several Fresnel zones is directly related to the outermost zone width, Δr, and the lens diameter, d, through $f = d\Delta r/\lambda$. In practice, the outermost zone must be displayed with at least two pixels to avoid aliasing, so Δr actually equals the pixel size. In addition, the lens diameter should be adjusted to several times the beam width over the SLM to avoid clipping of the laser beam. For our experiment, this leads to a minimum focal length of 25 mm. There is not a clear criterion to establish the maximum focal length that can be codified since it depends on the required lens efficiency. For the experiment the maximum focal length ($f \cong 80$ cm) is considered to provide accurate results. It is also worth mentioning that some care must be paid to block out light diffracted into the higher diffraction orders of the pixilated diffractive lens codified onto the SLM.

We conducted some computer simulations in order to evaluate the influence of pixilation and quantization of the SLM in beam propagation factor measurements. For the analysis, we considered a TEM_{00} Gaussian beam, with the generalization to more complex beam profiles automatic. The simulation was carried out in the following way. First, the beam rms width was analytically evaluated at the sensor plane assuming a non-pixilated, non-quantized lens profile. Afterwards, the effect of the sampled and quantized Fresnel lens onto the TEM_{00} Gaussian beam was simulated in the computer using the Fresnel transform as a valid diffraction model. The pixel size was chosen as a parameter. The number of pixels in the SLM (the lens pupil) was chosen to cover the full beam diameter so that no clipping artifacts were introduced. In this way, the rms width of the transformed beam was calculated using computer data for the simulated irradiance distribution at the sensor plane and the results compared to the analytical values. It is worthwhile to mention that in order to evaluate the simulated rms width, the irradiance distribution was clipped and zoomed around the central maxima of the diffractive orders generated by the pixilated structure of the SLM.

In our case only 130 number of grey levels are available which yield discrete phase values to encode the continuous quadratic phase function. To do this, as usual, we use the Eucledian projection to choose the quantization point that is closest in distance. Further, the effect of the nonlinear mapping between the grey level and the phase information has to be considered. In general, the quantization effect is to create an infinite number of ghost images located at different focus planes. Note, however, that ghost are less disturbing since they are non-overlapping. In our simulation all of the above effects have been taken into account.

For the simulation we chose a wavelength of 632 nm, a rms width of 0.25 mm at the SLM plane, a lens pupil of 4.8 mm, and the sensor plane was located 43.5 cm away from the SLM, which correspond to typical values for the optical implementation in the next section. The pixel size at the output plane was kept

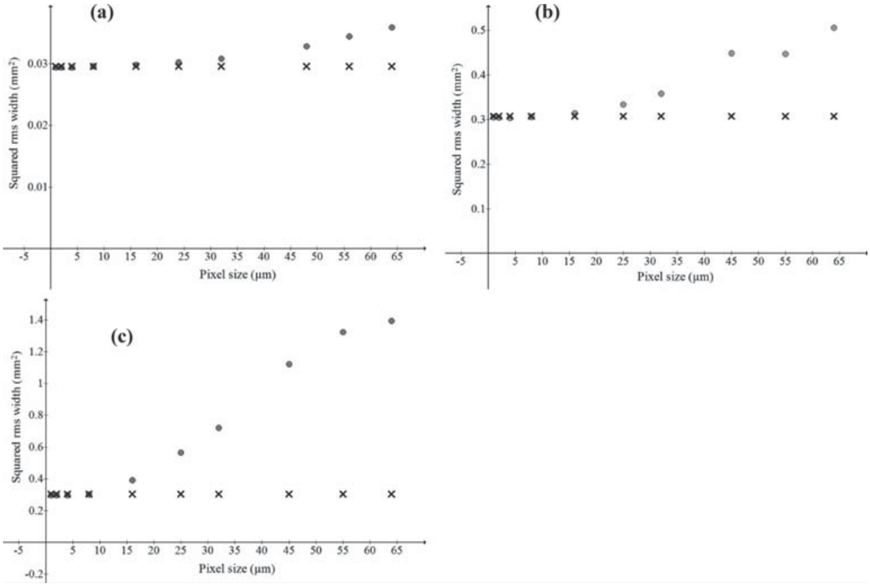

Fig. 6. Plot of the beam squared rms width at the sensor plane in terms of the pixel size of the SLM for a codified focal length of (a) 700 mm; (b) 150 mm; and (c) 100 mm. Analytical values are labelled with a cross, whereas simulated values are shown as a circle.

fixed to 8 μm which corresponds roughly to the pixel size of the CCD in the experimental section. Three different values for the focal length codified onto the SLM were considered which correspond to the extreme lenses of 100 and 700 mm and the intermediate value of 150 mm.

The results for the beam rms width at the sensor plane in terms of the pixel size of the SLM are shown in Fig. 6. Analytical values are labeled with a cross, whereas simulated values are shown as a circle. Also, we plot in Fig. 7 the irradiance distribution around the central maxima for the lens with focal length 100 mm and a pixel size of 1 μm and 64 μm. In all cases, a pixel size lower than 10 μm leads to an excellent agreement between simulated and analytical values, which confirm that sampling and quantization effects are negligible for a pixel sizes 25 times lower than the beam width. However, we report strong discrepancies for lenses codified onto low-resolution SLMs. These artifacts are more significant in the low focal length regime, even with relative errors as high as 400%. This fact makes it impossible the use of our technique in this regime.

In terms of the speed of operation, the system supports continuous signal acquisition for video rates up to 60 Hz which, in practical conditions, determines the bottleneck in terms of measurement speed for the beam propagation factor. From a spectral point of view, liquid crystal SLMs can be operated under broadband illumination although, for this case, severe chromatic aberrations coming from refractive index chromatism, the diffraction chromatism, and the quantization chromatism are expected [13], [14]. Although, for narrowband laser beams working at different spectral regions the SLM the system should be, in principle, recalibrated, even for this situation the chromatic compensation for a set of discrete wavelengths can alleviate the above matter [13], [14].

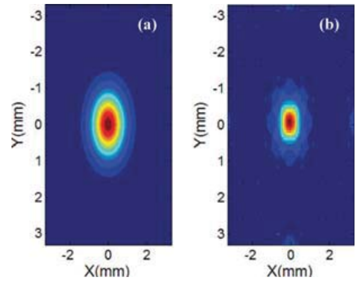

Fig. 7. Simulated irradiance distribution around the central maxima for a lens with focal length 100 mm codified onto an SLM with a pixel size of (a) 1 μm and (b) 64 μm. Note that the rms width corresponding to Fig. 7(b) is bigger than that of Fig. 7(a) due to the pedestal for the irradiance in Fig. 7(b) associated to the low resolution codification.

V. Experimental Results

According with the above procedure, we measured the beam propagation factor of a commercial He-Ne laser ($\lambda = 632$ nm, 20 mW) emitting a TEM_{00} mode with linear polarization as a coherent beam source and beam diameter of about 2 mm. It was characterized employing both the standard ISO approach and our procedure. In both cases, beam profiling was performed by means of a 14 bit digital charge-coupled device camera, 1360×1024 pixels, size 6.45 μm (WinCamD-UCD23)

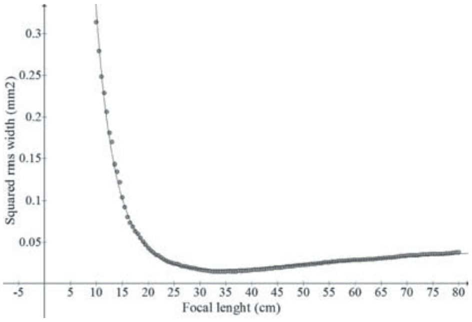

Fig. 8. Experimental results for x axis.

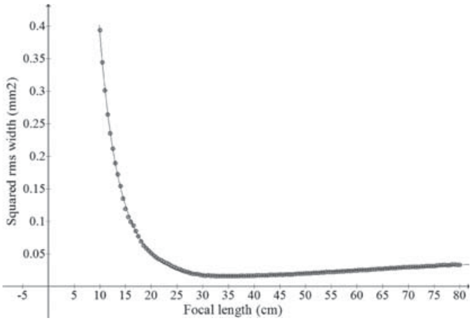

Fig. 9. Experimental results for y axis.

previously calibrated for the measurement of the laser beam parameters. Camera data processing was performed using commercial software. The data for the squared beam radius are plotted in Fig. 8 (x axis) and Fig. 9 (y axis) against the focal length displayed onto the SLM. The beam profiler was fixed at a distance of 43.5 cm from the SLM. We oversampled the focal length range between 10 and 80 cm with 140 sampling points. Focal lengths variations of a few millimeters generate focal distributions with a detectable focal depth in terms of the CCD pixel size. In Fig. 10, a picture of the focal distributions for two focal lengths differing in 5 mm is shown. Note that the ISO method only requires 10 measurement points along the axis of propagation (5 around the waist and (5 around the waist and 5 further than twice the Rayleigh range). A hyperbolic fit yields M^2 values of $1.12/1.15$ in horizontal/vertical direction, respectively. The effort for a complete measure (140 sampling points) lasted around 10 s. This time interval is shortened if the number of sampling points is reduced according to the ISO standard. Also, the measurement interval can be further reduced if the software control is implemented onto the graphic processing unit of the computer. The results for the beam propagation factor following the ISO approach were $1.07/1.08$ in horizontal/vertical directions after mechanical scanning of the beam profiler along the propagation direction. Thus a concordance level of less than 5% between both methods is found. Yet, the accuracy of both methods is comparable and mainly determined by beam profiling measurement accuracy. Using a 14-bit beam profiler, beams diameters are obtained with an accuracy better than 2% that translates to better than 4% in M^2 determination.

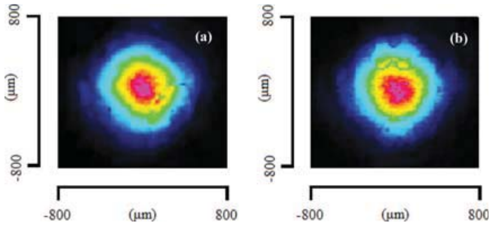

Fig. 10. Experimental irradiance distributions at the sensor plane when the codified focal lengths at the SLM are 22.5 cm (a) and 23 cm (b).

VI. CONCLUSION

To the best of our knowledge, we have experimentally validated the first beam propagation factor analyzer based on a liquid crystal SLM and a beam profiler using the idea of electronically controlled focal length lenses proposed originally by Riza *et al.* [6]. By using a digital sensor at a fixed position, we measure the beam width for each focal length that is codified onto the SLM. This analyzer provides full digital control, obtaining a compact and quick measurement method free from mechanical scanning. After fitting the measured data to the theoretical focusing behavior of a real laser beam, the beam propagation factor is obtained. The method has been experimentally performed in the laboratory and has demonstrated comparable performance to that of the ISO approach (within a concordance level of less than 5%) but free from artefacts associated to moving components.

REFERENCES

[1] B. E. A. Saleh and M. C. Teich, *Fundamentals of Photonics*, B. E. A. Saleh, Ed., 2nd ed. Hoboken, NJ: Wiley, 1989, pp. 79–87.

[2] "Test method for laser beam parameters: beam width, divergence angle and beam propagation factor," International Organization for Standardization, Doc. ISO/DIS 11146, 1996.

[3] B. Schäfer, M. Lübbecke, and K. Mann, "Hartmann-Shack wave front measurements for real time determination of laser beam propagation parameters," *Rev. Sci. Instrum.*, vol. 77, p. 053103, 2006.

[4] J. V. Sheldakova, A. V. Kudryashov, V. Y. Zavalova, and T. Y. Cherezova, "Beam quality measurements with Shack–Hartmann wavefront sensor and M2-sensor: Comparison of two methods," *Proc. SPIE*, vol. 4493, pp. 285–293, 2002.

[5] A. M. Cary, J. L. Guttman, R. Chirita, and D. W. Peterman, "Beam quality measurements with Shack-Hartmann wavefront sensor and M2-sensor: Comparison of two methods," in *Proc. SPIE*, 2008, vol. 6871, pp. 687103-1–687103-11.

[6] M. Sheikh and N. A. Riza, "Motion-free hybrid design laser beam propagation analyzer using a digital micromirror device and a variable focus liquid lens," *Appl. Opt.*, vol. 49, pp. D11–D16, 2010.

[7] M. Sheikh, P. J. Marraccini, and N. A. Riza, "Laser beam characterization using agile digital–analog photonics," in *Proc. SPIE*, 2010, vol. 7675, p. 767508.

[8] P. J. Marraccini and N. A. Riza, "Multimode laser beam characterization using agile digital-analog photonics," in *Proc. SPIE*, 2010, vol. 8026, p. 8026OE.

[9] S. Kuiper and B. H. W. Hendriks, "Variable-focus liquid lens for miniature cameras," *Appl. Phys. Lett.*, vol. 85, p. 1128, 2004.

[10] H. Ren and S. T. Wu, "Variable-focus liquid lens," *Opt. Express*, vol. 15, pp. 5931–5936, 2007.

[11] V. Laude, “Twisted-nematic liquid-crystal pixilated active lens,” *Opt. Commun.*, vol. 153, pp. 134–152, 1998.

[12] E. Carcolé, J. Campos, and S. Bosch, “Diffraction theory of Fresnel lenses encoded in low-resolution devices,” *App. Opt.*, vol. 33, pp. 162–174, 1994.

[13] A. Márquez, C. Iemmi, J. Campos, and M. J. Yzuel, “Achromatic diffractive lens written onto a liquid crystal display,” *Opt. Lett.*, vol. 31, pp. 392–392, 2006.

[14] M. S. Millán, J. Otón, and E. Pérez-Cabre, “Dynamic compensation of chromatic aberration in a programmable diffractive lens,” *Opt. Express*, vol. 14, pp. 6226–6242, 2006.

[15] J. L. Martinez, I. Moreno, and E. Ahouzi, “Diffraction and signal processing with a liquid crystal microdisplay,” *Eur. J. Phys.*, vol. 27, pp. 1221–1231, 2006.

[16] C. Maurer, A. Jesacher, S. Bernet, and M. Ritsch-Marte, “What spatial light modulators can do for optical microscopy,” *Laser Photon. Rev.*, vol. 5, pp. 81–101, 2011.

[17] J. Arines, V. Durán, Z. Jaroszewicz, J. Ares, E. Tajahuerce, P. Prado, J. Lancis, S. Bara, and V. Climent, “Measurement and compensation of optical aberrations using a single spatial light modulator,” *Opt. Express*, vol. 15, pp. 15287–15292, 2007.

[18] L. Martí-López, O. Mendoza-Yero, and J. A. Ramos-de-Campos, “Propagation of polychromatic Gaussian beams through thin lenses,” *J. Opt. Soc. Amer. A*, vol. 18, pp. 1348–1356, 2001.

[19] F. Li, N. Mukohzaka, N. Yoshida, Y. Igasaki, H. Toyoda, T. Inoue, Y. Kobayashi, and T. Hara, “Phase modulation characteristics analysis of optically-addressed parallel-aligned nematic liquid crystal phase-only spatial light modulator combined with a liquid crystal display,” *Opt. Rev.*, vol. 5, pp. 174–178, 1998.

[20] L. Martínez-León, P. Clemente, E. Tajahuerce, G. Mínguez-Vega, O. Mendoza-Yero, M. Fernández-Alonso, J. Lancis, V. Climent, and P. Andrés, “Spatial-chirp compensation in dynamical holograms reconstructed with ultrafast lasers,” *Appl. Phys. Lett.*, vol. 94, p. 011104, 2009.

Jorge Pérez-Vizcaíno, photograph and biography not available at time of publication.

Omel Mendoza-Yero, photograph and biography not available at time of publication.

Raúl Martínez-Cuenca, photograph and biography not available at time of publication.

Lluís Martínez-León, photograph and biography not available at time of publication.

Enrique Tajahuerce, photograph and biography not available at time of publication.

Jesús Lancis (S’88–M’89) was born in San Miguel de Salinas, Alicante, Spain, in 1965. He received the B.S. and Ph.D. degrees in physics from the Universitat de València, Spain, in 1988 and 1992, respectively.

Since 1991, he has been with the *Grup de Recerca d’Òptica de Castelló,* Physics Department, Universitat Jaume I, Castellon, Spain. He has been a visiting scientist at both the University of North Carolina at Charlotte, and with the University of Minnesota, Minneapolis, where he worked in the field of diffractive optics. His current research interest include short pulse generation, pulse shaping, microwave photonics, femtosecond optics, liquid crystal displays, ophtalmic optics, and entangled photons. He is both author and co-author of more than 100 papers in leading optics journals.

Dr. Lancis is a member of Spanish Optical Soceity and the Optical Society of America.

[II]

Programmable quasi-direct space-to-time pulse shaper with active wavefront correction.

Optics Letters, 37(24), 5067-5069. 2012

Programmable quasi-direct space-to-time pulse shaper with active wavefront correction

Omel Mendoza-Yero,[1,*] Vincent Loriot,[2,3] Jorge Pérez-Vizcaíno,[1] Gladys Mínguez-Vega,[1]
Jesús Lancis,[1] Rebeca de Nalda,[2] and Luis Bañares[3]
[1]*Institut de Noves Tecnologies de la Imatge (INIT), Universitat Jaume I, Castelló E 12080, Spain*
[2]*Instituto de Química Física Rocasolano, Consejo Superior de Investigaciones Científicas, Madrid 28006, Spain*
[3]*Facultad de Ciencias Químicas, Universidad Complutense de Madrid, Madrid 28040, Spain*
**Corresponding author: omendoza@fca.uji.es*

Received October 18, 2012; revised November 8, 2012; accepted November 8, 2012;
posted November 9, 2012 (Doc. ID 178289); published December 5, 2012

We experimentally demonstrate an extremely compact and programmable pulse shaper composed of a single phase mask encoded into a spatial light modulator. Its principle of operation is similar to the previously theoretically introduced quasi-direct space-to-time pulse shaper [Opt. Express **16**, 16993 (2008)], which is based on diffractive optics. The proposed pulse shaper exhibits not only real-time temporal modulation, but also high-efficiency output pulses thanks to an active correction of the wavefront aberrations. © 2012 Optical Society of America

OCIS codes: 320.5540, 050.1970, 220.1000.

Today, femtosecond pulse shaping is a widespread technology. User-defined temporal waveforms with control of phase, amplitude, and polarization are required in many applications, such as high-field laser–matter interactions, photonic processing of telecom signals, and nonlinear microscopy. Pulse shaping is usually performed through a space-to-time transformation, where spatial masking of an optical beam causes its temporal modulation. In the Fourier-transform pulse shaping technique, the complex mask is placed at the Fourier plane of a zero-dispersion grating device where the optical frequency spectrum is spatially dispersed [1].

In a different approach, if a spatial mask is placed in the input plane of a generalized spectrometer, a direct (for a diffractive grating) or quasi-direct [for a diffractive lens (DL)] space-to-time mapping of the input spatial mask into the output temporal waveform is obtained. The advantages of these approaches are the compactness of the setups and the saving of time, as the Fourier-transform computation of the spatial patterns is not needed. In this context, the direct space-to-time (DST) [2] and the quasi-direct space-to-time (QDST) [3,4] pulse shapers have demonstrated their utility for high-repetition-rate wavelength-division-multiplexed systems [5], the generation of millimeter waves [6], the generation of fractal light pulses [7], and the study of molecular alignment [8], and also in the spectral domain to obtain bandpass optical filters [9,10].

Compact, dynamic, user-friendly, and fast-operation devices demanded by nonexpert pulse-shaper users have inspired researchers to look for simple and compact designs. In this context, DST pulse shapers have been recently reduced to a phase-only spatial light modulator (SLM) together with a refractive lens to create a very innovative device [11]. However, high-power Ti:sapphire laser systems suffer from wavefront aberrations due to imperfections in the optical components, and pump-induced thermal distortions in the amplifiers. Although thermal distortions can be reduced by cooling the Ti:sapphire crystal, an accurate correction of wavefront aberrations needs a more versatile approach usually based on adaptive optics [12,13].

In this Letter, we show that the QDST pulse shaper can be reduced to a simple phase mask. As far as we know, this is the first proposal of a single diffractive element pulse shaper. In this proposal the entire size of the pulse shaper is very small; there is almost no need for optical alignment, and obviously no extra refractive focusing element is required. From an experimental point of view, the above-mentioned phase mask is implemented into a phase-only SLM, exhibiting in this way an additional advantage, its programmable performance. Furthermore, we demonstrate that an appropriate correction of the wavefront aberrations improves the pulse features at the output plane of the shaper. At this point, by using experimental data collected with a commercial Shark–Hartmman wavefront sensor (WS), the aberrations were mostly corrected with the SLM. In the present implementation of the QDST pulse shaper, both the corresponding phase mask and the wavefront correction were accomplished with the same device, the SLM. In order to measure the temporal response of the shaper, an intensity cross correlation [14], with a nonlinear crystal, between the shaped and the reference ultrashort light pulse has been carried out.

In Fig. 1 a schematic diagram of the optical setup is shown. For the experiment we use a Ti:sapphire

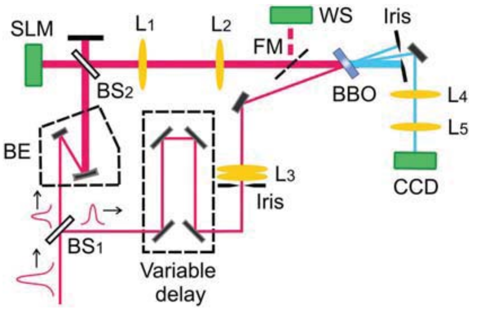

Fig. 1. (Color online) Schematic of the intensity cross-correlation setup to measure the temporal profile of light pulses.

femtosecond laser that emits pulses of about 30 fs intensity FWHM at 1 kHz of repetition rate, centered at $\lambda_0 = 800$ nm with 40 nm of spectral bandwidth. At the entrance of the interferometer, the light coming from the ultrashort laser source is split with a pellicle beam splitter (BS_1) into two pulses: the reference pulse and the shaped pulse. The reference pulse is a replica of the initial ultrashort pulse, whereas the shaped pulse has the desired temporal profile. The latter is first expanded via 4× all-mirror beam expander (BE) and sent, using a second beam splitter (BS_2), to the phase-only SLM (1920×1080 pixel resolution, and 8 μm pixel pitch), where the phase mask of the QDST pulse shaper is encoded.

In previous versions [3,8], the QDST pulse shaper was composed of two separate elements: a DL and a complex mask facing each other. To construct a single phase mask, both the complex mask transmittance and the DL must be encoded onto the phase-only SLM. The complex mask transmittance is written as $|t(r)| \exp(i\varphi_M)$, where $|t(r)|$ is the amplitude and φ_M is the phase of the function. To do that, we follow a procedure reported in [15]. That is, for each pixel of the SLM, the encoded phase mask is obtained by multiplying the amplitude of the complex mask by the phase of the DL. Thus, the phase transmission function of the phase-only SLM is $T(r) = \exp[i|t(r)|(\varphi_M + \Phi_{\mathrm{DL}})]$, where $\Phi_{\mathrm{DL}} = \pi r^2/(\lambda_0 Z_0)$ is the phase introduced by the DL, and Z_0 denotes its focal length for λ_0. The amplitude of the complex mask transmittance must be defined within the range [0, 1], whereas the total phase between $[-\pi, \pi]$. From the previous procedure it is apparent that as the depth of the phase distribution changes with $|t(r)|$, the diffraction efficiency of the phase mask is spatially modified.

The output of the QDST pulse shaper is located at the plane $z = Z_0$, in the close vicinity (by few micrometers) of the focal spot of the DL. In our optical setup, the plane $z = Z_0$ was imaged onto the plane of the nonlinear crystal with the help of a telescope composed of two lenses (L_1 and L_2) of equal focal length (200 mm). The temporal amplitude of the shaped pulse is approximately given by the convolution of the initial ultrashort pulse with the transmittance of the complex mask in r^2, previously transformed into the time domain by the conversion constant $\beta = 1/(2cZ_0)$, where c is the velocity of light in vacuum [3]. Furthermore, the temporal window of the shaper Λ is assessed by the expression $\Lambda = r_0^2\beta$, $r_0 = 4.3$ mm being the radial extension of the phase mask.

The shaped and reference pulses are spatially and temporally overlapped into a β-$\mathrm{BaB_2O_4}$ (BBO) type I crystal of 70 μm thickness. In our case, the crystal is thin enough to ensure a phase-matching process without loss of spectral components. The reference pulse is focused by means of a pair of refractive lenses (L_3), with an equivalent focal length of 250 mm. Since the length of bulk material is approximately the same in both arms, the effects of group-velocity dispersion were pre-compensated with a prism pair at the postcompression stage of the laser.

The delay line shown in Fig. 1 allows us to vary the path length of the reference pulse. By recording the intensity of the central second-harmonic (SH) signal for each position of the delay line, the approximated intensity profile (temporally stretched by the convolution with the reference pulse) of the shaped pulse is determined. In order to select the SH signal generated only in the close vicinity of the DL focus, we formed a 2× magnified image of the BBO crystal plane onto a CCD camera with a telescope composed of lenses L_4 and L_5 of focal lengths 100 and 200 mm, respectively.

In practice, the above measurements are affected by wavefront aberrations. That is, while moving the delay line to temporally scan the shaped pulse with respect to the reference one, the wavefront aberrations deteriorate the irradiance distribution at the BBO crystal plane. Here, the propagation time difference (PTD) among pulses coming from the cross section of the DL describes the temporal overlapping process in the BBO crystal. For each position of the delay line, the irradiance distribution at the BBO crystal plane is determined by the coherent interference of pulses diffracted from ring zones of the DL, with the reference pulse. These zones of equal area correspond to geometrical rings of the DL from which the PTD of diffracted pulses is equal to (or less than) the temporal pulse width of the reference pulse. The larger and thinner the rings, the smaller the focal spot size of the DL, and consequently the effects of wavefront aberrations become more and more critical.

In Fig. 2(a) we show the spatial shape of the central SH signal in the case of the outermost ring zone of the DL (achieved at the corresponding position of the delay line). From Fig. 2(a) it is clear that the expected Bessel-like pattern is completely lost because of the presence of aberrations. The above point was confirmed with an active correction of the wavefront aberrations at the BBO crystal plane; see Fig. 2(b).

For this purpose, we deviated the shaped pulse before the BBO crystal using a flip mirror (FM) (see Fig. 1), and sent it toward a commercial Shark–Harmman WS, where the spatial phase φ_{SP} at the SLM plane was measured. Hence, the phase transmission function of the phase-only SLM is finally rewritten in the form $T(r) = \exp[i|t(r)|(\varphi_M + \Phi_{\mathrm{DL}} - \varphi_{\mathrm{SP}})]$. In this way, the SLM is not only used to encode the QDST phase mask, but also to correct for wavefront distortions. The comparison between Figs. 2(a) and 2(b) allows us to see the improvement of the focal distribution after wavefront correction.

The finite number of pixels of the SLM causes the efficiency of the encoded DLs to depend on the radial coordinate. This unwanted effect originates a modulation in the temporal response of the QDST pulse shaper,

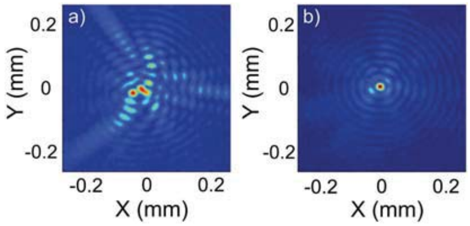

Fig. 2. (Color online) SH irradiance patterns at the BBO crystal plane for the outermost ring zone of the DL, without (a) and with (b) wavefront correction.

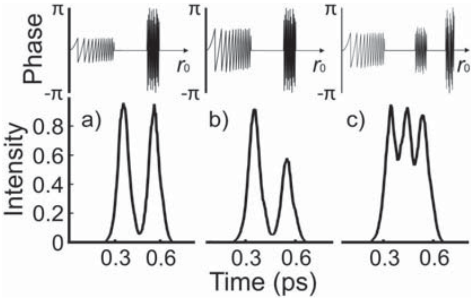

Fig. 3. Intensity cross-correlation measurements of temporal profiles synthesized by the QDST pulse shaper (bottom). Example of a radial phase profile of corresponding masks (top).

decreasing the peak intensity of the shaped pulses coming from the outer zones of the encoded DL. For longer focal lengths the above-mentioned dependence can be turned off, but unfortunately in these cases the temporal window of the QDST pulse shaper is also reduced. In particular, we encode a DL with focal length of 135 mm, which corresponds to a temporal window of about 230 fs. In this case, the phase of the outermost ring of the DL is encoded with only two phase levels. This reduces the focalization efficiency to about 40% [16]. Therefore, to guarantee a constant response over the whole temporal window of the QDST pulse shaper the amplitude of the complex mask should change radially to compensate for the mentioned efficiency loss (see mask profiles at top part of Fig. 3)

In Fig. 3, three different examples of temporal profiles obtained with the QDST pulse shaper are shown. The first case [see Fig. 3(a)] is a sequence of two pulses of equal peak intensity, delayed 200 fs between them. The temporal width of the shaped pulses, considering their convolution with the reference pulse, is about 80 fs intensity FWHM. The second example shown in Fig. 3(b) corresponds to the same temporal profile, but different relative peak intensity between pulses. Finally, the third case is a sequence of three pulses with slowly decreasing peak intensity; see Fig. 3(c). For examples shown in Figs. 3(a)–3(c), the theoretical overall diffraction efficiencies are 2.70%, 2.48%, and 2.67%, respectively. Notice that the limited spatial size of the SLM and the temporal width of the initial ultrashort pulse establish the maximum number of pulses that can be synthesized within the available temporal window; see Fig. 3(c).

For certain applications, an array of phase masks can also be possible, giving the extra possibility of parallel spatiotemporal and dynamical processing. In all applications, before implementing the QDST pulse shaper, particular attention should be paid to the adequate correction of the wavefront aberrations. The temporal window of the programmable QDST pulse shaper could be also increased in the near future when technological advances allow for SLM with larger working area as well as smaller pixel pitch. This is not the case for static phase masks, where the available techniques (e.g., photolithography) can achieve several centimeters for the mask size while keeping high spatial resolution.

This research was funded by the Spanish Ministerio de Ciencia e Innovación and the Generalitat Valenciana through Consolider Programme (SAUUL CSD2007-00013), and Prometeo Excellence Programme (PROMETEO/2012/021), and projects FIS2010-15746, P11B2010-26, and CTQ2008-02578. We also thank the European network ITN FASTQUAST (PITN-GA-2008-214962). Authors are also very grateful to the SCIC of the Universitat Jaume I for the use of the femtosecond laser.

References

1. A. M. Weiner, Opt. Commun. **284**, 3669 (2011).
2. D. E. Leaird and A. M. Weiner, Opt. Lett. **24**, 853 (1999).
3. G. Mínguez-Vega, O. Mendoza-Yero, J. Lancis, R. Gisbert, and P. Andrés, Opt. Express **16**, 16993 (2008).
4. V. Loriot, O. Mendoza-Yero, G. Mínguez-Vega, L. Bañares, and R. de Nalda, IEEE Photon. Technol. Lett. **24**, 273 (2012).
5. D. E. Leaird, A. M. Weiner, S. Shen, A. Sugita, S. Kamei, M. Ishii, and K. Okamoto, Opt. Quant. Electron. **33**, 811 (2001).
6. J. D. McKinney, D. E. Leaird, and A. M. Weiner, Opt. Lett. **27**, 1345 (2002).
7. O. Mendoza-Yero, B. Alonso, G. Mínguez-Vega, Í. J. Sola, J. Lancis, and J. A. Monsoriu, Opt. Lett. **37**, 1145 (2012).
8. O. Mendoza-Yero, G. Mínguez-Vega, J. Lancis, and V. Climent, Opt. Lett. **35**, 535 (2010).
9. G. Mínguez-Vega, V. R. Supradeepa, O. Mendoza-Yero, and A. M. Weiner, Opt. Lett. **35**, 2406 (2010).
10. G. Mínguez-Vega, O. Mendoza-Yero, E. Tajahuerce, J. Lancis, and P. Andrés, IEEE Photon. Technol. Lett. **21**, 347 (2009).
11. T. Mansuryan, M. Kalashyan, J. Lhermite, E. Suran, V. Kermene, A. Barthelemy, and F. Louradour, Opt. Lett. **36**, 1635 (2011).
12. H. Baumhacker, G. Pretzler, K. J. Witte, M. Hegelich, M. Kaluza, S. Karsch, A. Kudryashov, V. Samarkin, and A. Roukossouev, Opt. Lett. **27**, 1570 (2002).
13. J. M. Bueno, B. Vohnsen, L. Roso, and P. Artal, Appl. Opt. **48**, 770 (2009).
14. J. Trull, O. Jedrkiewicz, P. Di Trapani, A. Matijošius, A. Varanavičius, G. Valiulis, R. Danielius, E. Kucinskas, A. Piskarskas, and S. Trillo, Phys. Rev. E **69**, 026607 (2004).
15. J. A. Davis, D. M. Cottrell, J. Campos, M. J. Yzuel, and I. Moreno, Appl. Opt. **38**, 5004 (1999).
16. S. Sinzinger and J. Jahns, *Microoptics* (Wiley VCH, 2003).

[III]

Dispersion management in two-photon microscopy by using diffractive optical elements.

Optics Letters, 38(4), 440-442. 2013

Dispersion management in two-photon microscopy by using diffractive optical elements

Jorge Pérez-Vizcaíno,[1] Omel Mendoza-Yero,[1] Gladys Mínguez-Vega,[1,*] Raúl Martínez-Cuenca,[1]
Pedro Andrés,[2] and Jesús Lancis[1]

[1]Institut de Noves Tecnologies de la Imatge (INIT), Universitat Jaume I, Castelló 12080, Spain
[2]Departament d'Òptica, Universitat de València, Burjassot 46100, Spain
**Corresponding author: gminguez@uji.es*

Received November 30, 2012; revised January 3, 2013; accepted January 6, 2013;
posted January 7, 2013 (Doc. ID 180996); published February 8, 2013

We demonstrate efficient generation of wide-field fluorescence signals in two-photon microscopy exploiting diffractive optical elements and short pulses by using a dispersion-compensated beam delivery optics module. Computer-generated holograms are codified onto a phase-only spatial light modulator, which allows for arbitrary single-shot patterning of the sample. Spatiotemporal shaping of the pulse is mandatory to overcome spatial chirp and pulse-front tilt effects that spread both in space and time the irradiance patterns, thus limiting not only the spatial resolution but also the signal-to-noise ratio in two-photon microscopy. By using a multipass amplifier delivering 30 fs, 0.8 mJ pulses at 1 kHz repetition rate, we experimentally demonstrated arbitrary single-shot fluorescence irradiance patterns in Rhodamine B.

OCIS codes: 090.1970, 180.4315, 190.4180.

Two- and three-dimensional images of living tissue are widely demanded in life sciences [1]. In this context, multiphoton absorption processes [2] allow for a selective excitation of fluorescence signals, providing a convenient way to acquire images with good quality. The probability of these nonlinear processes is extremely low because they rely on the absorption of two or more photons to excite a molecule to a certain vibrational state from which a fluorescence signal is emitted. Hence, the fluorescence emission is restricted to a small region of the laser focus, allowing not only high spatial resolution imaging deep into tissue [3] but also naturally axial resolution.

In this context, the laser focus traditionally is scanned across the live samples, which cause that two-photon imaging technique to suffer from time limitations on signal acquisition [4]. In fact, the time required to acquire a complete two-dimensional image of the whole field of view, depends, among other factors, on the response time of scanners. Although this drawback has been improved by using different strategies to increase the scanning speed, which include resonant mirror systems [5], acousto-optical devices [6], or polygon-mirror scanners [7], such strategies can reduce the dwell time per pixel and can compromise signal-to-noise ratio. In addition, by selectively scanning only points of interest rather than all pixels of the sample, very fast pixel-by-pixel scan processes have been reported [8,9].

In recent years, an alternative approach has been introduced to spatially multiplex the laser focus and then to carry out multibeam scanning simultaneously. This allows a more efficient use of the available laser power to either speed up imaging or to increase sampling per frame. The generation of an array of laser foci can be performed by multiple beam splitters [10], spinning disks [11], or diffractive optical elements [12]. Arbitrary diffraction patterns created by programmable spatial light modulators (SLMs), however, clearly offer more flexibility and customizability than imprinted fixed elements. For instance, SLMs can be used for simultaneous photomanipulation of living samples in a variable and temporally dynamic manner and for the stimulation or inhibition of multiple neurons at once to achieve specific excitatory and inhibition effects [4,13].

For short pulses under 100 fs, however, the irradiance patterns generated with SLMs appear naturally blurred. Apart from possible distortion effects resulting from wavefront aberrations or light scattering, this unwanted physical phenomenon mainly is attributed to the linear dependence of the scale of the Fraunhofer irradiance patterns with the wavelength of light usually known as spatial chirp. In fact, spatial chirp causes an increasing of the eccentricity of the focused spots in applications, such as real-time two-photon absorption microscopy [14] and multifocal material processing [15]. In addition, the pulse-front tilt due to the propagation time difference between pulses coming from the SLM at different transverse positions also stretches the pulse in time. This kind of temporal pulse stretching cannot be precompensated with the chirping of the original pulse like it can be done in the case of group-velocity dispersion broadening caused by the pass of the ultrashort pulse through the material of optical components.

To illustrate the impact of spatial chirp and pulse-front tilt on two-photon microscopy, consider the use of a diffraction grating of period p_0 to generate multifocal spots under pulsed light illumination of central wavelength λ_0. We assume that the laser pulse is described by the one-dimensional electric field $U(x,t) = U_0 \exp(-x^2/4\sigma_x^2) \exp(-t^2/4\sigma_t^2)$, where σ_x and σ_t denote the root-mean-square (rms) width of the spatial and temporal intensity profiles, respectively. With the help of a high numerical aperture microscope objective of focal length f_0, the diffraction orders (denoted by n) are spatially distributed at the sample plane, showing a set of tightly focused spots. As a result of the angular dispersion of the grating, each spectral component is focused at a different transverse position, which results in an elongated light spot. That is, the higher n, the longer the foci in the transversal direction x. Also, the decrease in the available bandwidth at an individual point due to the lateral walk-off of the different spectral components results in the temporal stretching of the pulse. As far as we move into higher diffraction orders, the pulse width σ_t becomes more stretched. In contrast, the number of fluorescence photons produced per second F_{ps} in a two-photon absorption process, decreases with increasing pulse width in accordance with the expression $F_{ps} \propto 1/\sigma_t$ [2]. In this example, the relative spatial and temporal broadening, with respect to the unaffected zero diffraction order, can be estimated roughly by the expressions [16] $\Delta x \cong nf_0\lambda_0^2/(4\pi c p_0 \sigma_t)$ and $\Delta\tau \cong n\lambda_0\sigma_x/cp_0$, respectively, where c is the velocity of light in vacuum. For instance, for the set of parameters $f_0 = 10$ mm, $\lambda_0 = 800$ nm, $p_0 = 83.3$ µm (or 12 lp/mm), $\sigma_t = 12.7$ fs, and $\sigma_x = 5$ mm, it can be verified easily that, for the first diffraction order, $\Delta x = 1.6$ µm and $\Delta t = 160$ fs, or $\Delta x/\sigma_0 = \Delta t/\sigma_t \cong 12.6$, where σ_0 is the rms width of the zero diffraction order. Such realistic values for the spatial and the temporal pulse broadening make the previous diffraction grating (like other diffractive optical elements) unsuitable for applications in multifocal multiphoton microscopy, as previously noted by Sacconi *et al.* [17]. Hence, both spatial chirp and pulse-front tilt phenomena adversely affect image quality and fluorescence generation, limiting the spatial resolution and the signal-to-noise ratio.

In this Letter we experimentally show two-photon absorption and fluorescence emission in Rhodamine B (RB) with spatially and temporally well-resolved irradiance patterns. To create arbitrary irradiance patterns in RB, computer-generated holograms (CGHs) were encoded onto a phase-only SLM. This allows for a dynamic and programmable optical setup with a great deal of flexibility and customizability. Spatial chirp and pulse-front tilt effects were corrected, at first order, by using an hybrid diffractive–refractive optical system that was tested experimentally in the reconstruction of dynamical CGHs [18] and the generation of second-harmonic irradiance patterns [19] with imprinted diffractive optical elements.

Figure 1 shows the proposed setup. A mode-locked Ti: sapphire laser (Femtosource, Femtolaser) provides the excitation source. The temporal width of the pulses is 30 fs amplitude FWHM ($\sigma_t = 12.7$ fs), and the central wavelength of the corresponding spectrum is $\lambda_0 = 800$ nm with a bandwidth of approximately 50 nm. The maximum energy per pulse is 0.8 mJ at a 1 kHz repetition rate. The average energy per pulse was adjusted with a half-wave plate and a polarizer, and the spatial beam width was fixed using a reflective beam expander. The ultrashort light pulses from the Ti:sapphire laser passes before exit through a postcompression stage based on fused silica Brewster prisms. In the beam delivery path, until the observation plane, one can introduce negative dispersion to later compensate for the positive material dispersion.

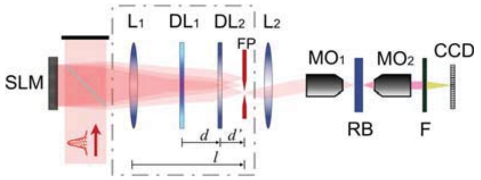

Fig. 1. (Color online) Schematic of the diffractive—refractive optical system used to improve two-photon absorption and fluorescence emission in RB.

The pulsed laser beam impinges through a beam splitter onto a Fourier CGH encoded onto a phase-only SLM that, by virtue of the beam delivery optics (BDO) inside the dashed box, images the reconstructed hologram onto its back focal plane (FP). The CGHs are calculated by using the well-known Gerchberg–Saxton iterative Fourier transform algorithm but are carried out in two stages as proposed by Wyrowski [20]. The BDO is designed as a dispersion compensating module (DCM) to provide an output irradiance distribution corresponding to the nearly wavelength-independent Fourier transform of the hologram amplitude at its back FP. More specifically (see the dashed box in Fig. 1), beam delivery is accomplished by means of a lens achromat L_1 (with focal length $f_1 = 300$ mm) coupled to a diffractive lens pair DL$_1$, DL$_2$ as was introduced in [16]. A diffractive lens can be regarded as an optical element that focuses light by diffraction, following an inverse dependence with the wavelength of light. The focal lengths of DL$_1$ and DL$_2$ for the center wavelength of the laser are denoted by $f_{01} = -150$ mm and $f_{02} = 150$ mm, respectively. Initially, the system acts as a Fourier transformer for the center wavelength, e.g., the field at FP is the Fourier transform of the field in the SLM plane for the center wavelength. In a second step, we force the design to ensure that reconstructed CGHs corresponding to each wavelength coalesces in a single spatial pattern for all the spectral components and that every ray impinging onto the SLM has an identical arrival time at the back FP. Although exact compensation is not possible, we impose a first-order, or achromatic, correction that leads to the geometrical constraints, $l = f_1$, $d^2 = -f_{01}f_{02}$, and $d' = -d^2/(d + 2f_{01})$. To compare the optical features of our proposal with a conventional setup (without DCM), we simply remove the diffractive lens pair and displace the achromatic lens L_1 to locate its back focal plane at FP.

To excite the fluorescence signal in the RB, we used a telescope composed of the refractive lens L_2 of focal length $f_2 = 100$ mm, and a 20× microscope objective MO$_1$ of focal length 10 mm. This telescope makes a reduced image of the irradiance pattern at the RB, which is contained within a cubic glass box of 10 mm thickness. The additional relay optics preserves the spatiotemporal light distribution of the irradiance pattern except for the reduced spatial scale. To observe the fluorescence signal, the plane of RB is imaged onto a conventional CCD sensor (Ueye UI-1540M, 1280 × 1024 pixel resolution and 5.2 pixel pitch) by means of a 50× microscope objective MO$_2$. We placed a suited filter F (BG39-Schott crystal) before the CCD camera to avoid transmission of infrared light.

In Fig. 2, results of the recorded fluorescence signal without (central column) and with (right column) the DCM are shown. In our experiment, the ability of the optical system to generate arbitrary irradiance distributions is illustrated with two examples, representing a bicycle in Figs. 2(a)–2(c), and a spiral in Figs. 2(d)–2(f). In the first column of Fig. 2, computer reconstruction

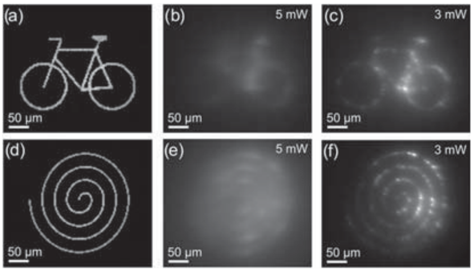

Fig. 2. Arbitrary fluorescence irradiance patterns obtained in RB (b) and (e) without compensation and (c) and (f) with DCM. (a) and (d) Corresponding reconstructed CGHs for the central wavelength of the laser.

of the CGHs corresponding to the bicycle Fig. 2(a) and the spiral Fig. 2(d) are shown. The computer reconstruction of the holograms spreads over an area of more than 400×400 pixels (or $2.08\ \text{mm} \times 2.08\ \text{mm}$). The spatial spectrum of the samples ranges from frequencies of around 25 lp/mm to about 38 lp/mm. Within this interval, the effects of theoretical spatial and temporal broadening are calculated to vary from the values $\Delta x = 3.3\ \mu\text{m}$, $\Delta t = 330$ fs to $\Delta x = 5\ \mu\text{m}$, $\Delta t = 500$ fs, respectively.

To ensure widefield fluorescence signaling all over the sample plane for the repetition rate and the pulse width of our laser system, the average power is adjusted to 3 mW. As explained, patterning was accomplished through diffractive beam delivery. As reported in [17], we found out that spatial and temporal broadening of the pulse at the sample plane makes the use of diffractive optical element unsuitable, recording no signal. The fluorescence signal was subsequently recovered when the DCM was employed [see Figs. 2(c) and 2(f)]. We attribute this effect to the dispersion compensation capability of the DCM that preserves temporal width of the laser pulse at the sample plane, thus increasing the fluorescence signal with respect to the uncompensated situation. The number of emitted photons at the sample depends inversely on the pulse width. In addition, because of spatial chirp compensation, transverse spatial resolution for the CGH reconstruction is maintained. Finally, we check that diffraction-driven fluorescence signaling is possible without the DCM, but at the expense of using an additional 2 mW average power to compensate for temporal broadening. This is not recommended when using biological samples because high levels of excitation intensity may cause photodamage and photobleaching [3]. The uncompensated spatial chirp leads to a blurred signal that prevents correct hologram reconstruction and thus irradiance patterning; see Figs. 2(b) and 2(e).

This research was funded by the Spanish Ministerio de Ciencia e Innovación through Consolider Programme (SAUUL CSD2007-00013) and project FIS2010-15746. Partial support from the Generalitat Valenciana and Fundació Caixa-Castelló through the projects PROMETEO/2012/021 and P11B2010-26 is also acknowledged. Authors are very grateful to the Serveis Centrals d'Intrumentació Científica (SCIC) of the Universitat Jaume I for the use of the femtosecond laser. We are indebted to Professor Jürgen Jahns from the FernUniversität Hagen (Germany) for making the DLs.

References

1. W. R. Zipfel, R. M. Williams, and W. W. Webb, Nat. Biotechnol. **21**, 1369 (2003).
2. B. R. Masters, *Handbook of Biomedical Nonlinear Optical Microscopy*, B. R. Masters and P. T. C. So, eds. (Oxford University, 2008).
3. W. Denk, K. R. Delaney, A. Gelperin, D. Kleinfeld, B. W. Strowbridge, D. W. Tank, and R. Yuste, J. Neurosci. Methods **54**, 151 (1994).
4. V. Nikolenko, B. O. Watson, R. Araya, A. Woodruff, D. S. Peterka, and R. Yuste, Front. Neural Circuits **2**, 1 (2008).
5. N. L. Rochefort, O. Garaschuk, R.-I. Milos, M. Narushima, N. Marandi, B. Pichler, Y. Kovalchuk, and A. Konnerth, Proc. Natl. Acad. Sci. USA **106**, 15049 (2009).
6. Y. Otsua, V. Bormutha, J. Wonga, B. Mathieub, G. P. Duguéa, A. Feltz, and S. Dieudonnéa, J. Neurosci. Methods **173**, 259 (2008).
7. W. C. Warger, G. S. Laevsky, D. J. Townsend, M. Rajadhyaksha, and Ch. A. DiMarzio, J. Biomed. Opt. **12**, 044006 (2007).
8. W. Göbel and F. Helmchen, J. Neurophysiol. **98**, 3770 (2007).
9. K. P. Lillis, A. Enga, J. A. White, and J. Mertz, J. Neurosci. Methods **172**, 178 (2008).
10. T. Nielsen, M. Fricke, D. Hellweg, and P. Andresen, J. Microsc. **201**, 368 (2001).
11. J. Bewersdorf, R. Pick, and S. W. Hell, Opt. Lett. **23**, 655 (1998).
12. D. C. O'Shea, T. J. Suleski, A. D. Kathman, and D. W. Prather, *Diffractive Optics: Design, Fabrication, and Test* (SPIE, 2004).
13. B. O. Watson, V. Nikolenko, R. Araya, D. S. Peterka, A. Woodruff, and R. Yuste, Front. clin. Neurosci. **4**, 1 (2010).
14. A. H. Buist, M. Müller, J. Squer, and G. J. Brakenhoff, J. Microsc. **192**, 217 (1998).
15. Z. Kuang, W. Perrie, J. Leach, M. Sharp, S. P. Edwardson, M. Padgett, G. Dearden, and K. G. Watkins, Appl. Surf. Sci. **255**, 2284 (2008).
16. G. Mínguez-Vega, J. Lancis, J. Caraquitena, V. Torres-Company, and P. Andrés, Opt. Lett. **31**, 2631 (2006).
17. L. Sacconi, E. Froner, R. Antolini, M. R. Taghizadeh, A. Choudhury, and F. S. Pavone, Opt. Lett. **28**, 1918 (2003).
18. Ll. Martínez-León, P. Clemente, E. Tajahuerce, G. Mínguez-Vega, O. Mendoza-Yero, M. Fernández-Alonso, J. Lancis, V. Climent, and P. Andrés, Appl. Phys. Lett. **94**, 011104 (2009).
19. R. Martínez-Cuenca, O. Mendoza-Yero, B. Alonso, Í. J. Sola, G. Mínguez-Vega, and J. Lancis, Opt. Lett. **37**, 957 (2012).
20. F. Wyrowski, J. Opt. Soc. Am. A **7**, 961 (1990).

[IV]

On-axis non-linear effects with programmable Dammann lenses under femtosecond illumination.

Optics Letters, 38(10), 1621-1623. 2013.

On-axis non-linear effects with programmable Dammann lenses under femtosecond illumination

Jorge Pérez Vizcaíno,[1,*] **Omel Mendoza-Yero,**[1] **Rocío Borrego-Varillas,**[1,2] **Gladys Mínguez-Vega,**[1]
Javier R. Vázquez de Aldana,[2] **and Jesús Láncis**[1]

[1]*Instituto de Nuevas Tecnologías de la Imagen (INIT), Universidad Jaume I, Castellón E 12080, Spain*

[2]*Departamento de Física Aplicada, Universidad de Salamanca, Salamanca, E-37008, Spain*
**Corresponding author: jvizcain@uji.es*

Received February 8, 2013; revised April 10, 2013; accepted April 12, 2013;
posted April 12, 2013 (Doc. ID 185116); published May 8, 2013

We demonstrate the utilization of Dammann lenses codified onto a spatial light modulator (SLM) for triggering nonlinear effects. With continuous wave illumination Dammann lenses are binary phase optical elements that generate a set of equal intensity foci. We theoretically calculate the influence of ultrashort pulse illumination on the uniformity of the generated pattern, which is affected by chromatic aberration for pulses with temporal widths lower than 100 fs. The simulations also indicate that acceptable uniformity can be achieved for pulses of several fs by shortening the distance among foci which can be easily modified with the SLM. Multifocal second-harmonic generation (SHG) and on-axis multiple filamentation are produced and actively controlled in $\beta-\mathrm{BaB_2O_4}$ (BBO) and fused silica samples, respectively, with an amplified Ti: Sapphire femtosecond laser of 30 fs pulse duration. Experimental results are in very good agreement with theoretical calculations. © 2013 Optical Society of America

OCIS codes: (050.1940) Diffraction; (320.6629) Supercontinuum generation; (320.7110) Ultrafast nonlinear optics.
http://dx.doi.org/10.1364/OL.38.001621

The study of the non-linear processes [1] that take place during the interaction of light with matter has benefited from the high peak powers achieved with amplified femtosecond (fs) lasers [2]. This opens a huge gate toward the development of many applications in the nonlinear optics field. For instance, second-order parametric processes [3] are efficiently used to tune the central wavelength through SHG or sum/difference-frequency generation, expanding the accessible wavelength range of standard Ti:sapphire laser systems. Third-order processes are also very often exploited to increase the spectral width of fs pulses through optical-Kerr effect (self-phase modulation), or in combination with strong-field ionization and higher order processes (supercontinuum generation [4] and filamentation [5]). The increase of the spectral width by means of the abovementioned nonlinear effects allows subsequent compression of the pulse to a much shorter temporal duration [6].

Most of these processes require the focusing of the laser beam [7] just to reach the high intensities needed to trigger the desired effect. However, under certain circumstances, the spatiotemporal properties of the pulse focusing itself can be exploited to gain control over the nonlinear mechanisms taking place. In this sense, diffractive lenses have been recently employed for SHG [8] or in super continuum generation [9]: the strong chromatic aberration induced by diffraction changes the spectral properties of the pulse.

On the other hand, Dammann diffraction gratings are binary phase distributions of alternate 0, π zones for well-defined transient points [10,11]. For continuous wave (CW) illumination, these gratings generate diffraction patterns characterized by a number N of diffracted orders with the same peak intensity. This concept can be easily extended to lenses. The phase of a converging refractive lens can be represented by $\pi r^2/\lambda f$, where r denotes the radial coordinate, f the focal length, and λ the wavelength of light. The lens function $\exp(i\pi r^2/\lambda f)$ can be binarized by applying the Dammann grating formalism to the squared radial coordinate r^2 [12]. The resultant binary lens function will create a series of N focal planes having focal lengths of f/n with equal peak intensities, where $n = (\ldots, -3, -1, 1, 3, \ldots)$ for an even number of orders, and $n = (\ldots, -2, -1, 0, 1, 2, \ldots)$ for an odd number of orders [13]. Although Dammann lenses encoded into a spatial light modulator (SLM) can be a powerful tool for dynamic control and generation of nonlinear effects, they have not been explored yet in this context.

In this letter, we first summarize the characteristics of the on-axis diffraction pattern for Dammann lenses encoded into an SLM illuminated by ultrashort laser sources. Second, two results from experiments are shown to prove its potential to trigger nonlinear effects. Specifically, we demonstrate the application of Dammann lenses to SHG and filamentation in transparent dielectrics.

In Fig. 1 a schematic diagram of the optical setup is shown. For the experiment we use a Ti:Sapphire fs laser that emits linearly polarized pulses of about 30 fs at intensity FWHM, centered at $\lambda_0 = 800$ nm, with 50 nm of spectral bandwidth and a repetition rate of 1 kHz. Dammann lenses are encoded onto a reflective liquid

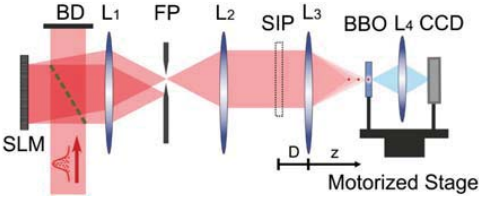

Fig. 1. Experimental setup for the analysis of nonlinear effects caused by multiple on-axis foci generated with Dammann lenses encoded into an SLM. The input beam is split in two rays by a beam splitter (green dotted line) to work with the SLM at normal incidence. A beam dumper (BD) is used to block the unused part of the beam.

0146-9592/13/101621-03$15.00/0

crystal on silicon (LCoS) SLM (Holoeye Pluto). The SLM has 1920 × 1080 pixels with 8 μm of pixel pitch. The reflected beam from the SLM passes through a 1× telescope composed of a pair of lenses L_1 and L_2 of focal lengths $f_1 = f_2 = 100$ mm. The telescope makes an image of the SLM plane after the lens L_2. To avoid the zero diffraction order of the SLM, we overlap a linear phase of period 0.3 mm to the Dammann lens, and use in the experiment its first diffraction order.

In addition, to ensure an equal spacing among all Dammann foci, a third lens L_3 is placed at the focal length distance f_3=50 mm from the SLM image plane (SIP). This configuration allows us to obtain a number N of equally spaced focused spots with the same peak irradiance. The focal planes ($z = f_n$ from L_3) of the foci can be determined by the expression

$$\frac{1}{f_n} = \frac{1}{F} - \frac{n}{nD - f}. \qquad (1)$$

From Eq. (1), it follows that there are three parameters to control the output of our optical system: the number of foci (related to the parameter n), the focal length of Dammann lenses, and the focal length of the refractive lens L_3. The axial width of the foci can be determined by solving the Huygens–Fresnel diffraction equation in the ABCD matrix formalism. To do that, we calculate the irradiance distribution along the propagation axis z when no phase is encoded into the SLM (it can be regarded as a mirror), and thus a collimated laser beam reaches the refractive lens L_3, i.e., when $n = 0$. In this condition, the normalized on-axis irradiance can be determined by the expression

$$I(z) = \frac{\sin^2\left(\frac{A\pi a^2}{\lambda z}\right)}{A^2}, \qquad (2)$$

where $A = 1 - z/F$ and a is the radius of the encoded Dammann lens. At this point we analyze the influence of broadband light spectra on the irradiance given by Dammann lenses under ultrashort pulsed illumination. In the bottom part of Fig. 2 the Fresnel diffraction integral is used to simulate the irradiance $I(z)$. Here, the on-axis irradiance obtained with a Dammann lens of 5 equal foci separated by 2.05 mm is shown. As it can be seen in the top part of Fig. 2, the simulation was carried out for two different Fourier transform limited Gaussian laser pulses, and an ideal CW source.

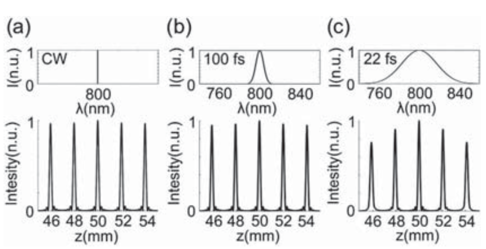

Fig. 2. Simulated irradiance patterns obtained with a Dammann lens, which is illuminated with (a) monochromatic beam, (b) 100 fs laser pulse, and (c) 22 fs laser pulse.

The irradiance uniformity in the case of the CW source is approximately 10^{-5} [11]. Small discrepancies in the height of the peaks are caused mainly due to deviations of the $0 - \pi$ transition locations from their ideal values when encoding Dammann lenses into an SLM [14,15]. For an ultrashort laser pulse of 100 fs falls of 0.3% and 1.5% (for n = ±1 and n = ±2 orders, respectively) are registered. The equivalent values for 22 fs pulses were 6% and 20%. In accordance to our simulations, for laser pulses close to or greater than 100 fs, chromatic aberrations do not influence excessively the uniformity of Damman irradiance patterns. In contrast, for shorter pulses (below a few tens of fs), the effects of chromatic aberrations cannot be neglected e.g., see Fig. 2(c). In addition, we found out that the longer the separation between foci, the greater the reduction of the irradiance uniformity due to chromatic aberrations. Therefore, chromatic aberrations will increase the spatial width and decrease the peak irradiance of the foci, reducing the uniformity of the generated irradiance patterns. The efficiency of this experiment is mainly affected by the SLM device efficiency and the inherent Dammann lens efficiency. Taking all into account the estimated efficiency of the system is of about 40%.

In order to show the potential of Dammann lenses to manage non-linear effects, we developed a couple of experiments. First, we explored SHG originated by a programmable set of on-axis Dammann foci. To do that, a type-I $\beta - BaB_2O_4$ (BBO) crystal ($\theta = 29.2°$, 20 μm thickness) was displaced along the different foci generated with Dammann lenses in the focal region of L_3. With the help of the lens L_4, magnified images of each focus were formed onto a charge-coupled device (CCD) camera. To avoid transmission of infrared light a suitable filter was placed in front of the CCD. The scanning device (made up of BBO crystal, lens L_4, and CCD) was mounted on a motorized stage, which allows for computer controlled movements via Matlab code. The thickness of the non-linear crystal ensures enough spectral acceptance for the SHG of the fundamental pulses, which energy was carefully set to avoid the damage of the crystal during the scan.

In Fig. 3, experimental results are shown. Furthermore, images of the transversal focal spots, the spectrum

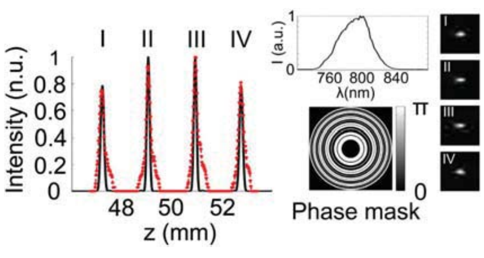

Fig. 3. On-axis multifocal SHG with Dammann lenses: experiment (red dotted line) and theory (black line). Dammann phase mask, pulse spectrum, and images of the foci from a lateral side of the non-linear crystal are shown as insets.

of our laser, and the encoded Dammann phase mask are provided as insets. This Dammann phase mask generates a set of $N = 4$ foci separated by 1.92 mm. The motor step was set to 20 μm, whereas the focal length of L_3 was $F = D = 50$ mm. The second harmonic irradiance recorded with the CCD is plotted as a function of the distance z from the lens L_3, and represented by a red dotted line. Within the paraxial Fresnel approximation, the experimental results are compared to numerical simulations (black line) of the squared normalized irradiance $I^2(z)$ calculated for the measured spectrum of our laser. From a visual inspection of Fig. 3 it is apparent that experimental results are in good agreement with the simulations. We believe that almost inappreciable differences in the locations of the peak irradiances are mainly due to possible deviations of the pulsed laser beam (toward convergence behavior) from its collimated state before the L_3 lens. In addition, the increase in the axial width of experimental data with respect to simulations is mainly attributed to the discrepancy of our beam from the plane wave illumination considered in simulations. Misalignment can also influence the broadening of the foci slightly.

In the second experiment, we take advantage of programmable Dammann lenses to produce multiple spatially tuned filaments in a fused silica sample. The motorized stage was removed and a fused silica sample (20 mm × 10 mm × 5 mm) with all faces polished was placed in the focal region of L_3 lens ($F = D = 50$ mm). Then, the pulse energy was progressively increased from 0 to the minimum value at which filaments were observed in the sample at the various foci of the lens. The plasma emission of the filaments was registered in a CCD from one of the sides of the sample. The number of foci, as well as the distance between them, was controlled to produce several filaments with different Dammann phase masks. The corresponding images are shown in Fig. 4. Moreover, the yellow lines show the on-axis irradiance profiles along the whole extension of the filaments. In particular, Fig. 4(a) and 4(b) correspond to four filaments with separations of 2.1 and 0.4 mm, respectively. In Fig. 4(c) three filaments separated by 2.14 mm are generated, whereas in Fig. 4(d) the number of filaments is increased to six with a distance among them of 0.85 mm. As it might be expected both the shape and intensity of the filaments change with their distance from the air-glass interface due to the spherical aberration induced by light refraction [16,17].

We have shown that Dammann lenses can be used as a powerful tool to manipulate “at will” certain non-linear effects with intense fs pulses. Hence, several applications might be expected e.g., for performing in-depth parallel processing of transparent dielectrics [18,19]. In this paper we have investigated on-axis Dammann lenses, but our formalism can be easily extended to other cases (e.g., bidimensional Dammann structures).

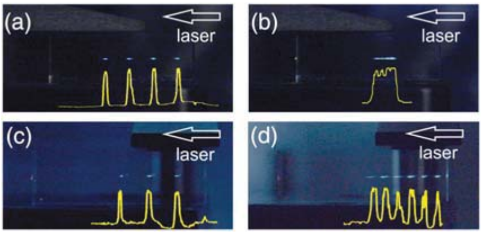

Fig. 4. Examples of multifilament generation in fused silica glass. The number of filaments and distances between them are changed by encoding different Dammann lenses.

This research was funded by the Spanish Ministerio de Ciencia e Innovación through Consolider Programme (SAUUL CSD2007-00013) and FIS2010-15746. Also, financial support from the Generalitat Valenciana through project PROMETEO/2012/021 and Pla Propi de Investigació de la Universitat Jaume I through project P11B2010-26 is acknowledged. Authors are also very grateful to the SCIC of the Universitat Jaume I for the use of the femtosecond laser.

References

1. R. W. Boyd, *Nonlinear Optics* (Academic, 2008).
2. D. Strickland and G. Mourou, Opt. Commun. **56**, 219 (1985).
3. P. Franken, A. Hill, C. Peters, and G. Weinreich, Phys. Rev. Lett. **7**, 118 (1961).
4. R. Alfano, *The Supercontinuum Laser Source* (Springer, 2006).
5. A. Couairon and A. Mysyrowicz, Phys. Rep. **441**, 47 (2007).
6. M. Nisoli, S. De Silvestri, and O. Svelto, Appl. Phys. Lett. **68**, 2793 (1996).
7. G. Boyd and D. Kleinman, J. Appl. Phys. **39**, 3597 (1968).
8. G. Mínguez-Vega, C. Romero, O. Mendoza-Yero, J. R. Vázquez de Aldana, R. Borrego-Varillas, C. Méndez, P. Andrés, J. Lancis, and L. Roso, Opt. Lett. **35**, 3694 (2010).
9. C. Romero, R. Borrego-Varillas, A. Camino, G. Minguez-Vega, O. Mendoza-Yero, J. Hernandez-Toro, and J. R. Vázquez de Aldana, Opt. Express **19**, 4977 (2011).
10. H. Dammann and E. Klotz, Opt. Acta **24**, 505 (1977).
11. C. Zhou and L. Liu, Appl. Opt. **34**, 5961 (1995).
12. I. Moreno, J. A. Davis, D. M. Cottrell, N. Zhang, and X.-C. Yuan, Opt. Lett. **35**, 1536 (2010).
13. J. A. Davis, I. Moreno, J. L. Martínez, T. J. Hernández, and D. M. Cottrell, Appl. Opt. **50**, 3653 (2011).
14. J. Yu, C. Zhou, W. Jia, W. Cao, S. Wang, J. Ma, and H. Cao, Appl. Opt. **51**, 1619 (2012).
15. D. C. O´Shea, Appl. Opt. **34**, 6533 (1995).
16. N. Huot, R. Stoian, A. Mermillod-Blondin, C. Mauclair, and E. Audouard, Opt. Express **15**, 12395 (2007).
17. Q. Sun, H. Jiang, Y. Liu, Y. Zhou, H. Yang, and Q. Gong, J. Opt. A **7**, 655 (2005).
18. R. Gattass and E. Mazur, Nat. Photonics **2**, 219 (2008).
19. C. Mauclair, A. Mermillond-Blondin, S. Landon, N. Huot, A. Rosenfeld, I. V. Hertel, E. Audouard, I. Myiamoto, and R. Stoian, Opt. Lett. **36**, 325 (2011).

[V]

Controlled multi-beam supercontinuum generation with a spatial light modulator.

Photonics Technology Letters, IEEE, 26(16), 1661-1664. 2014.

Controlled Multibeam Supercontinuum Generation With a Spatial Light Modulator

Rocio Borrego-Varillas, Jorge Pérez-Vizcaíno, Omel Mendoza-Yero, Gladys Mínguez-Vega,
Javier R. Vázquez de Aldana, and Jesús Lancis, *Member, IEEE*

***Abstract*— We report on deterministic femtosecond multifilamentation in fused silica by encoding a diffractive microlens array into a spatial light modulator. The efficiency and focal length of each microlens are modified through the addressing voltage. This allows for a precise control on the energy coupled to the filaments thus obtaining a homogenized supercontinuum pattern from an inhomogeneous irradiance input distribution. Slight changes in the focal length of the microlenses allow for independent tailoring of the supercontinuum spectra.**

***Index Terms*— Optical pulse shaping, optical arrays, supercontinuum generation.**

I. INTRODUCTION

FILAMENTATION [1] is a regime of nonlinear propagation where the equilibrium between the self-focusing process, caused by Kerr effect, and the plasma induced defocusing, leads to the self-guiding of light for distances considerably larger than the Rayleigh length [2]. This phenomenon can eventually give rise to an extreme spectral broadening, ranging from the ultraviolet to the infrared regions, termed supercontinuum (SC) generation [3], [4]. Currently, the ongoing research in filamentation ranges from the modeling of the process to the generation of filaments with high flexibility for many different applications.

Spectral control of the SC is desired in applications like femtosecond time-resolved spectroscopy [5], spectral interferometry [6], or in optical parametric amplifiers [7].

When the laser power is much higher than the critical power for self-focusing, the beam undergoes a break-up into multiple filaments. It has been demonstrated that multiple filamentation (MF) originates from transverse modulation instabilities [8], [9], thus producing a random distribution of filaments. Gaining control over the spatial filaments distribution is an important task in applications such as filamentation-based tumor treatment [10], a novel technique which has been recently proposed for cancer therapy. In such case, careful management of both the position and the energy of the filaments, is decisive to control the radiological dose and avoid damage of the adjacent healthy tissue. Another example is the inscription of optical waveguides in dielectrics by direct irradiation with femtosecond pulses that requires the control of the weak plasma generated in the bulk [11]. Although these applications would benefit from MF in terms of speed, they demand for flexible setups that allow for a precise control of the parameters governing the process, such as the energy or the numerical aperture.

Up to now, several strategies have been proposed for deterministic MF: amplitude modulation by a periodic mesh [12], [13], nonlinear interaction of two overlapping beams [14], Dammann lenses [15] and wavefront shaping [16], among others. In this sense, focusing the beam by a microlens array is an attractive approach. Watanabe et al. were the first to report a SC array by focusing femtosecond laser pulses into a liquid with a microlens array [17]. Cook and coworkers demonstrated the generation of coherent continuum filaments in B270 glass by using an array of diffractive microlenses (DMLs) [18]. More recently, Camino et al. [19] proposed deterministic MF in fused silica by adjusting the diffraction pattern generated by a loosely focusing 2D periodic lens array. However, it is still necessary to gain further control over the individual filaments, in terms of energy and spectrum, if real industrial, scientific or biomedical applications want to be developed.

Current megapixel spatial light modulators (SLMs) offer the possibility for versatile and fine control of light beams at the micrometric scale. The use of SLMs has benefited a wide range of applications in adaptive optics [20], [21], scattering media [22] or optical microscopy [23]. In this Letter, we report active control of MF in a solid medium by codifying a diffractive microlens array in a phase-only SLM. We demonstrate for the first time, to our knowledge, precise control on the energy coupled to each one of the filaments thus obtaining a homogeneous SC beam. This is achieved by changing independently the efficiency of each microlens. Moreover, the spectrum of the generated SC was tuned by slightly changing the focal length of the lenses, in agreement with previous observations [24].

II. EXPERIMENT SETUP

A scheme of the experimental setup is shown in Fig. 1. For the experiment we used a Ti:Sapphire femtosecond laser that

---

Manuscript received January 22, 2014; revised April 11, 2014; accepted June 7, 2014. Date of publication June 12, 2014; date of current version July 25, 2014. This work was supported in part by the Generalitat Valenciana under Project PROMETEO/2012/021, in part by the Excellence Net about Medical Imaging under Project ISIC/2012/013, and in part by the Pla Propi de Investigació de la Universitat Jaume I under Project P1·1B2013-53.

R. Borrego-Varillas, J. Pérez-Vizcaíno, O. Mendoza-Yero, G. Mínguez-Vega, and J. Lancis, are with the Departament de Ciències Experimentals, Universitat Jaume I, Castelló 12080, Spain (e-mail: rocio.borrego@polimi.it; jvizcain@uji.es; omendoza@uji.es; gminguez@fca.uji.es; lancis@uji.es).

J. R. Vázquez de Aldana is with the Grupo de Investigación de Microprocesado de Materiales con Láser, Universidad de Salamanca, Salamanca E-37008, Spain (e-mail: jrval@usal.es).

Color versions of one or more of the figures in this letter are available online at http://ieeexplore.ieee.org.

Digital Object Identifier 10.1109/LPT.2014.2330362

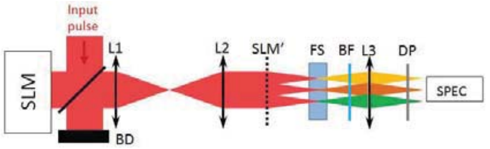

Fig. 1. Experimental setup. The input pulse is divided at the 55:45 beam splitter (BD: beam dumper) and reaches the SLM. The pattern generated by the microlens array is focalized in the fused silica (FS) sample. The exiting light is filtered out with a band-pass filter (BF) and collected with a lens and a diffusing plate (DP) into an spectrometer.

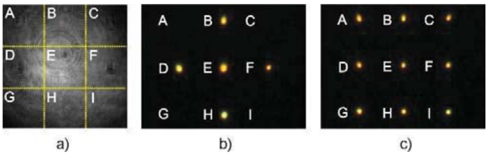

Fig. 2. a) Beam profile at the SLM plane for 76 μJ input energy. The yellow lines denote the edges of the DLMs; b) SC signal for 76 μJ input energy and c) SC signal for 170 μJ input energy with efficiency correction as explained in the text.

emits linearly polarized pulses of about 30 fs (full width half maximum in intensity), centered at λ_0=800 nm, with 50 nm of spectral bandwidth and a repetition rate of 1 kHz.

The beam was incident on a reflective liquid crystal on silicon SLM (Holoeye Pluto) after reflecting on a beam splitter. The SLM has 1920×1080 pixels with 8 μm of pixel pitch. The reflected beam from the SLM passed through the beam splitter, and then, a 1× telescope composed by a pair of lenses L_1 and L_2 of focal lengths f_1=f_2=100 mm, imaged the SLM at the focal plane of L_2 (labelled as SLM' in Fig. 1).

The phase encoded onto the SLM consisted of an array of 3×3 lenses (1.73×1.73 mm^2 each). The phase for each DML corresponds to that of a kinoform profile given by [15]:

$$\varphi_j(r) = mod\left[\frac{\pi r^2}{\lambda_0 f_j}, 2\pi\right] \tag{1}$$

where j-index refers to each DML, λ_0 is the central wavelength of the incident pulse, f_j is the focal length, r is the radial coordinate from the center of the j-th lens, and the function $mod(x, y)$ gives the remainder on division of x by y. This phase ranges from 0 to 2π. In order to gain control over the energy coupled in this focus for each DMLs Eq. (1) is multiplied by α_j. The parameter α_j varies from 0 to 1 and allows for the control of the diffraction efficiency of the lens [30], [31]. In this way, the new encoded phase is

$$\Psi_j(r) = \alpha_j \varphi_j(r) \tag{2}$$

For α_j=1 nearly all the light reflected in the corresponding j-th lens of the array is directed into the focus. However, when $\alpha_j \neq 1$ the energy coupled to the main focus is reduced.

The relation between the value of α and the corresponding efficiency η for the generated pattern is given by [25]:

$$\eta_j = sinc^2(\alpha_j - 1) \tag{3}$$

where $sinc(x)$=$sin(\pi x)/(\pi x)$.

The parameters of the codified microlens array were uniformly set to f_j=60 mm and α_j=1 in the beginning. A fused silica sample (5×10×20 mm^3, all faces polished to optical grade) was placed in such a way that the multiple beams entered through the 5 mm long face and focused inside the sample (see Fig. 1). The pulse energy, controlled by a variable attenuator, was carefully adjusted just above the threshold to the produce SC with the central beam.

Note that, although sapphire is preferable in terms of stability and bandgap, the energy provided by our laser was not sufficient to generate a 9 × 9 array due to its larger SC threshold.

At the rear face of the fused silica sample, the non-converted infrared beam was removed by means of a band-pass filter (FGB37, Thorlabs). The SC light was collected with a lens L_3 (f_3=100 mm) and projected onto a white screen. Images of the projected SC patterns were recorded with a CMOS camera (Canon EOS, 1100-D). Spectrum measurements of the SC patterns were taken by removing the white screen and placing a diffusing plate and a fiber coupled to a spectrometer (StellarNet Inc, CXR-SR-200) instead. The lateral profiles of the generated filaments were imaged through a f=60 mm lens onto a CMOS-based camera (uEye, IDS 1460-C).

III. EXPERIMENTAL RESULTS

Owing to the Gaussian distribution of our beam profile the energy is mainly concentrated on the center and, therefore, a different fraction of the incident energy will be delivered to the different microlenses (termed A, B….I, see Fig. 2.a). As a consequence, the values of the efficiency parameters, α_j, are required to be determined in order to get a uniform distribution of the intensity for all the foci of the microlenses. In order to do that, we measured the threshold pulse energy (incident on the beam-splitter) for SC generation in each one of the 9 microlenses. The threshold is defined as the minimum pulse energy required to just start SC generation (detected with the spectrometer). The measured values ranged from 30 μJ for the central microlens (E) to 160 μJ in the case of one of the external lenses (I). Please note that these values refer to the energy impinging the array, not a single lens. Due to the losses in the beam-splitter and in the SLM, we estimate a 10.5% of the total energy reaching the fused silica sample. From the threshold energies, the efficiency parameters were individually calculated as the rate

$$\alpha_j = U_j / max\left(U_j\right) \tag{4}$$

and the obtained values were codified in the DLM.

In Fig. 2 b) we show the visible output signal projected on a screen for an input energy of 76 μJ with all the efficiency parameters set to α_j=1. As it can be seen in the figure, SC is produced only in the central and the four adjacent foci provided the energy delivered to the external lenses does not exceed the threshold. Moreover, the visible spectrum generated with the 5 central lenses was not identical as expected from the different intensities reached at their corresponding foci.

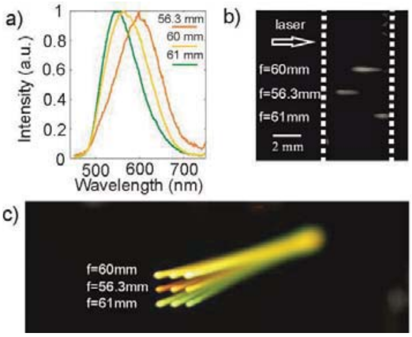

Fig. 3. Filaments' profiles inside the fused silica sample (the dotted lines indicate the sample's input and output faces); b) corresponding spectra measured behind the FGB37 filter and c) photograph of the generated SC light.

Then, we implemented in the DLM the α_j values obtained from Eq. 4 and we increased the input energy to 170 μJ. This value is slightly above the SC threshold to guarantee that no structural damage was inflicted upon the plate. Under this configuration, the energy delivered to all the foci was just above the SC threshold and a homogeneous visible signal was generated (see Fig. 2c), both in the spectrum as in the conversion efficiency. An inspection of the fused silica plate revealed that no permanent damage was induced in the sample under these experimental conditions.

So far, we have corrected the influence of spatial inhomogeneties of the incident beam in the intensity and spectrum of the SC via the parameters α_j. In a second set of experiments, we pursued control over the spectral properties of the so-generated beams. A direct way to do that is, for instance, increasing the incident pulse energy. However, in practical applications an increase in the input energy is undesirable because it could easily lead to a permanent damage in the sample [26]. Recently, it has been demonstrated [24] that when a femtosecond beam is focused with a diffractive lens, wavelength tunability in the SC signal can be achieved by simply changing the lens-sample relative distance. It was found that the depth at which the filament is formed is closely connected to the SC spectrum [27]. Based on this, the position of the filament, and thus the spectral content of the SC generated signal, could be controlled by slightly modifying the focal length of the DMLs and keeping the pulse energy constant. Obviously, when changing the focal length, the numerical aperture of the focusing beams is also slightly changed.

We implemented this idea in the SLM. The pulse energy was set to 200 μJ and the values of α_j were set to the computed values for foci homogeneization. Then, we codified in the DML phases corresponding to different focal lengths. As expected, the spectra of the generated SC changed in agreement with our expectations, as it can be seen in Fig. 3b. As an example of the flexibility of our setup, we set different focal lengths for each row of lenses (i.e., $f_A = f_B = f_C$=61 mm, $f_D = f_E = f_F$=56.3 mm and $f_G = f_H = f_I$=60 mm). The filaments produced inside the silica sample, moved accordingly (see Fig. 3a). Moreover, the DMLs with the longer focal lengths (A–C) formed short filaments, clipped by the rear face of the sample. This is associated with spectra tuned towards the shortest wavelengths, which is in accordance with the observations in [26]. In contrast, for the shortest focal lengths (D–F), filaments developed slightly behind the front face. Under these conditions, three colored patters were observed at the output of the sample (see Fig. 3c).

IV. CONCLUSION

In conclusion, we have reported controlled MF in fused silica by encoding a DML array in a phase-only SLM for SC generation. We have demonstrated a precise and independent control on (i) the energy coupled to each of the filaments by means of the α parameter, and (ii) the spectrum of the generated SC light by changing the focal length of the DMLs. We believe that the results of these investigations can be useful in applications which demand for homogenized MF patterns and/or spectral tunability, including femtosecond laser inscription, time-resolved spectroscopy or tumor treatment.

REFERENCES

[1] A. Braun, G. Korn, X. Liu, D. Du, J. Squier, and G. Mourou, "Self-channeling of high-peak-power femtosecond laser pulses in air," *Opt. Lett.*, vol. 20, no. 1, pp. 73–75, 1995.

[2] A. Couairon and A. Mysyrowicz, "Femtosecond filamentation in transparent media," *Phys. Rep.*, vol. 441, nos. 2–4, pp. 47–189, Mar. 2007.

[3] R. R. Alfano and S. L. Saphiro, "Emission in the region 4000 to 7000 Å via four-photon coupling in glass," *Phys. Rev. Lett.*, vol. 24, no. 11, pp. 584–587, 1970.

[4] R. R. Alfano, *The Supercontinuum Laser Source*. New York, NY, USA: Springer-Verlag, 2006.

[5] V. I. Klimov and D. W. McBranch, "Femtosecond high-sensitivity, chirp-free transient absorption spectroscopy using kilohertz lasers," *Opt. Lett.*, vol. 23, no. 4, pp. 277–279, 1998.

[6] Z. W. Wilkes, S. Varma, Y.-H. Chen, H. M. Milchberg, T. G. Jones, and A. Ting, "Direct measurements of the nonlinear index of refraction of water at 815 and 407 nm using single-shot supercontinuum spectral interferometry," *Appl. Phys. Lett.*, vol. 94, no. 21, pp. 211102–211103, 2009.

[7] G. Cerullo and S. De Silvestri, "Ultrafast optical parametric amplifiers," *Rev. Sci. Instrum.*, vol. 74, no. 1, pp. 1–18, 2003.

[8] H. Schroeder, J. Liu, and S. L. Chin, "From random to controlled small-scale filamentation in water," *Opt. Exp.*, vol. 12, no. 20, pp. 4768–4774, 2004.

[9] L. Bergé *et al.*, "Multiple filamentation of terawatt laser pulses in air," *Phys. Rev. Lett.*, vol. 92, no. 22, pp. 225002–225005, 2004.

[10] R. Meesat *et al.*, "Cancer radiotherapy based on femtosecond IR laser-beam filamentation yielding ultra-high dose rates and zero entrance dose," *Proc. Nat. Acad. Sci.*, vol. 109, no. 38, pp. E2508–E2513, 2012.

[11] R. Osellana, G. Cerullo, and R. Ramponi, *Femtosecond Laser Micromachining*. Berlin, Germany: Springer-Verlag, 2012.

[12] V. P. Kandidov *et al.*, "Towards a control of multiple filamentation by spatial regularization of a high-power femtosecond laser pulse," *Appl. Phys. B*, vol. 80, no. 2, pp. 267–275, 2005.

[13] O. G. Kosareva *et al.*, "Array of femtosecond plasma channels in fused silica," *Opt. Commun.*, vol. 267, no. 2, pp. 511–523, 2006.

[14] J. Liu, H. Schroeder, S. L. Chin, R. Li, and Z. Xu, "Ultrafast control of multiple filamentation by ultrafast laser pulses," *Appl. Phys. Lett.*, vol. 87, no. 16, pp. 161105-1–161105-3, Oct. 2005.

[15] J. P. Vizcaíno, O. Mendoza-Yero, R. Borrego-Varillas, G. Mínguez-Vega, J. R. Vázquez de Aldana, and J. Láncis, "On-axis non-linear effects with programmable Dammann lenses under femtosecond illumination," *Opt. Lett.*, vol. 38, no. 10, pp. 1621–1623, 2013.

[16] C. P. Hauri, J. Biegert, U. Keller, B. Schaefer, K. Mann, and G. Marowski, “Validity of wave-front reconstruction and propagation of ultrabroadband pulses measured with a Hartmann-Shack sensor,” *Opt. Lett.*, vol. 30, no. 12, pp. 1563–1565, 2005.

[17] W. Watanabe, Y. Masudda, H. Arimoto, and K. Itoh, “Coherent array of white-light continuum generated by microlens array,” *Opt. Rev.*, vol. 6, no. 3, pp. 167–172, 1999.

[18] K. Cook, R. McGeorge, A. K. Kar, M. R. Taghizadeh, and R. A. Lamb, “Coherent array of white-light continuum filaments produced by diffractive microlenses,” *Appl. Phys. Lett.*, vol. 86, no. 2, pp. 021105-1–021105-3, Jan. 2005.

[19] A. Camino, Z. Hao, X. Liu, and J. Lin, “Control of laser filamentation in fused silica by a periodic microlens array,” *Opt. Exp.*, vol. 21, no. 7, pp. 7908–7915, 2013.

[20] J. Arines *et al.*, “Measurement and compensation of optical aberrations using a single spatial light modulator,” *Opt. Exp.*, vol. 15, no. 23, pp. 15287–15292, 2007.

[21] S. Ngcobo, I. Litvin, L. Burger, and A. Forbes, “A digital laser for on-demand laser modes,” *Nature Commun.*, vol. 4, p. 2289, Jul. 2013.

[22] I. M. Vellekoop and A. P. Mosk, “Focusing coherent light through opaque strongly scattering media,” *Opt. Lett.*, vol. 32, no. 16, pp. 2309–2311, 2007.

[23] C. Maurer, A. Jesacher, S. Bernet, and M. Ritsch-Marte, “What spatial light modulators can do for optical microscopy,” *Laser Photon. Rev.*, vol. 5, no. 1, pp. 81–101, 2011.

[24] C. Romero *et al.*, “Diffractive optics for spectral control of the supercontinuum generated in sapphire with femtosecond pulses,” *Opt. Exp.*, vol. 19, no. 6, pp. 4977–4984, 2011.

[25] V. Moreno, J. F. Román, and J. R. Salgueiro, “High efficiency diffractive lenses: Deduction of kinoform profile,” *Amer. J. Phys.*, vol. 65, pp. 556–562, Dec. 1997.

[26] C. B. Schaffer, A. Brodeur, and E. Mazur, “Laser-induced breakdown and damage in bulk transparent materials induced by tightly focused femtosecond laser pulses,” *Meas. Sci. Technol.*, vol. 12, no. 11, pp. 1784–1794, 2001.

[27] R. Borrego-Varillas, C. Romero, O. Mendoza-Yero, G. Mínguez-Vega, I. Gallardo, and J. R. Vázquez de Aldana, “Femtosecond filamentation in sapphire with diffractive lenses,” *J. Opt. Soc. Amer. B*, vol. 30, no. 8, pp. 2059–2065, 2013.

[VI]

Fresnel phase retrieval method using an annular lens array on an SLM.

Applied Physics B, 117(1), 67-73. 2014.

Appl. Phys. B (2014) 117:67–73
DOI 10.1007/s00340-014-5799-9

Applied Physics B
Lasers and Optics

Fresnel phase retrieval method using an annular lens array on an SLM

**V. Loriot · O. Mendoza-Yero · J. Pérez-Vizcaíno ·
G. Mínguez-Vega · R. de Nalda · L. Bañares ·
J. Lancis**

Received: 21 January 2013 / Accepted: 11 February 2014 / Published online: 1 June 2014

Abstract Wavefront aberrations play a major role when focusing an ultrashort laser pulse to a high-quality focal spot. Here, we report a novel method to measure and correct wavefront aberrations of a 30-fs pulsed laser beam. The method only requires a programmable liquid-crystal spatial light modulator and a camera. Wavefront retrieval is based on pupil segmentation with an annular lens array, which allows us to determine the local phase that minimizes focusing errors due to wavefront aberrations. Our method provides accurate results even when implemented with low dynamic range cameras and polychromatic beams. Finally, the retrieved phase is added to a diffractive lens codified onto the spatial light modulator to experimentally demonstrate near-diffraction-limited femtosecond beam focusing without refractive components.

1 Introduction

Focusing ultrashort laser pulses to a small focal region is the key to a myriad of nonlinear optical phenomena such as nonlinear microscopic imaging, manipulation and machining. However, wavefront aberrations originated by imperfections, misalignments and stress of the optical mounts in the chains inside femtosecond amplifier systems enlarge the spatial dimensions of the focal spot. It is now well established that the measurement and the correction of wavefront aberrations of the laser pulse is crucial for high-quality stable focusing [1–3]. An adaptive optics system, which consists of a wavefront sensing device and a compensating unit, measures and corrects the wavefront aberrations of a laser pulse, and eventually delivers a near-diffraction-limited focal spot to a target. The above device has been successfully applied in such different fields as to generate high laser intensities in the range of 10^{22} W cm^{-2} [4, 5], to increase the repetition rate of high-energy lasers [6] and to write optical waveguides in dielectric samples [7].

Accurate knowledge of the laser beam wavefront is the first step toward producing highly focused homogeneous intensity spots. Several phase measurement methods have already been proposed and demonstrated. The most popular is the Shack–Hartmann wavefront sensor (SHWS) where the measurement of the local phase slopes of the wavefront provides the entire beam phase [1–7]. This technique requires a microlens array that divides the pulsed beam into a number of beamlets and has been implemented, for instance, to test the temporal stability of pulsed laser beams [8]. Achromatic lateral shearing interferometers are particularly suited for the measurement of the wavefront of broadband ultrashort laser pulses because of their achromaticity [9]. Also, the angular and spectral dependences of

---

V. Loriot (✉) · R. de Nalda
Instituto de Química Física Rocasolano, Consejo Superior de Investigaciones Científicas, C/ Serrano 119, 28006 Madrid, Spain
e-mail: vincent.loriot@univ-lyon1.fr

V. Loriot · L. Bañares
Departamento de Química Física (Unidad Asociada de I+D+i al CSIC), Facultad de Ciencias Químicas, Universidad Complutense de Madrid, 28040 Madrid, Spain

Present Address:
V. Loriot
Institut Lumière Matière, UMR5306 Université Lyon 1-CNRS, Université de Lyon, 69622 Villeurbanne Cedex, France

O. Mendoza-Yero · J. Pérez-Vizcaíno · G. Mínguez-Vega · J. Lancis
GROC·UJI, Institut de Noves Tecnologies de la Imatge (INIT), Universitat Jaume I, 12080 Castellón, Spain

second-harmonic generation conversion efficiency in uniaxial crystals have been used for phase measurement [10]. On the other hand, the Fresnel phase retrieval method such as the early work of Fienup and Wackerman [11] provides the spatial phase of the pulsed beam reconstructed from only two intensity distributions at two planes along the optical axis that are measured by means of simple CCD cameras. This technique has been successfully employed for terawatt-class femtosecond laser pulses with accuracy better than $\lambda/30$ peak to valley [12, 13]. The iterative Fourier transform algorithm is used to achieve an acceptable solution for the wavefront and the effects of the dynamic range of the sensor, the intensity noise, and the wavelength-dependent error in wavefront reconstruction are considered. Concerning wavelength error, the value was demonstrated to be negligible for long pulses of 100 fs but also claimed to increase proportionally with the bandwidth for shorter pulses.

On a completely different context, liquid-crystal displays working as electronically addressed spatial light modulators (SLM) have been widely used to generate programmable diffractive lenses (DL) to focus continuous wave laser radiation, either monochromatic [14] or polychromatic [15]. Also, arrays of lenses have been codified to implement a programmable SHWS [16]. Now, the mathematical models to optimize encoding of the lens function in a device constrained by the pixelated structure and the phase quantization of the SLM are well understood [17]. Although such lenses suffer from a relatively low pupil diameter and long focal length, they allow for an electronically controlled variable focal length. But, what is more important, the use of this kind of modulators introduces the benefit of local beam control of the phase of the lens which allows for minimizing focusing errors due to wavefront aberrations.

Here, we present a novel technique for wavefront retrieval of short pulses coming from commercial amplifier systems running at mJ energy levels and temporal pulse durations at tens of femtoseconds. The method requires the implementation of a DL onto the SLM, which is subsequently apertured through a set of concentric rings in a sequential way. Also, the intensity is measured with a camera at the focal plane for each ring-shaped zone. As a result, our technique is particularly well fitted for the measurement of the drop of both the intensity profile and the diffraction efficiency at the outermost radial zones of the DL due to the reduced number of phase steps available for codifying the lens function. Our method permits to deal properly with the different arrival time of the light coming from different radial locations at the SLM plane. The segmentation of the pupil plane into subregions to measure wavefront aberrations was recently introduced in the field of high-resolution imaging in biological tissue [18]. In a second step, the lens function was codified onto the SLM, with the local phase modified in accordance with the results obtained at the sensing stage, and a laboratory experiment on the diffractive focusing of a 30-fs laser beam was carried out. Furthermore, our technique also opens the possibility of real-time tuning of femtosecond laser beams through the programmable nature of phase-only SLMs. Emerging applications as compact pulse shaping based on a single SLM require wavefront compensation to obtain a high throughput in the output pulse [19–21].

2 Optical setup

We present a schematic of our experimental setup in Fig. 1. An ultrashort laser source (FEMTOPOWER compact PRO from Femtolaser) emitted 30-fs light pulses at the central wavelength of 800 nm and repetition rate of 1 kHz. The pulsed beam was sent to a 4× all-mirror beam expander (BE) to better fit the active area of the SLM with an almost constant intensity beam. A pellicle beam splitter (BS) was inserted in the beam path. The transmitted beam was used to monitor the average power of the beam by means of a power meter (PM). The power was controlled using a variable attenuator consisting of a half-wave plate and a Glan–Thompson polarizer (not in the picture). The reflected beam impinged onto a liquid-crystal phase-only SLM (PLUTO-NIR from Holoeye) with 1,920 × 1,080 pixels and pixel pitch of eight microns. The maximum peak intensity permitted to keep a well-controlled SLM modulation is around 20 GW cm^{-2}, and the damage threshold is around 250 GW cm^{-2} corresponding to 500 μJ and 7 mJ at 30 fs, respectively, for a complete use of the modulation area allowing further high-field experiments.

In order to focus the beam, we encoded a quadratic phase factor corresponding to a DL onto the SLM. Initially,

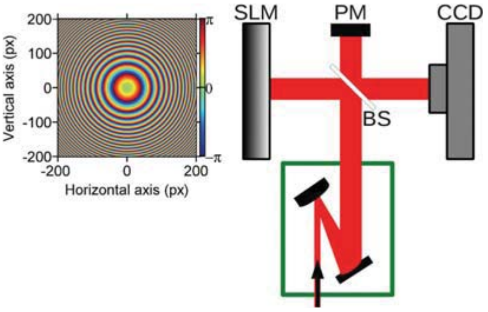

Fig. 1 Schematic of the optical setup. In the *inset*, phase transmission function encoded in the central 400 × 400 pixels of the SLM corresponding to a DL

we sent to the modulator the gray levels corresponding to the quadratic phase $\varphi(r)$ imparted by a lens of focal length f; i.e., $\varphi(r) = kr^2/(2f)$, with k the wavenumber and r the radial coordinate on the SLM pupil. In practice, the SLM displays the phase wrapped in 2π steps. Focusing artifacts (such as multiple focal lengths and higher-order diffractions) due to the pixelated and the quantized nature of the SLM were taken into account. Quantization effects originate aliasing at the outer regions of the lens since the available number of pixels to codify each wrapped zone decreases with the distance to the center due to the squared dependence of the phase with the radial coordinate. In practical terms, this effect fixes the ultimate limit for the available minimum focal length, which is given by $f = kD\Delta r/(2\pi)$, with D the lens diameter and Δr the outermost zone width that must be longer than the pixel pitch. To overcome this limit, we encoded a DL of 130 mm of focal length for 800 nm in the SLM. The CMOS camera (Ueye UI-1540M—8 bits) was located at the focal plane. The computed focal length can also be tuned so as not to saturate the camera and to obtain a reasonable spatial sampling.

Deviations from its ideal form were found and were attributed to unanticipated spatial phase inhomogeneities over the pulsed laser beam that can be described completely by the wave aberrations. It is defined as the difference between the perfect (plane) and the actual wavefront for every point at the pupil of the SLM for the mean wavelength. A perfect pulsed laser beam focuses to a circularly symmetric pattern. However, spatial phase inhomogeneities generate aberrations that produce a larger and, in general, asymmetric focal distribution. Wavefront aberrations were subsequently measured and corrected to achieve enhanced resolution and to generate high intensity in lensless pulsed beam focusing.

2.1 Wavefront sensing

To retrieve spatial phase inhomogeneities of the pulsed laser beam coming from the femtosecond system, the beam at the SLM plane was divided into N discrete zones that tile its whole active area and thereby was segmented into N beamlets individually controllable. Each zone corresponds to a circular ring whose inner, r_{in}, and outer radius, r_{out}, were chosen in such a way that the propagation time difference (PTD) for pulses originated at the two edges of the zone to the geometrical focus is smaller than the femtosecond pulse width. This PTD can be calculated by the formula $(r_{\text{out}}^2 - r_{\text{in}}^2)/(2fc)$, where c is the speed of light [20, 21]. In our experiment, we considered a PTD of 22 fs, i.e., the area of each ring was 5.32 mm^2. In addition, we chose an approach based on ring overlapping. This means that one zone overlapped with the following by a distance equivalent to half of the PTD. With the above parameters, the total number of rings employed was $N = 23$. When considering extremely short pulses, such as few-cycle pulses, this technique has technological limitations due to SLM dispersion on the one hand and to the inhomogeneities of the spatial phase across the broad spectrum on the other.

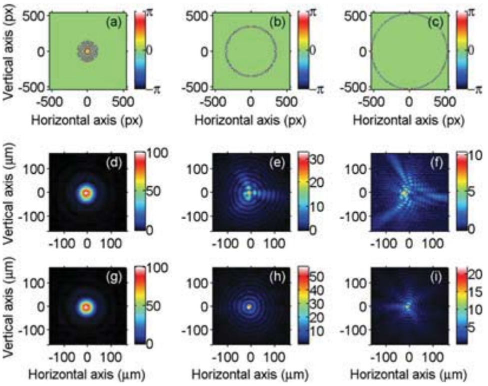

Fig. 2 a–c Phase transmission function encoded in the SLM corresponding to a DL with only one ring active, in particular the 1st, 10th and 23rd, respectively. The measured irradiance in the focal plane for each ring without (**d–f**) and with **g–i** wavefront correction

We then applied the quadratic phase pattern corresponding to a DL with focal length 130 mm only to one of the zones. The remaining zones were driven with a phase pattern corresponding to a diverging lens that causes the associated beamlets generate negligible effect at the focus, rendering them effectively “off.” We acquired an image at the focal plane using the sole remaining “on” beamlet. An example of the SLM phase distribution corresponding to several ring-shaped zones used in the experiment can be found in Fig. 2a–c. To reduce the noise due to experimental fluctuations of the beam, we captured several images of the focal plane and averaged them. The focal irradiance measured with the camera for the corresponding rings are in Fig. 2d–f. Contribution of the innermost zone of the DL (ring 1) corresponds almost to the Airy pattern as can be seen in Fig. 2d. However, as expected, the output pattern recorded by the camera differs more from the ideal theoretical focal distribution of an homogeneous annulus for the outermost zones of the lens. This effect was attributed to the optical aberrations that have a strong dependence with the radial coordinate and prevents us to obtain a high-quality Airy spot when the whole area of the SLM is used to focus the beam. In Fig. 2g–i, we show results for the focal irradiance distribution generated by the

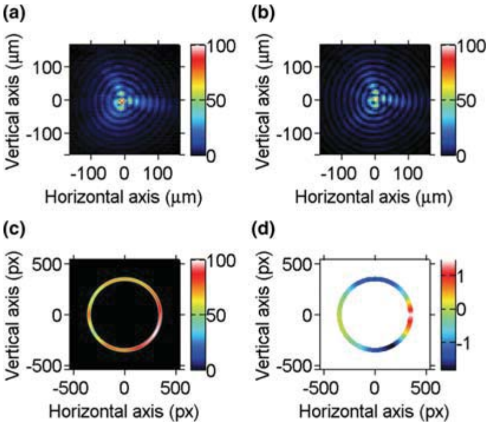

Fig. 3 Phase recovery procedure for a ring-shaped zone (10th ring) over the SLM plane: **a** experimental measurement of the focal irradiance; **b** calculated irradiance distribution from the fitted phase; **c** retrieved intensity which for our experiment is almost uniform; **d** retrieved phase

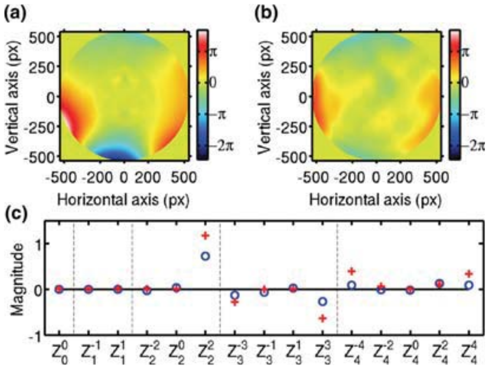

Fig. 4 Spatial phase reconstruction performed with the Fresnel phase retrieval **a** with annular lens array, and **b** with the full area. The Zernike coefficients [22] corresponding to the method shown in **a** (*plus symbol*) and method shown in **b** (*circle*) are displayed in **c**

above zones after wavefront sensing and compensation as is discussed throughout the rest of the paper. The key point in our pupil segmentation method is to take into account the broadband nature of short pulses to focus light nearly free of chromatic artifacts. As mentioned earlier, the broader the spectrum of the laser the higher the number of ring-shaped zones needed in the procedure. Following the generalized Huygens-Fresnel diffraction integral, the monochromatic depth of focus (DOF) for an annulus ring of a DL can be expressed by the formula DOF $\approx 1.76f^2\lambda_0/(r^2_{out} - r^2_{in})$. Whenever the DOF is longer than the longitudinal chromatic aberation of the focusing system we will be able to record with the camera structures close to the Ary pattern. Then, the retrieval process will be more accurate. In this way our method is more robust with respect to the presence of chromatic aberrations than other conventional methods. The ideal number of rings corresponds to that which allows to recover a structure close to the Airy pattern for each ring.

The next step is to find the azimuthal modulation in each of the rings that causes the observed pattern at focus. In order to do that, the angular variation is parameterized at a number of reference points uniformly distributed at the SLM plane for subsequent spline interpolation. In our work we found that for all the practical aberrations, 12 points are sufficient to recover the main information of the wavefront. As we deal with complex patterns, 24 independent parameters are required (12 for the amplitude and 12 for the phase). One of the 12 phase elements was fixed to remove the insensitive effect of a global shift in the absolute phase. To ensure that the fitting procedure is self-consistent, we also added the ring position and the width as free test parameters. The intensity distribution at focus derived from each set of intensities and phases was calculated through the Fourier transform. The fit of the 25 parameters was obtained from a 2D least-squares fitting procedure where the searched target was the minimum Euclidean distance from the calculated to the experimental irradiance distribution at focus. The ring position and the width test parameters were checked in each reconstruction and were in agreement with the segmentation used in the experiment. With the remaining 23 parameters and by means of a spline interpolation, we were able to obtain the retrieved intensity and phase as is shown in Fig. 3. In Fig. 3b, we illustrate the reconstructed output intensity from the retrieved amplitude and phase. The agreement between the measurement and the 2D fit is satisfactory.

Next, we repeated the previous procedure for the whole set of ring-shaped zones. To optimize the time required for the calculus, the final parameters obtained in one ring were used as the initial parameters for the next ring-shaped zone. The full phase over the SLM plane is generated through stacking the information obtained for each zone. The retrieved phase over the SLM pupil in our case is shown in Fig. 4a, where we have omitted the constant and the linear phase terms as they do not provide relevant information. This corresponds to canceling Z_0^0, Z_1^{-1} and Z_1^1 Zernike coefficients (as shown in Fig. 4c). The Z_0^0 term is the absolute spatial phase that cannot be detected with a linear detector, and $Z_1^{\pm 1}$ corresponds to a global displacement of the signal that can also be due to the vibration of the setup. In our example, few orders of Zernike polynomials are enough to correctly describe the spatial phase. We can see that numeric noise is more intense for the innermost zone. This is due to the fixed number of reference points used to sample the zones of the SLM plane, which are closer for this zone. To compare our results, we also calculated the aberrated wavefront with the Fresnel phase retrieval method using the conventional iterative Fourier transform algorithm (IFTA) [12, 13]. We considered that the intensity over the SLM was constant and measured the focal irradiance pattern generated by the whole DL. In the iterative calculation, we analyzed the convergence of the algorithm by measuring the root mean square (rms) error between the image in the focal plane measured with the camera and the reconstructed image. Because the rms error of the intensity approaches an asymptotic value after iteration of the order of 100–300, the number of iterations was fixed at 300. The retrieved phase is shown in Fig. 4a. As will be seen below, for the border area of the pupil, we have less information of the phase than the one obtained with the proposed annular lens array method.

2.2 Pulsed beam focusing

To provide a demonstration of the capabilities of our method, we designed an experiment for lensless focusing of a femtosecond pulsed beam. To this end, we simply used a SLM and no additional optics. Onto the SLM, we encoded the quadratic phase factor corresponding to a DL, together with the phase that corresponds to the wavefront correction for our laser beam. Let us mention here that the drawback of the procedure (shared with other methods of diffractive correction of wavefront aberrations) is that the finite number of pixels of the SLM causes the efficiency of the encoded DLs to depend on the radial coordinate. This unwanted effect reduces the peak intensity of the pulses coming from the outer zones of the encoded DL. Satisfactorily, our method is well suited to measure the radial dependence, as the active area of the SLM is sampled through ring-shaped zones. For each ring-shaped zone, we evaluated the mean power that arrives to the focal plane and the values were normalized at its maximum value. In Fig. 5a, we show the dependence of the efficiency of our DL of 130 mm focal length with the ring number. Error bars correspond to the standard deviation, as several images per ring where used to calculate the corresponding efficiency. As expected from a theoretical point of view, focalization efficiency of the outermost ring is about 40 % as the DL is encoded with only two phase levels [23].

Let us mention two different procedures to partially mitigate the radial drop of the diffraction efficiency. On the one hand, codification of DLs with a longer focal length helps, as the outermost zone width is higher. Unfortunately there are some applications where this is not an option. On the other hand, to guarantee a constant radial response, it is possible to reduce the efficiency of the inner parts of the lens by controlling the design parameters through the maximum value of the wrapped phase [24]. In this way, the efficiency of the lens can be made constant over the whole radius at the expense of the reduction in the global energy derived to the main focal plane. This last solution has successfully been implemented in this configuration by our group in [19].

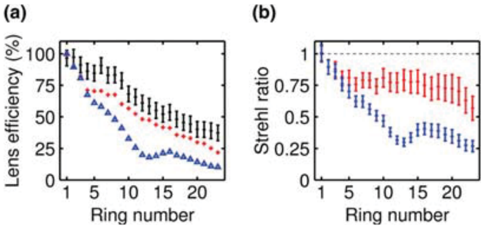

Fig. 5 **a** Diffraction efficiency of each of the rings used to segment the DL is presented by the black errorbar signal (*plus symbol*). The maximum peak intensity recorded in each image is shown for the uncompensated spatial phase (*triangle*) and the pupil segmentation compensation (*plus symbol*). The estimated Strehl ratio for each ring is then extracted in **b** for the uncompensated (*blue plus symbol*) and the compensated spatial phase (*red plus symbol*)

To quantify the improvement of the spatial phase compensation, we estimate the Strehl ratio for our 23 rings. If the spatial phase is flat, we may observe a constant ratio between the maximum of signal of each image and the image integral of signal for all the 23 rings (both shown in Fig. 5a). Since the first ring is a small disk, we can assume that the spatial phase is negligible; in this case, the Strehl ratio is assumed to be 1. Hence, the Strehl ratios are evaluated for all the rings through a calibration with the central disk. This estimation is displayed in Fig. 5b for the measurement with and without corrections. The correction allows us to maintain a reasonable Strehl ratio for all the rings. It means that the spatial phase is almost completely removed. If the spatial phase is correctly removed for all the rings independently then the spatial phase can be deleted for the full spatial profile.

Finally, let us compare in Fig. 6 the irradiance distribution in the focal plane of the encoded SLM in three different cases: (a) without wavefront correction, (b) with the wavefront correction provided by the Fresnel phase retrieval method and (c) with the added phase obtained with our pupil segmentation method. It appears clear that the spatial phase has a strong influence on the focalization of the pulse. In Fig. 6a, the peak intensity is quite low (see colorbar) due to the fact that aberrations cause blurring of the focal spot. With the Fresnel phase retrieval method, most of the problems have been corrected, the Strehl ratio has improved by about 36 %, but the spatial compression is still not perfect. We attribute this fact to the poor quality of

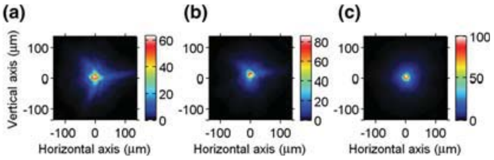

Fig. 6 Measurement of the intensity distribution of the full beam at the focal plane **a** without any correction of the spatial phase, **b** by using the Fresnel phase retrieval correction and **c** with the correction of the spatial phase presented in this article

the image in Fig. 6a used to retrieve the phase. The quantized levels of the camera and the broad spectrum of the laser pulse cause the blurring of the image, which results in a loss of resolution for the iterative method. Although the phase retrieval and pupil segmentation methods provide similar results with monochromatic illumination and high dynamic range cameras, we have found that in our experimental conditions, the pupil segmentation method provides better results because the fit with a limited number of parameters overcomes the limitation originated by the discrete intensity levels of the camera and the experimental noise. Therefore, pupil segmentation provides stronger focalization, with a Strehl ratio improved by about 60 % compared with the uncorrected case. Furthermore, the circular symmetry of the output pattern is recovered, demonstrating that the SLM provides a convenient way to achieve maximum focusing power. This shows that annular segmentation into subregions is a well suited technique to measure with high accuracy polychromatic pulsed beams with low dynamic range cameras.

3 Conclusion

In this paper, we present an innovative spatial phase retrieval method based on pupil segmentation. To implement our method, only an SLM and a camera are needed. The pupil plane corresponds to the SLM, where a DL is encoded, and the output plane is the focal plane where the camera is placed. The pupil plane is decomposed into overlapped concentric rings and, at the same time, the corresponding irradiance for each ring is recorded with the camera. By means of a least-square fitting procedure, the phase and amplitude distribution of the input beam over the SLM plane was retrieved. In our experiment, the amplitude was almost flat and the phase was compared with the one obtained with the Fresnel phase retrieval method. We found that our proposal provides more accurate results. To test our method, we did an experiment based on lensless focusing a 30-fs femtosecond laser beam. To increase the quality of the focal spot, aberrations were corrected. The complex conjugate phase of the retrieved phase was encoded onto the SLM together with the DL. We observed that the spatial quality and intensity of the focal spot obtained at the focal plane are higher when compared to the conventional Fresnel phase retrieval method. This was attributed to pupil segmentation that allows to overcome the limitations associated with the poor dynamic range of conventional cameras. This advantage is even crucial with polychromatic coherent beams such as the 30 fs pulse employed in the present experiment. In this case, we demonstrated that pupil segmentation is a well suited technique to overcome the additional blurring associated with chromatic aberrations in the Fresnel phase retrieval method. Work is in progress to reduce the number of acquisitions, keeping the same dynamic range, to make the technique well suited also for low repetion rate lasers. The adaptation of the Fresnel phase retrieval method to the pupil segmentation technique will be seen elsewhere.

Acknowledgments This work was supported by the Spanish Ministerio de Economia y Competitividad (MINECO) and FEDER through the projects FIS2010-15746, SAUUL (CSD2007-00013), CTQ2008-02578 and CTQ2012-36184-C02-01. Also, financial support from the Generalitat Valenciana through project PROMETEO/2012/021, the Universitat Jaume I through project P1•1B2013-53 and European network ITN FASTQUAST (PITN-GA-2008-214962) is acknowledged. The authors are grateful to the Serveis Centrals d'Intrumentació Científica of the Universitat Jaume I for the use of the femtosecond laser.

References

1. K. Akaoka, S. Harayama, K. Tei, Y. Maruyama, T. Arisawa, Proc. SPIE **3265**, 219 (1998)
2. B. Schäfer, K. Mann, G. Marowsky, C.P. Hauri, J. Biegert, U. Keller, Proc. SPIE **5918**, 59180P
3. T.A. Planchon, J.-P. Rousseau, F. Burgy, G. Chériaux, J.-P. Chambaret, Opt. Commun. **252**, 222 (2005)
4. S.-W. Bahk, P. Rousseau, T.A. Planchon, V. Chvykov, G. Kalintchenko, A. Maksimchuk, G.A. Mourou, V. Yanovsky, Opt. Lett. **29**, 2837 (2004)
5. V. Yanovsky, V. Chvykov, G. Kalinchenko, P. Rousseau, T. Planchon, T. Matsuoka, A. Maksimchuk, J. Nees, G. Cheriaux, G. Mourou, K. Krushelnick, Opt. Express **16**, 2109 (2008)
6. B. Wattellier, J. Fuchs, J.P. Zou, K. Abdeli, C. Haefner, H. Pépin, Rev. Sci. Inst. **75**, 5186 (2004)
7. A. Ruiz de la Cruz, A. Ferrer, W. Gaweld, D. Puerto, M. Galván Sosa, J. Siegel, J. Solis Opt. Express **17**, 20853 (2009)
8. J.M. Bueno, B. Vohnsen, L. Roso, P. Artal, Appl. Opt. **49**, 770 (2009)
9. J.-C. Chanteloup, F. Druon, M. Nantel, A. Maksimchuk, G. Mourou, Opt. Lett. **23**, 621 (1998)
10. R. Borrego-Varillas, C. Romero, J.R. Vázquez de Aldana, J.M. Bueno, L. Roso, Opt. Express **19**, 22851 (2011)
11. J.R. Fienup, C.C. Wackerman, Opt. Lett. **3**, 2729 (1978)
12. S. Matsuoka, K. Yamakawa, J. Opt. Soc. Am. B **17**, 663 (2000)
13. T.M. Jeong, C.M. Kim, D.-K. Ko, J. Leet, J. Opt. Soc. Korean **12**, 186 (2008)
14. J.L. Martínez, I. Moreno, E. Ahouzi, Eur. J. Phys. **27**, 1221 (2006)

15. A. Márquez, C. Iemmi, J. Campos, M.J. Yzuel, Opt. Lett. **31**, 392 (2006)
16. J. Arines, V. Durán, Z. Jaroszewicz, J. Ares, E. Tajahuerce, P. Prado, J. Lancis, S. Bará, V. Climent, Opt. Express **15**, 15287 (2007)
17. E. Carcolé, J. Campos, S. Bosch, Appl. Opt. **33**, 162 (1994)
18. N. Ji, D.E. Milkie, E. Betzig, Nat. Methods **7**, 141 (2010)
19. O. Mendoza-Yero, V. Loriot, J. Pérez-Vizcaíno, G. Mínguez-Vega, J. Lancis, R. de Nalda, L. Bañares, Opt. Lett. **37**, 5067–5069 (2012)
20. G. Mínguez-Vega, O. Mendoza-Yero, J. Lancis, R. Gisbert, P. Andrés, Opt. Express **16**, 16993 (2008)
21. V. Loriot, O. Mendoza-Yero, G. Mínguez-Vega, L. Bañares, R. de Nalda, IEEE Photon. Technol. Lett. **24**, 273–275 (2012)
22. American National Standard for Ophthlmics. ANSI® Z80.28-2009, Annex 6
23. S. Sinzinger, J. Jahns, *Microoptics* (Wiley VCH, Weinheim, 2003)
24. V. Moreno, J.F. Román, J.R. Salgueiro, Am. J. Phys. **65**, 556 (1997)

[VII]

Dynamic Control of Interference Effects between Optical Filaments through Programmable Optical Phase Modulation.

Submitted for publication.

Dynamic Control of Interference Effects between Optical Filaments through Programmable Optical Phase Modulation

R. Borrego-Varillas, J. Pérez-Vizcaíno, O. Mendoza-Yero,
J. R. Vázquez de Aldana, G. Mínguez-Vega, and J. Lancis, *Member, IEEE.*

***Abstract*— Light beams shaped by programmable megapixel spatial light modulators (SLMs) are key to broaden the applications of photonics. In this paper, we consider the application of a SLM for the generation of two mutually coherent white-light continuum optical sources by focusing a single infrared femtosecond pulse in bulk. We demonstrate that the inhomogeneity of the input beam and the longitudinal separation of the filaments are crucial parameters that break down the mutual coherence across neighboring filaments. We show that local control over the optical phase enables us to gain fine control over filament interference effects.**

***Index Terms*— Optical pulse shaping, spatial coherence, supercontinuum generation.**

I. INTRODUCTION

SUPERCONTINUUM (SC) generation refers to an extreme spectral broadening, which is usually accomplished by strong nonlinear propagation of a laser pulse [1]. It has been observed in a variety of media ranging from gases and liquids, to solids [2], including photonic crystal fibers [3]. Thanks to its broadband and ultrashort characteristics, it is a unique light source for practical applications such as femtosecond time-resolved spectroscopy [4], spectral interferometry [5], or its use as seed pulses for optical parametric amplifiers [6].

Moreover, there are diverse applications for SC sources which strongly depend upon coherence of the SC source, such as optical coherence tomography [7], high precision metrology [8], high-speed telecommunication industry [9], ultrashort pulse generation [10] and accuracy frequency measurement in spectroscopy [11]. Furthermore, the spectral coherence properties of a light pulse have shown to play an important role in the product achieved from some chemical reactions in a pump-dump scenario [12].

The coherence properties of the SC have been the subject of diverse investigations, in both bulk materials as photonic crystal fibers. In physical systems governed by nonlinear dynamics, any tiny variation of the input magnitudes leads to a significant variation at the output. The seminal paper of Dudley [13] set the basis for a proper description of the stochastic nature of the SC generated in photonic crystal and tapered optical fibers. More recently, the detailed coherence properties of SC radiation generated in nonlinear fibers were described using second-order coherence theory. In this way it was shown that SC can be divided into quasi-coherent and quasi-stationary parts and that the relative contributions depend on the dynamics involved in the spectral broadening [14, 15].

Concerning SC pulses generated in bulk media, Bellini and Hänsch were the first to demonstrate that two white-light continuum pulses that are independently generated by phase-locked ultrashort pulses are locked in phase [16]. The mutual-temporal coherence of SC generated in glass was experimentally investigated using a diffraction-grating-based interferometer [17] and has been also demonstrated using collinear geometries with time-delayed pump pulses [18]. Watanabe et al. studied the coherence of an array of continuum sources generated by focusing 130 fs pulses in water [19], concluding that they were mutually coherent. Baum et al. demonstrated stable interference between the outputs of two noncollinearly phase-matched optical parametric amplifiers seeded by separate continua beams [20]. Stable interferences between the infrared and visible parts of a continuum spectrum have also been measured [21], evidencing that both of them are locked in phase. The coherence properties of white-light have also been exploited to generate variable linear arrays of phase-coherent SC sources [22] and it has been demonstrated the generation of a regular array of white-light filaments in glass by the use of diffractive microlenses [23].

The coherence of two adjacent SC sources is thus an issue of great importance in multi-beam filamentation. Under certain circumstances, this quantity can be measured with a Young’s two pinhole interference setup. The intimate relation between the phase correlations of the fields at the two pinholes and the visibility of the interference fringes relies on spatial and temporal overlapping of the beams. This limitation, which often is not explicitly stated, severely restricts the use of

This research was funded by Generalitat Valenciana through the programme (PROMETEO\ 2012\021), Spanish Ministry of Science (FIS2013-40666-P) and University Jaume I through the project P1 1B2013 - 53. The authors are also very grateful to the SCIC of the Universitat Jaume I for the use of the femtosecond laser.

R. Borrego-Varillas, J. Pérez-Vizcaíno, O. Mendoza-Yero, G. Mínguez-Vega, and J. Lancis, are with the Departament de Ciències Experimentals, Universitat Jaume I, 12080 Castelló, Spain (e-mail: rborrego@uji.es).

J. R. Vázquez de Aldana is with the Grupo de Investigación de Microprocesado de Materiales con Láser, Universidad de Salamanca, E-37008, Spain.

Young's interferometer for coherence measurement of multiple SC sources. The reason is the lack of homogeneity of amplified femtosecond beams, which are usually characterized by a poor beam quality factor (higher than 2). This leads to temporal delay between the beams that makes it impossible to observe interference effects at practical geometries.

On the other hand, liquid-crystal displays working as electronically addressed spatial light modulators (SLMs) have been used to generate programmable diffractive lenses. Current megapixel SLMs allow for a fine control over the local phase of an incident beam on real time. This can compensate for potential aberrations and spatial inhomogeneities of the beam. Moreover, the refresh rates of current SLMs allow for real-time control over the focal length and efficiency of the diffractive lenses. In spite of these advantages, the use of SLMs for SC coherence measurements has not been yet reported.

In this paper, we show a way of changing the visibility of the fringes in real-time by using a SLM. For this purpose, two microlenses are implemented onto the SLM, thus allowing for a precise control of the focus position and the energy coupled into each filament. A standard interferometric system is also studied for comparison.

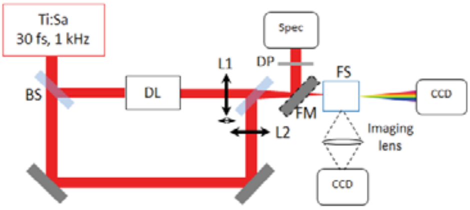

Fig. 1. Mach-Zehnder interferometer (BS: beam splitter; DL: delay line; DP: diffusing plate; FM: flip mirror; FS: fused silica plate; L_1 and L_2: refractive lenses).

II. THEORETICAL AND EXPERIMENTAL BACKGROUND

In order to fully characterize the properties of the mutual coherence between two adjacent SC sources in a conventional scenario, as a first step, we built a Mach-Zehnder interferometer (Fig. 1). It allowed us some versatility because we can independently vary the geometrical separation and the temporal delay of the two focused pulses.

As a light source we used a Ti:Sapphire femtosecond laser that emits linearly-polarized pulses of about 30 fs full-width at half maximum (FWHM) in intensity, centered at λ_0=800 nm, with a spectral bandwidth of 50 nm FWHM and a repetition rate of 1 kHz. The energy was controlled by means of a variable attenuator. A 7 mm iris was placed in front of the interferometer (this will allow us to keep the same numerical aperture that in our second experiment which includes an SLM). The beam was then split in two replicas, each one propagating in the different arms of the interferometer. In order to separate the beams laterally at the output, one of the replicas was aligned at a slightly different height than the other. Two identical refractive lenses (f=150 mm) were inserted in both arms respectively: the first lens was fixed, whereas the other was mounted in a translational stage to finely vary the separation between foci. Additionally, one of the arms was equipped with a retro-reflector mounted in a translational stage, which allowed us to control the temporal delay between pulses.

The target material for SC generation was a 5-mm thick fused silica sample. The energy was set to ~0.5 µJ per arm (under our experimental conditions, thresholds for SC generation in this sample were 0.40 µJ in one arm and 0.38 µJ in the other). When the geometrical foci for both lenses were situated at the same depth of the sample, we obtained two identical filaments laterally separated by 0.22 mm (Fig. 2a). Well-contrasted fringes appeared when both pulses were temporally overlapped, i.e. t=0 fs. The profile of the corresponding images registered by the CCD is shown as an inset in Fig. 2a (bottom). From the fringes generated by the interference of the two SC beams we can measure their visibility [24]

$$V = \frac{I_{\max} - I_{\min}}{I_{\max} + I_{\min}}$$

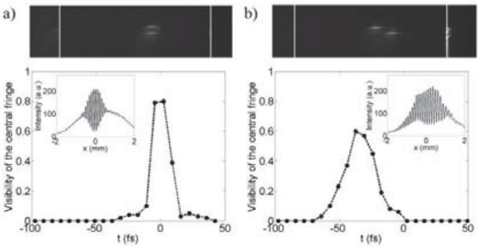

Fig. 2. Panel a) corresponds to the case where one of the both geometrical foci rely on the same plane, whereas in b) one was slightly displaced. Top: images of filaments profiles. Bottom: visibility of the central fringe as a function of the time delay. Insets show the spatial fringes extracted from the interferogram.

In our case, we observed that for the equal optical paths and zero delay our SC sources had a visibility of about 0.80. This was a typical value as it is well known from the high coherence of SC beams [16-19].

The bottom part of Fig. 2a represents the visibility of the central fringe as a function of the delay between pulses, V(τ). Since interferences will only develop at those points where pulses temporally overlap, this curve can be understood as a cross-correlation between SC pulses coming from the two adjacent filaments. The width of such curve, Δτ, is therefore related to the SC pulse duration, and consequently to the coherence length. Under these experimental conditions, we found Δτ=17.0 fs (FWHM).

In the case where the two foci of the lenses were separated 0.6 mm along the propagation axis (right panels in Fig. 2), we observed that no fringes appeared at t=0 fs. Instead, the

highest contrast was found at t= −37 fs. This temporal separation of the pulses can be partially attributed to the group velocity mismatch (GVM) between infrared (input pulses) and visible SC pulses, together with the different divergences of the SC and infrared beams. On the other hand, the value of visibility is lower, V=0.6, than that obtained when the foci are in the same plane. We explain this difference on the basis of spectral densities: since filaments develop at different depths within the material, the intensity of the spectral components is not equalized, thus affecting the fringe contrast. The width of the curve visibility vs. delay was Δτ=67.0 fs. We attribute this behavior to pulse lengthening due to chromatic dispersion: the SC generated in the second filament will suffer material dispersion for 0.6 mm more than the other one. As a consequence, the pulse is chirped and thus lengthened in time.
The reduction of the visibility and the pulse spreading are drawbacks that should be avoided for its optimum use in highly demanding practical applications.

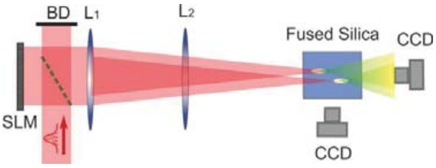

Fig. 3. Experimental setup with the SLM. (BD: beam dumper; L_1 and L_2: refractive lenses).

III. EXPERIMENTAL SETUP

Once we have studied the SC sources generated with a conventional interferometer, we focus our attention in the main objective of the paper that is the use of a SLM to perform a real time and programmable control of the fringe visibility of two SC sources.

The experimental setup for measuring the coherence of adjacent SC pulses is shown in Fig. 3. As a light source we used the same Ti:Sapphire femtosecond laser than in the previous experiment. Before the laser beam impinges onto a reflective liquid crystal on silicon phase-only SLM (Holoeye, Pluto), it was conveniently attenuated with neutral filters. The SLM has 1920×1080 pixels with 8 μm of pixel pitch. Two diffractive microlenses (DMLs) of 1.44x1.44 mm^2 each, were encoded onto the SLM both with a focal length of 60 mm for the central wavelength of the laser. The phase of each DML corresponds to that of a kinoform profile given by [25]:

$$\varphi(r, f_j) = \mathrm{mod}\left(\frac{\pi r^2}{\lambda_0 f_j}, 2\pi\right)$$

where j-index refers to each DML, λ_0 is the central wavelength, f_j is the focal length and r is the radial coordinate. The function mod(*x, y*) gives the remainder on division of *x* by *y*. This phase ranges from 0 to 2π. In order to reduce the foci's lateral separation, two opposite linear phases of the same period (80 μm) were overlapped to each of the DMLs. In this way, two filaments were formed, with a lateral separation of 0.2 mm.

Next, the reflected beam from the SLM passed through a 1x telescope composed of a pair of lenses L_1 and L_2 of focal lengths f_1=f_2=100 mm. The telescope imaged the SLM plane between the lens L_2 and a 5 mm thick fused silica block used for SC generation. The fused silica block was placed at the focal plane of the DMLs. In this way, two separated filaments were formed. The total incident energy before the beam-splitter was risen up to 110 μJ. Due to the losses in the beam-splitter and the SLM, we estimate a 3.5% of the total incident energy per kinoform lens reaching the sample. A side view of the filaments profile was made through a lens (f=60 mm) and registered by a camera. The straight forward SC light was projected onto a CCD camera which had an integrated band-pass filter (Thorlabs, FGB37S) to remove the non-converted infrared beam.

IV. RESULTS AND DISCUSSION

Under the above conditions, two filaments were formed, as shown in Fig. 4a. In spite of using the same focal length for both DMLs, the filaments appeared at different depths of the sample (separation of ~640 μm), which resulted in a minimal fringe visibility, as expected from experiments shown in Sect. 2. This focal offset can be attributed to beam inhomogeneities in terms of amplitude and phase, which may eventually lead to different position and length of the filaments. The wavefront of our laser was measured and no significant wavefront distortions were observed. However, the non-homogeneous intensity beam profile yielded an unequal energy distribution among both DMLs. As a direct consequence, the beam carrying more energy self-focused closer to the sample's front face. So although this setup is more compact than the interferometric one, it cannot be directly used to generate highly correlated SC beams unless this problem is solved.

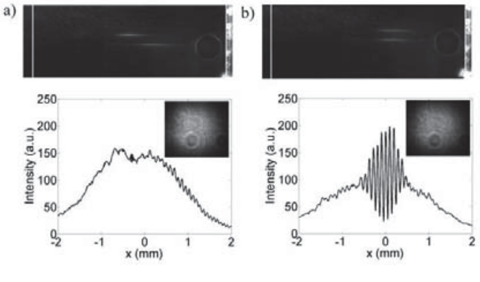

Fig. 4. Pictures of the filaments' profile (top) and corresponding fringe profile (bottom) a) without and b) with efficiency compensation Inset: interferogram. c) Visibility of the central fringe as a function of the focal length of one of the DMLs.

To face this drawback and to gain control over the energy coupled to the focus, in our proposal the phase encoded into the SLM (Eq. (2)) was multiplied by the design parameter α_j:

$$\psi(r, f_j, \alpha_j) = \alpha_j \varphi(r, f_j)$$

with α_j from 0 to 1. It can be demonstrated that the efficiency η of the lens, and thus the energy coupled to the focus, is related to α through the expression [25]:

$$\eta = \mathrm{sinc}^2(1-\alpha)$$

By adjusting the design parameter, α, and consequently the efficiencies of the DMLs, the energies coupled to both foci were equalized and thus the fringe contrast was increased. To do this, we first determined the energy thresholds to generate SC with each DML which were found to be different (3.2 µJ for the DML$_1$ and 2.5 µJ for DML$_2$). Thus the efficiency of DML$_1$ was reduced to 80% (α=0.75), while it was kept to 100% (α=1) for DML$_2$, ensuring that the energy coupled to both foci was similar. Fig. 4b shows the image of the filaments with efficiency compensation and the corresponding interferogram. Now, clear fringes are observed and we obtained a fringe visibility of 0.78 in good agreement with the expected maximum value measured with the Mach-Zehnder interferometer. Therefore, just by changing the α parameter we can tune the maximum fringe visibility obtained with our SLM proposal.

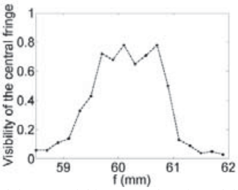

Fig. 5. Visibility of the central fringe as a function of the focal length of one of the DMLs.

To provide a more exhaustive control of the fringe visibility at a particular point of space, we performed a study of the fringe visibility as a function of the filaments' relative position. This was done by changing the focal length of DML$_2$. In Fig. 5 we depicted the visibility of the fringe located at x=0 (the center of the two beams) as a function of the focal length of DML$_2$. As expected, once the suitable α parameter was encoded in both lenses, the highest coherence degree was found for f=60 mm (i.e., same focal length for both DMLs) achieving a visibility of 0.78, and decreased monotonically as the filaments were progressively separated. In this case, the maximum visibility was displaced through positive values of the coordinate x where both pulses overlapped in time. However the poor temporal overlapping at x=0 allowed us to tune in real time the desired visibility in this position.

V. CONCLUSIONS

DLs have been shown to be a powerful tool for the spectral control of SC generation in bulk [26-28]. Here, we have demonstrated the dynamic control of the fringe visibility obtained by the interference between SC pulses generated in bulk media by using DMLs encoded into a SLM. First, the careful tuning of the DML's efficiency allowed for the optimization of the maximum fringe visibility. On the other hand, by changing the focal length of each DML, we can control easily the fringe visibility at a specific point of space. Thus, the use of a SLM allows for the implementation of compact and robust setups, with large control capabilities in the fringe visibility. The results for the SLM setup are in good agreement with the measurements obtained with the interferometric setup. Moreover, the easy alignment and operation of these systems overcome the problems of the tedious interferometric setups.

REFERENCES

[1] R.R. Alfano, The Supercontinuum Laser Source (Springer, 2006).

[2] R.R. Alfano and S. L. Saphiro, "Emission in the region 4000 to 7000 Å Via Four-Photon Coupling in Glass," *Phys. Rev. Lett.* 24, 584-587 (1970).

[3] J. M. Dudley, G. Genty, and S. Coen, "Supercontinuum generation in photonic crystal fiber", *Rev. Mod. Phys.* 78, 1135-1184 (2006).

[4] V. I. Klimov and D. W. McBranch, "Femtosecond high-sensitivity, chirp-free transient absorption spectroscopy using kilohertz lasers," *Opt. Lett.* 23, 277-279 (1998).

[5] Z. Wilkes, S. Varma, Y.-H. Chen, H. Milchberg, T. Jones and A. Ting, "Direct measurements of the nonlinear index of refraction of water at 815 and 407 nm using single-shot supercontinuum spectral interferometry*," Appl. Phys. Lett.* 94, 211102 (2009).

[6] G. Cerullo and S. de Silvestri, "Ultrafast optical parametric amplifiers," *Rev. Sci. Instrum.* 74, 1-18 (2003).

[7] I. Hartl, X. D. Li, C. Chudoba, R. K. Ghanta, T. H. Ko, J. G. Fujimoto, J. K. Ranka and R. S. Windeler, "Ultrahigh-resolution optical coherence tomography using continuum generation in an air–silica microstructure optical fiber," *Opt. Lett.* 29, 608-610 (2001).

[8] S. A. Diddams, D. J. Jones, J. Ye, S. T. Cundiff, and J. L. Hall, "Direct Link between Microwave and Optical Frequencies with a 300 THz Femtosecond Laser Comb," *Phys. Rev. Lett.* 84, 5102-5105 (2000).

[9] H. Takara, "Multiple optical carrier generation from a supercontinuum source," *Opt. Photonics News* 13, 48–51, (2002).

[10] A. Baltuška, T. Fuji, and T. Kobayashi, "Visible pulse compression to 4 fs by optical parametric amplification and programmable dispersion control," *Opt. Lett.* 27, 306-308 (2002).

[11] T. Udem, J. Reichert, R. Holzwarth, and T. W. Hänsch, "Absolute optical frequency measurement of the Cesium D1 line with a mode-locked laser," *Phys. Rev. Lett.* 82, 3568-3571 (1999).

[12] X. P. Jiang, M. Shapiro, and P. Brumer, "Pump-dump coherent control with partially coherent laser pulses," *J. Chem. Phys.* 104, 607 (1996).

[13] J.M. Dudley and S. Coen, "Coherence properties of supercontinuum spectra generated in photonic crystal and tapered optical fibers" *Opt. Lett.* 27, 1180-1182 (2002).

[14] G. Genty, M. Surakka, J. Turunen, and A.T. Friberg, "Second-order coherence of supercontinuum light", *Opt. Lett.* 35, 3057-3509 (2010).

[15] G. Genty, M. Surakka, J. Turunen, and A.T. Friberg, "Complete characterization of supercontinuum coherence" *J. Opt. Soc. Am. B* 28, 2301-2309 (2011).

[16] M. Bellini and T. W. Hänsch, "Phase-locked white-light continuum pulses: toward a universal optical frequency-comb synthesizer," *Opt. Lett.* 25, 1049-1051 (2000).

[17] I. Zeylikovich and R. R. Alfano, "Coherence properties of the supercontinuum source," *Appl. Phys. B* 77, 265-268 (2003).

[18] C. Corsi, A. Tortora and M. Bellini, "Mutual coherence of supercontinuum pulses collinearly generated in bulk media," *Appl. Phys. B* 77, 285-290 (2003).

[19] W. Watanabe, Y. Masuda, H. Arimoto and K. Itoh, "Coherent array of white-light continuum generated by microlens array," *Opt. Review* 6, 167-172 (1999).

[20] P. Baum, S. Lochbrunner, J. Piel and E. Riedle, "Phase-coherent generation of tunable visible femtosecond pulses," *Opt. Lett.* 28, 185-187 (2003).

[21] M. Bradler, P. Baum and E. Riedle, "Femtosecond continuum generation in bulk laser host materials with sub-µJ pump pulses," *Appl. Phys. B* 97, 561-574 (2009).

[22] C. Corsi, A. Tortora and M. Bellini, "Generation of a variable linear array of phase-coherent supercontinuum sources," *Appl. Phys. B* 78, 299-304 (2004).

[23] K. Cook, R. McGeorge, A. K. Kar, M. R. Taghizadeh and R. A. Lamb, "Coherent array of white-light continuum filaments produced by diffractive microlenses," *Appl. Phys. Lett.* 86, 021105 (2005).

[24] Born & Wolf, Principles of Optics (Cambridge University Press, Cambridge, 2006).

[25] V. Moreno, J. F. Roman, and J. R. Salgueiro, "High efficiency diffractive lenses: Deduction of kinoform profile," *American Journal of Physics* 65, 556-562 (1997).

[26] C. Romero, R. Borrego-Varillas, A. Camino, G. Mínguez-Vega, O. Mendoza-Yero, J. Hernández-Toro, and J. R. Vázquez de Aldana, "Diffractive optics for spectral control of the supercontinuum generated in sapphire with femtosecond pulses," *Opt. Express* 19, 4977-4984 (2011).

[27] R. Borrego-Varillas, C. Romero, O. Mendoza-Yero, G. Mínguez-Vega, I. Gallardo and J. R. Vázquez de Aldana, "Femtosecond filamentation in sapphire with diffractive lenses," *J. Opt. Soc. Am. B* 30, 2059-2065 (2013).

[28] R. Borrego-Varillas, J. Pérez-Vizcaíno, O. Mendoza-Yero, G. Mínguez-Vega, J. R. Vázquez de Aldana and J. Lancis, "Controlled multi-beam supercontinuum generation with a spatial light modulator," *Phot. Tech. Lett.*, IEEE, 26, 1661-1664 (2014).